Fall 2013

Altered Cholesterol Metabolism In Human Cancers Unraveled By Label-Free Spectroscopic Imaging

Shuhua Yue
Purdue University

Recommended Citation

Yue, Shuhua, "Altered Cholesterol Metabolism In Human Cancers Unraveled By Label-Free Spectroscopic Imaging" (2013). *Open Access Dissertations*. 11.
https://docs.lib.purdue.edu/open_access_dissertations/11

Graduate School ETD Form 9
(Revised 12/07)

PURDUE UNIVERSITY
GRADUATE SCHOOL
Thesis/Dissertation Acceptance

This is to certify that the thesis/dissertation prepared

By Shuhua Yue

Entitled Altered Cholesterol Metabolism in Human Cancers Unraveled by Label-free Spectroscopic Imaging

For the degree of Doctor of Philosophy

Is approved by the final examining committee:

Ji-Xin Cheng Chair	Ignacio G. Camarillo
Zheng Ouyang	
Young Kim	
Sophie A. Lelievre	

To the best of my knowledge and as understood by the student in the *Research Integrity and Copyright Disclaimer (Graduate School Form 20)*, this thesis/dissertation adheres to the provisions of Purdue University's "Policy on Integrity in Research" and the use of copyrighted material.

Approved by Major Professor(s): Ji-Xin Cheng

Approved by: George R. Wodicka 11/15/2013
Head of the Graduate Program Date

ALTERED CHOLESTEROL METABOLISM IN HUMAN CANCERS UNRAVELED BY LABEL-FREE SPECTROSCOPIC IMAGING

A Dissertation

Submitted to the Faculty

of

Purdue University

by

Shuhua Yue

In Partial Fulfillment of the

Requirements for the Degree

of

Doctor of Philosophy

December 2013

Purdue University

West Lafayette, Indiana

To my parents, my husband, and my son.

ACKNOWLEDGEMENTS

First and foremost, I would like to take this opportunity to express my heartfelt gratitude to my academic advisor Prof. Ji-Xin Cheng, for his constant guidance and continuous support during the past six years. His passion to science and rigorous scholarship set an excellent example for me to pursue my academic career.

I sincerely thank my graduate committee members: Prof. Ji-Xin Cheng, Prof. Sophie. Lelièvre, Prof. Ignacio Camarillo, Prof. Zheng Ouyang, and Prof. Young Kim, for their supports and kindly help in my Ph.D. study and future career.

Special thanks to Prof. Timothy Ratliff and Prof. Xiaoqi Liu for their advice on prostate cancer biology; and Prof. Sophie A. Lelièvre for her advice on breast cancer biology.

In addition, I'd like to thank all the current and former members in Cheng's group, who I have had the great pleasure of working with. In particular, I am grateful to Dr. Haifeng Wang, Dr. Thuc Le, Dr. Mihail Slipchenko, Dr. Li Li, Dr. Hongtao Chen, Dr. Brandon Huff, Dr. Yan Fu, Dr. Yunzhou shi, Dr. Ling Tong, Dr. Hanwei Wang, Dr. Jiabin Zhu, and Dr. Yookyung Jung for all of their insightful comments on my research. I also thank team colleagues Junjie Li, Hyeon Jeong Lee, Seung-Young Lee, Bing Song, Leelyn Chong, Pu Wang, Delong Zhang, Wei Wu, Nan Lin, Hunter Cooke, Anna Sullivan, and many of my friends for all the great knowledge we have shared with.

Furthermore, I greatly appreciate Prof. Timothy Ratliff, Prof. Sophie Lelièvre, Prof. Xiaoqi Liu, Prof. Michael Koch, Prof. Timothy Masterson, Dr. Liang Cheng, Dr. Juan Manuel Cárdenas-Mora, and Dr. Tiao Shao for great collaborations that lead to fruitful research achievements. I thank Prof. Kimberly Buhman, Prof. Chang-Deng Hu, Prof. Scott Crist, Prof. James Fleet, Prof. Beth Pflug, and Prof. Graham Cooks for their constructive comments on my PhD work.

I thank Mrs. Sandra Torregrosa-Allen from Purdue Cancer Center; Mrs. Debra Sherman from Life Science Microscopy Facility; Tracy and Carol from Histopathology Laboratory, and Dr. Amber Jannasch from Bindley Bioscience Center for their technical support.

Finally, I give my greatest appreciation to my husband, Yanjie Zhao, for his endless support and love. I also thank my parents and parents-in-law for their unlimited love. I would also thank my son for bringing all the happiness to my life.

TABLE OF CONTENTS

LIST OF TABLES

LIST OF FIGURES

NOMENCLATURE

2D	two-dimensional
3D	three-dimensional
AA	arachidonic acid
ABCA1	ATP-binding cassette transporter sub-family ABCA member 1
ABCG1	ATP-binding cassette transporter sub-family ABCG member 1
ACAT	acyl coenzyme A: cholesterol acyltransferase
ACC	acetyl-CoA carboxylase
Acetyl-CoA	acetyl-coenzyme A
ACLY	adenosine triphosphate-citrate lyase
ALA	alpha-linolenic acid
ApM	apical membrane
AR	androgen receptor
ATP	adenosine-triphosphate
AUC	area under curve
ATCC	American Type Cell Collection
BaM	basal membrane
BM	basement membrane
BMI	body mass index

BPE	bovine pituitary extract
BPH	benign prostatic hyperplasia
BrC	breast cancer
CARS	coherent anti-Stokes Raman scattering
CCD	charge-coupled device
CDS1	CDP-diacylglycerol synthase 1
CE	cholesteryl ester
CRC	colorectal cancer
DESI	desorption electrospray ionization
DESI-MS	desorption electrospray ionization-mass spectrometry
DGAT	diglyceride acyltransferase
DHA	docosahexaenoic acid
DiI-LDL	DiI-labeled LDL
DNA	deoxyribonucleic acid
ECM	extracellular matrix
EGF	epidermal growth factor
EGFR	epidermal growth factor receptor
EGTA	ethylene glycol tetraacetic acid
EHS	Engelbreth-Holm-Swarm
EPA	eicosapentaenoic acid
ER	estrogen receptor
ERK	extracellular signal-regulated kinase
FASN	fatty acid synthase

FBS	fetal bovine serum
FDA	Food and Drug Administration
FFA	free fatty acid
GF	growth factor
GFR	growth factor receptor
HDL	high-density lipoprotein
HDLr	high-density lipoprotein receptor
H&E	hematoxylin and eosin
hEGF	human recombinant epidermal growth factor
HMGCR	3-hydroxy-3-methyl-glutaryl-CoA reductase
IGF1	insulin-like growth factor 1
IHC	immunohistochemistry
IL-6	interleukin-6
K-SFM	keratinocyte serum free medium
LA	linolenic acid
LC-MS	liquid chromatography-mass spectrometry
LD	lipid droplet
LDL	low-density lipoprotein
LDLr	low-density lipoprotein receptor
LXR	liver X receptor
MAGL	monoacylglycerol lipase
MAPK	mitogen-activated protein kinase
MRI	magnetic resonance imaging

mTOR	mammalian target of rapamycin
MTT	3-(4,5-dimethylthiazol-2-yl)-2,5-diphenyltetrazolium bromide
NLO	nonlinear optical
NMR	nuclear magnetic resonance
OA-519	oncogenic antigen-519
OCT	optical coherent tomography
ORO	oil red O
OvC	ovary cancer
PBS	phosphate buffered saline
PCa	prostate cancer
PDPK1	phosphoinositide dependent protein kinase 1
PI	propidium iodide
PI3K	phosphoinositide 3-kinase
PIN	prostatic intraepithelial neoplasia
PMT	photomultiplier tube
PR	progesterone receptor
PTEN	phosphatase and tensin homolog
PUFA	polyunsaturated fatty acid
RNA	ribonucleic acid
ROC	receiver operating characteristic
SCD	stearoyl-CoA desaturase
SD	standard deviation
SEM	standard error of the mean

SFG	sum frequency generation
SHG	second harmonic generation
shRNA	short hairpin RNA
siRNA	small interfering RNA
SREBP	sterol regulatory element-binding protein
SRL	stimulated Raman loss
SRS	stimulated Raman scattering
TCA	tricarboxylic acid
TG	triacylglycerol
TNFα	tumor necrosis factor alpha
TPEF	two-photon excited fluorescence
TRAMP	transgenic adenocarcinoma of the mouse prostate
ZO-1	zona occludens-1

ABSTRACT

Yue, Shuhua. Ph.D., Purdue University, December 2013. Altered Cholesterol Metabolism in Human Cancers Unraveled by Label-free Spectroscopic Imaging. Major Professor: Ji-Xin Cheng.

Despite tremendous scientific achievements, cancer remains the second leading cause of death in the United States. Metabolic reprogramming has been increasingly recognized as a core hallmark of cancer. My dissertation work identified novel diagnostic markers and therapeutic targets for human cancers through the study of cholesterol in cancer cells.

Enabled by label-free Raman spectromicroscopy, we performed the first quantitative analysis of lipogenesis at single cell level in human patient cancerous tissues. Our imaging data revealed an unexpected, aberrant accumulation of esterified cholesterol in lipid droplets of high-grade prostate cancer and metastases, but not in normal prostate, benign prostatic hyperplasia, or prostatitis. Biochemical and molecular biological studies showed that such cholesteryl ester accumulation was a consequence of loss of tumor suppressor PTEN and subsequent activation of PI3K/AKT pathway in prostate cancer cells. Furthermore, we found that such accumulation arose from significantly enhanced uptake of exogenous lipoproteins and required cholesterol esterification. Depletion of cholesteryl ester storage using pharmacological inhibitors or RNA interference significantly reduced cancer proliferation, impaired cancer invasion capability, and

suppressed tumor growth in mouse xenograft models with negligible toxicity. These findings open new opportunities for diagnosing and treating late-stage prostate cancer by targeting the altered cholesterol metabolism.

My thesis work also found that cholesterol-rich domains on plasma membranes can be used as a marker for the loss of basoapical polarity, one of the earliest changes observed in breast neoplasia. Raman microspectroscopy revealed that in polarized acini lipids were more ordered at the apical membranes compared to basal membranes, and that an inverse situation occurred in acini that lost apical polarity upon treatment with Ca^{2+}-chelator EGTA. This method allowed us to detect the disruption of apical polarity by dietary breast cancer risk factor, ω6 fatty acid, even when the effect was too moderate to permit a conclusive assessment by traditional immunostaining method. Collectively, label-free Raman analysis of cholesterol-rich membrane domains in mammary acini provides an effective screening platform to identify risk factors that initiate breast cancer.

CHAPTER 1. INTRODUCTION

Despite tremendous scientific achievements, cancer remains a major global burden of disease. According to the most recent data on cancer incidence and mortality from the National Cancer Institute, and the Center for Disease Control and Prevention, cancer is the second leading cause of death in the United States with a total of 1,660,290 new cases and 580,350 cancer deaths projected to occur in 2013 [1]. In other words, in every one minute there is one person dying from cancer in the United States. With significant improvements in prevention and control of cardiovascular diseases, cancer may soon become the number one killer to human beings worldwide.

Since the first observation of chromosomal abnormalities in cancers [2] and numerous following studies on genetic transformations responsible for carcinogenesis [3-5], cancer has been classically considered as a multistep genetic disease caused by a series of abnormal activation of oncogenes and/or inactivation of tumor suppressor genes [6]. Although Warburg discovered a characteristic metabolic pattern for cancer as early as 1920s [7], metabolic reprogramming has long been underappreciated by the majority of cancer researchers. Owing to recent advances in analytic tools and progress of cancer genomics, many key oncogenic transformations in cancer cells have been found to drive metabolic signaling pathways that differ from their normal counterparts by high rates of glycolysis and biosynthesis of essential macromolecules to fuel rapid growth [8].

Meanwhile, some of the metabolic alterations become necessary for malignant transformations [8]. Such connections between oncogenic transformations and metabolic alterations make cancer metabolism one of the most intense areas of research in cancer biology. Many excellent review articles have been published recently [8-11]. The renewed interest in cancer metabolism is opening translational opportunities for the diagnosis [12] and treatment [13] of human cancers. Most if not all cancers have been suggested to share the same essential alterations in cell physiology, namely the six hallmarks of cancer summarized by Hanahan and Weinberg in 2000 [14]. Metabolic reprogramming has been increasingly recognized as a new hallmark of cancer [15].

While normal cells reply on mitochondrial oxidative phosphorylation to generate the energy needed for cellular processes, most cancer cells activate glycolysis even in the presence of adequate oxygen, a process known as aerobic glycolysis or Warburg effect [16]. Although enough evidence has support the crucial role of aerobic glycolysis in cancer development, the underlying mechanism why cancer cells prefer to use glycolysis, a very inefficient way to generate ATP, is still under investigation [17]. Other than energy metabolism, cancer cells also adapt metabolic pathways to facilitate the biosynthesis of macromolecules needed for a new cell. The advances in proteomics greatly stimulated research, revealing the key roles of amino acids, especially glutamine [18, 19] and glycine [20], in cancer development.

1.1 Fat and Cancer

Whereas alterations to metabolism of glucose and amino acids have been extensively studied [16, 18, 20], the metabolism of another essential macromolecule, lipids, in cancer is an under-studied field [21]. Lipids are a group of water-insoluble molecules that include fatty acids, sterols, phospholipids, sphingolipids, TGs, etc. [22] Phospholipids, together with sterols and sphingolipids, form building blocks of biological membranes. TGs serve as energy storage for cells. Fatty acids provide hydrocarbon chains to produce more complex lipids, and in the meanwhile can be oxidized into acetyl-CoA for further biosynthesis or energy supply if no glucose is available. Emerging evidence also supports that lipids can also function as signaling molecules that have profound effect on a wide range of biological processes, including cell proliferation, cell differentiation, apoptosis, migration, and inflammation [23]. Recently, lipids have received considerable amount of attention in the field of cancer research, largely due to increasing evidence on the link between obesity, dietary fat intake, blood lipid levels and cancer risk.

1.1.1 Whole-body Fat Metabolism and Cancer

Obesity is a strong risk factor for many prevalent metabolic diseases, including cardiovascular disease, type 2 diabetes, and cancer [24-28]. Obesity has been reported to increase rates of both cancer incidence and mortality for a variety of cancers, including those of the oesophagus [29], colorectum [30], postmenopausal breast [31], endometrium [32], kidney [33], pancreas [34], liver [35], gallbladder [36], lung [37], cervix [38], ovary [39], prostate [40], and haematopoietic cancers [41]. It has been estimated that 14% of all deaths from cancer in men and 20% of those in women may be due to obesity in the U.S. The currently proposed factors linking obesity to cancer include insulin resistance, endogenous sex steroids, and adipokines [42]. Accumulating evidence supports that dietary fat intake is also positively associated with the risk of CRC, PCa, and BrC, but with much less compelling data for other types of cancers [43-47]. Recently, it has been recognized that specific types of fats play a much more important role in cancer development and progression compared to the total amount of fat intake. Particularly, whereas ω-3 PUFAs, including ALA, EPA, and DHA, are precursors for anti-inflammatory mediators, ω-6 PUFAs, including LA and AA are precursors for pro-inflammatory mediators [23]. The ratio between ω-6 and ω-3 PUFAs is generally believed to positively correlate with cancer risk [48-50]. A positive correlation between serum TG levels and the risk of cancers, including lung, colorectal, thyroid, prostate, breast, endometrial, and gynaecological cancers, has also been reported [51-55], although there are still some inconsistency among different studies [56-58].

1.1.2 Intracellular Fatty Acid Metabolism and Cancer

Most normal cells acquire lipids from exogenous supplies either in the form of FFAs or in the form of LDLs [59]. These exogenous lipids derive from both dietary fat intake and the lipids synthesized in the liver or adipose tissue. De novo fatty acid synthesis mainly occurs in the liver, adipose tissue, and lactating breast [59]. The TCA cycle, fueled by both glycolysis and glutaminolysis, produces citrate, which is converted into acetyl-CoA by ACLY. Acetyl-CoA is then catalyzed by ACC to produce malonyl-CoA, which is together with acetyl-CoA catalyzed by the critical enzyme FASN to generate saturated fatty acid, palmitic acid [60]. Saturated fatty acids can be further elongated through catalyzation by enzymes ELOVLs. Fatty acyl-CoA desaturases, including SCDs, can introduce one double bond to produce mono-unsaturated fatty acids [60]. Because essential PUFAs cannot be synthesized *de novo*, highly unsaturated fatty acids are produced by desaturation of essential PUFAs obtained exogenously [60].

1.1.2.1 *De Novo* Fatty Acid Synthesis in Cancer Cells

Cancer cells adopt metabolic pathways that differ from their normal counterparts by high rates of *de novo* fatty acid synthesis to fuel rapid growth. The important role of *de novo* lipid synthesis in cancer cell biology has not been recognized until 1990s, when oncogenic antigen-519 (OA-519), later known as FASN, was found in cancer cells from BrC patients with poor prognosis [61]. Since then, upregulation of several lipogenic enzymes in cancer cells has been reported [21, 62] (Figure 1.1). ACLY has been shown to be important for cell transformation, proliferation and survival *in vitro* and tumorigenesis *in vivo* [63, 64]. ACC has also been reported to be overexpressed in BrC [65] and crucial for PCa cell growth and survival [66]. FASN, which catalyses the terminal steps of *de novo* fatty acid synthesis, represents the most frequently altered lipogenic enzyme in cancer cells [62]. Upregulation of FASN has been shown in many types of human cancers and their pre-neoplasia lesions, including breast, prostate, lung, oral, colorectum, ovary, oesophagus, melanoma, etc [62].

Two major mechanisms have been proposed to account for FASN overexpression in cancer cells. The major one is through GFs and GFRs. Phosphorylation of GFRs, such

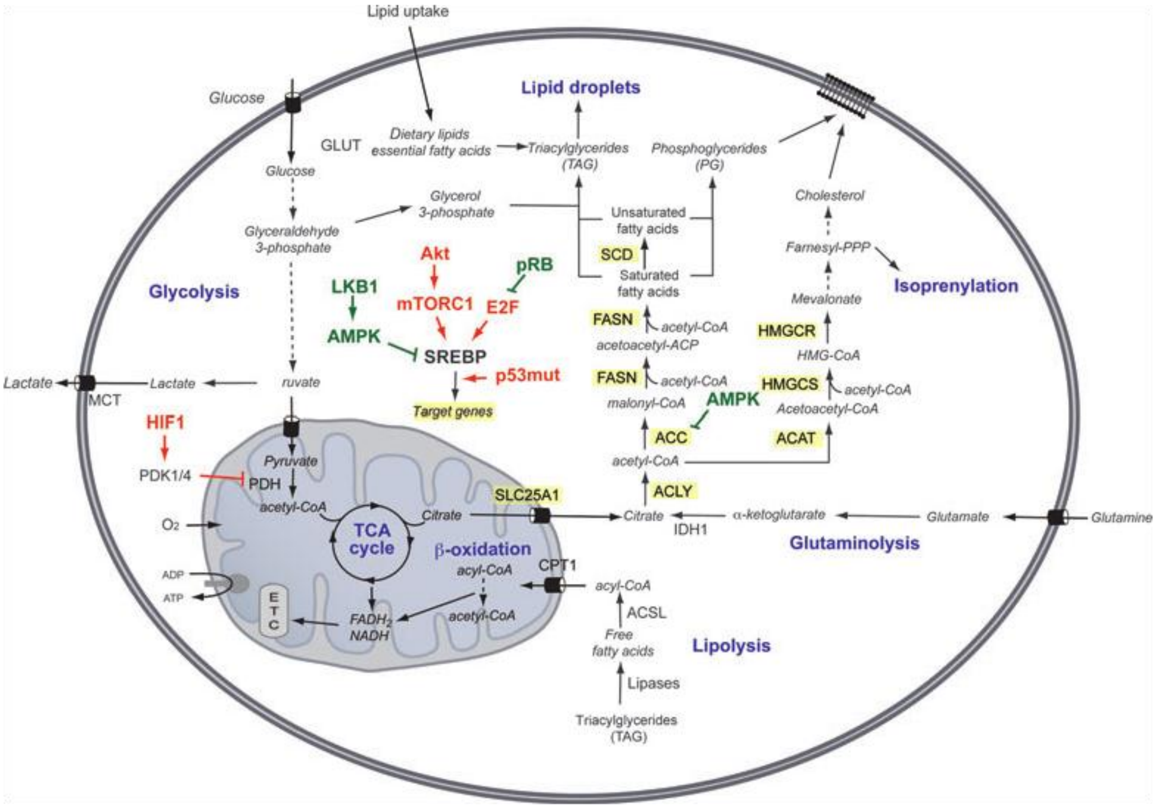

Figure 1.1 Regulation of lipid metabolism by oncogenic signalling pathways. Many cancer cells show high rates of de novo lipid synthesis. Fatty acids are required for the production of phosphoglycerides, which, together with cholesterol, can be used for building cell membranes. Triacylglycerides and cholesterylesters are stored in LDs. Lipids from extracellular sources can also be used for these purposes. Fatty acids mobilized from lipid stores can be degraded in the mitochondria through b-oxidation to provide energy when required. Many enzymes within the fatty-acid and cholesterol-biosynthesis pathways are regulated by SREBPs (highlighted by yellow boxes). Oncogenic activation of the PI3K/Akt pathway promotes glucose uptake and its use in lipid synthesis through activation of SREBP. Activation of E2F following loss of the retinoblastoma protein increases expression of SREBPs and their target genes. Mutant p53 (p53mut) increases the expression of genes within the cholesterol biosynthesis (mevalonate) pathway by binding to their promoters. AMPK is activated in response to low cellular energy levels and prevents lipid synthesis and stimulates b-oxidation through inhibition of ACC. AMPK can also inhibit SREBP by direct phosphorylation. Activation of HIF1 by hypoxia reduces the flux of glucose to acetyl-CoA through the mitochondria. Reductive metabolism of glutamine-derived a-ketoglutarate provides cytoplasmic citrate in hypoxic cells. Reprinted with permission from [21]. Copyright © 1999-2013 John Wiley & Sons, Inc.

as EGFR (also known as ERBB1) and ERBB2 (also known as HER2), activates the downstream signaling pathways, including PI3K–AKT and MAPK-ERKs (ERK1 and ERK2) transduction cascades [62] (Figure 1.1). Another possible mechanism is through steroid hormones, including estrogen, progestin, and androgen, and their corresponding receptors, i.e. ER, PR, and AR. The binding of steroid hormones to their receptors also activates the identical downstream pathways [62] (Figure 1.1). Both PI3K-AKT and MAPK-ERK pathways have been found upregulated and implicated in cancer pathogenesis [67, 68]. These two oncogenic signaling pathways regulate FASN expression through SREBPs [69] (Figure 1.1). The SREBPs are transcription factors that function to control lipid and cholesterol homeostasis by sensing cellular cholesterol [70]. Activation of SREBP has been frequently observed in a number of cancers. The three SREBP isoforms, SREBP-1a, -1c, and -2, have different roles in lipid synthesis. Whereas SREBP-1a and -2 are relatively specific to cholesterol synthesis, SREBP-1c is responsible for *de novo* fatty acid synthesis [71].

Increased *de novo* fatty acid synthesis renders new therapeutic targets for cancer treatment [21, 72]. Among all the overexpressed lipogenic enzymes, FASN is the most attractive target due to its universal upregulation in various types of cancers [62]. Several FASN inhibitors have been developed, including C75, orlistat and GSK837149A, and the current data suggest the potential of FASN to be a good clinical target [62]. Nevertheless, the side effect of FASN inhibition on central nervous system raises significant concerns about safety of these drugs [62].

1.1.2.2 Lipid Hydrolysis in Cancer Cells

The majority of research on altered lipid metabolism in cancer has been focusing on *de novo* fatty acid synthesis until the recent finding of MAGL, a lipolytic enzyme that is highly elevated in aggressive cancer cells from multiple tissues of origin [73, 74] (Figure 1.1). MAGL hydrolyzes monoacylglycerols to release FFAs, which were found to correlate with aggressiveness of cancer cells [73, 74]. MAGL inhibition by inhibitor JZL184 or shRNA was shown to significantly suppress cancer cell proliferation, migration, invasion, and growth *in vivo* [73, 74]. Nevertheless, the inhibitory effect of MAGL inhibition on cancer growth was restored by high-fat diet [73]. Further studies are needed to clarify whether the functions of fatty acids derived from *de novo* synthesis or released from lipolysis are different. This may address the concern about simultaneous increase of both lipogenesis and lipolysis.

1.1.2.3 FFAs Promote Cancer Development

FFAs have been shown to promote different aspects of cancer development [21, 72] (Figure 1.1). First, quite a number of FFAs are esterified to phospholipids, which are important structural lipids for membrane synthesis. Second, FFAs are oxidized during periods of energy stress. As an example, PCa generally displays low levels of glycolysis and high levels of β-oxidation enzymes [75]. Increased β-oxidation has also been found in pancreatic cancer, leukaemia, and glioblastoma cells [21, 72]. Third, FFAs provide sources for derivative signaling lipids, such as phosphatidic acid, lysophosphatidic acid, prostaglandins, and leukotrienes. Lysophosphatidic acids promote cell aggressiveness through regulation of G protein-coupled receptors [76]. Both prostaglandins and leukotrienes have been implicated in a variety of human malignancies, including inflammation and carcinogenesis [77]. In addition, FFAs also contribute to other aspects of cancer biology, such as redox homeostasis and resistance to oxidative stress [21, 72].

1.1.2.4 Neutral Fat Storage in Cancer Cells

Neutral fat are stored in LDs, an organelle that has a monolayer of phospholipid and specific proteins [22]. Cells contain various types of LDs with distinct functions due to the proteins attached, such as LD structural proteins, lipid synthesis enzymes, lipases, and membrane-trafficking proteins. LDs often play dynamic roles in various aspects of lipid metabolism [78-80]. The aberrant accumulation of LDs is associated with some of the most widespread human diseases, such as obesity, diabetes type II, and atherosclerosis [81].

Based on the findings of upregulated expressions of both lipogenic and lipolytic enzymes, it is conceivable that cancer cells require reservoirs for lipids, namely LDs, to store newly synthesized lipids on one hand and provide lipids for hydrolysis on the other hand. Indeed, as early as the 1970s, LDs were reported in clinical studies of mammary carcinoma [82]. Since then, lipid accumulation has been described in many types of human cancers, including breast, brain, colon and others [83-85]. For CRC, LDs were found to serve as reservoirs of cyclooxygenase 2 and prostaglandin synthase [84], which have been shown to be implicated in various human malignancies including inflammation and cancer [86]. For PCa, LD accumulation in LNCaP-LP was reported and attributed to the upregulation of fatty acid synthase [87, 88]. Lipid accumulation was also shown to contribute to dendritic cell dysfunction in cancer [89]. **Despite these scientific progress**

[90], **lipid accumulation has not, to date, been used as a prognostic factor or therapeutic target of cancer. In particular, because compositions of LDs are not readily accessible with traditional methods, the exact role of lipid accumulation in cancer progression remains elusive.**

1.2 Cholesterol and Cancer

Cholesterol is an essential biomolecule that plays important roles in the maintenance of membrane structure, signal transduction, and provision of precursor to hormone synthesis [91]. Although there has been an undoubted link between cholesterol and cardiovascular disease [92], **the role of cholesterol in cancer remains elusive**. This key section will thoroughly review the current understanding of cholesterol metabolism in cancer at both whole-body and cellular levels.

1.2.1 Whole-body Cholesterol Metabolism and Cancer

Cholesterol can be acquired from diet or endogenous biosynthesis. Dietary cholesterol is absorbed by enterocytes of the small intestine and is further packaged into the lipoprotein chylomicrons, which after addition of new apoproteins are taken up by hepatocytes of the liver [93]. Along with the cholesterol synthesized *de novo* by the liver, hepatocytes secrete cholesterol in VLDL particles that are further processed into LDL [59, 93]. LDLs contain the most cholesterol content among all lipoproteins and deliver cholesterol into periphery tissues for key biological processes. Excess cholesterol from periphery tissues are released to HDLs, which carry cholesterol back to the liver [59, 93].

1.2.1.1 Dietary Cholesterol Intake and Cancer Risk

Dietary Healthy dietary pattern (e.g. low in red meat, high in vegetable) has been recommended to prevent cancer [94]. In order to determine the contribution of dietary cholesterol intake to cancer risk, a number of epidemiological studies have been conducted. By evaluating food frequency questionnaire, one study has reported that dietary cholesterol intake is associated with increased risk of various types of cancers, including lung, breast, colon, rectum, stomach, pancreas, kidney, and bladder cancers [95]. A population-based case-control study from Japan also concluded that diet rich in cholesterol increased pancreatic cancer risk [96]. In contrast, a cohort study of US women did not support the association between cholesterol intake and pancreatic cancer risk [97]. In terms of CRC, a number of studies consistently show that dietary cholesterol significantly increases the risk of CRC [98-100]. Animal study has also shown that dietary cholesterol is a potent dietary co-carcinogen that promotes carcinogenesis of CRC in rats [101, 102], and reduced intake of cholesterol suppresses CRC metastasis and prolongs survival in the rat model [103]. For the squamous and small cell lung cancer patients who smoke tobacco heavily in Hawaii, cholesterol intake was found to increase the risk of lung cancer [104]. Another study from Hawaii also supports the role of dietary cholesterol intake in lung cancer in men but not in women [105, 106]. However, in the studies conducted among Japanese men in Hawaii and Finnish men, no association was observed between cholesterol and lung cancer risk [107, 108]. A pooled analysis of 12 cohort studies did not find a correlation between cholesterol or egg intake and the risk of OvC [109]. Dietary cholesterol did not significantly contribute to mammary tumor development in rats [110]. Taken together, the link between dietary cholesterol and cancer may exist, but it might depend on cancer types. More systematic clinical and preclinical studies are needed.

1.2.1.2 Blood Cholesterol Levels and Cancer Risk

Based on the large prospective study on cholesterol and cancer conducted in Korea, the relationship between total-C levels and cancer has varied greatly by tissue of origin [111]. Whereas total-C levels were positively associated with the risk of BrC, PCa, and CRC, total-C levels were negatively correlated with the risk of cancers arising from liver, lung, stomach, and esophageal [111]. A few other studies also suggest that cancer patients have declined levels of cholesterol in the blood [112-115]. The cholesterol fraction associated with the decrease in circulating cholesterol was majorly HDL-C [116]. The decreased level of HDL-C has been found to be restored when cancer is in the remission stage [117]. Because the association between circulating cholesterol levels and cancer risk varies by cancer types, we will review in more details for the most heavily studied cancer types as below.

PCa is certainly the most extensively studied cancer type with respect to the effects of circulating cholesterol levels. A number of prospective studies show that men with low circulating cholesterol are at lower risk of developing high-grade PCa (Gleason score 8-10) compared to those with high cholesterol levels. No correlation between circulating cholesterol levels and the risk of overall or low-grade PCa (Gleason score 2-6) was found [118-120]. Consistently, men with high cholesterol levels (≥ 240 mg/dL) had significantly higher risk of high-grade PCa compared to those with low cholesterol levels

(< 200 mg/dL) [121]. Although there was one study that did not find association between cholesterol levels and PCa [122], its follow-up study concluded that HDL-C levels were inversely associated with PCa risk [123]. It was also observed that both total-C/HDL-C and LDL-C/HDL-C ratios were associated with increased risk of PCa [123]. High HDL-C levels were also found to prevent against PCa in another study [124]. All these epidemiological evidence supports the positive association between hypercholesterolemia and risk of aggressive PCa.

Preclinical studies also support the role of cholesterol in PCa incidence and progression. Zhuang et al. [125] and Mostaghel et al. [126] both demonstrated that elevation of circulating cholesterol in nude mice promoted tumor growth, by increasing either the phosphorylation of AKT (a key kinase in PCa survival and growth) or the intratumoral *de novo* steroidogenesis. Solomon et al. [127] showed that the pharmacological reduction of serum cholesterol levels hindered human PCa growth in a mouse xenograft model. Spontaneous PCa models (e.g. TRAMP) have also been used to strengthen the conclusion that hypercholesterolemia results in enhanced tumor progression and metastases to the lung [128].

BrC has higher incidence in western countries, which leads to a focus on the link between diet and BrC risk. Although dietary fat intake affects blood cholesterol levels, it is not conclusive that blood cholesterol levels contribute to the overall BrC risk. In the Nurses' Health Study, serum cholesterol levels were not substantially associated with BrC risk [129]. In a prospective study of postmenopausal women conducted in Korea, a positive correlation between serum cholesterol levels and BrC incidence was found, but the strength of the association was significantly reduced after the adjustment for BMI

[130]. In another study conducted in Sweden, high cholesterol levels were found to be a risk factor for postmenopausal women but not for premenopausal women [131]. Circulating cholesterol also affects clinical outcome of BrC. A prospective study of Canadian women reported a high recurrence rate in women with high cholesterol levels [132]. Another study of Norwegian women shows an increased death from BrC in women who were in the highest quartile of cholesterol levels [133]. It was also found that postmenopausal BrC patients had higher oxLDL, total-C, and LDL-C levels compared to the matched healthy women [134]. The results from epidemiological studies are still not conclusive, because different BMI or BrC sub-type results in different circulating cholesterol.

Fewer studies have been performed on the link between cholesterol and other types of cancer. For OvC, late-stage patients who had normal LDL-C survived significantly longer than those who had elevated LDL-C [135]. Higher oxLDL levels were also found in women with OvC compared to the matched control group [134]. In terms of CRC, a prospective study conducted in Europe found a negative trend for HDL-C with CRC, but no significant trend for total-C or LDL-C with CRC [136]. The Japan Collaborative Cohort Study did not find an association between total-C and CRC neither [137], even though oxLDL was significantly higher in CRC patients. Nevertheless, higher levels of total-C, LDL-C and LDL/HDL ratios were observed in CRC patients with metastases compared to those without metastases [138].

1.2.1.3 Statin Use and Cancer Risk

As blood cholesterol levels have been shown to be closely correlated with cancer risk, it is conceivable that cholesterol-lowering drugs may prevent cancer development. Indeed use of statins, HMGCR inhibitors that lower blood cholesterol levels via blocking cholesterol synthesis in the liver, has been found to reduce the risk of cancer incidence and mortality [139-141].

PCa is certainly the most extensively studied cancer type for the effect of statins on cancer risk [142, 143]. Although there have been some conflicting results, with one study showing no association [144] and two studies reporting a positive association between statin use and PCa risk [145, 146], many more studies have collectively support a protective effect of statins [143]. In 2006, a large prospective cohort study of US male health professionals, for the first time, demonstrated a protective effect of statins on the risk of advanced PCa [147]. Specifically, although no association between statin use and risk of PCa overall was found, current use of statins was shown to reduce risk of advanced PCa by 49% and of metastatic or fatal PCa by 61%, compared with no current use. Longer use of statins ($\geq$ 5 years) was associated with even lower risk of advanced disease (0.26, 95% CI = 0.08 to 0.83). One year later, the California Men's Health Study showed that long-term use ($\geq$ 5 years) of statins was associated with a 28% lower risk for PCa compared to nonuse, among regular nonsteroidal anti-inflammatory drug users [148]. According to a large U.S. cohort study (Cancer Prevention Study II Nutrition Cohort), long-term use ($\geq$ 5 years) of statins was also found to reduce the risk of advanced PCa, even though not associated with overall PCa incidence [144, 149]. A population-based case-control study conducted in Finland further supported that users of statins, including atorvastatin, lovastatin, and simvastatin, had significantly lower risk of developing advanced PCa [150]. Recently, more reports have shown the positive correlation between statin use and reduced risk of high-grade PCa [151, 152]. Based on the data in Veterans Affairs New England Healthcare System, statin users were 31% less likely to be diagnosed with PCa and 60% less likely to be diagnosed with high-grade PCa, compared with antihypertensive medication users [153]. Studies also found that statin users were less likely to have high PSA levels [154] or develop high-grade PIN [155]. Statin use was associated with a significant improvement in PSA relapse-free survival in high-risk patients who received radiotherapy [156], and reduced risk of recurrence after prostatectomy [157] and death from PCa [158]. Collectively, these studies strongly support the hypothesis that statins reduce the risk of advanced PCa.

A number of clinical trials have been conducted to evaluate the effect of statins on BrC risk. The majority of earlier studies did not find an association between statin use and BrC risk [159]. Several recent epidemiologic studies showed promising results of statin use in BrC prevention [160-162]. The reason for this inconsistency is possibly that earlier studies analyzed all statin users as a single group, whereas the recent studies compared clinical outcomes for different types of statins (e.g. hydrophilic, hydrophobic) [163]. One of the most recent study, Danish Nationwide Prospective Cohort Study), showed that use of hydrophobic statins reduced both incidence and recurrence of BrC over 10-year follow-up [160]. Other two studies also supported the protective effect of hydrophobic statins on BrC incidence [162] and recurrence [161]. A recent cohort study on primary inflammatory BrC showed that lipophilic statins significantly improved progression-free survival [164]. A prospective randomised study evaluating the benefits of certain types of statins in BrC is warranted.

Fewer studies have been performed to evaluation the association between statin use and the risk of other types of cancer. There was one earlier study reporting 47% reduction in CRC incidence associated with long-term use of stains [165]. Unfortunately, later studies with mixed results could not reproduce this finding [166]. A 55% reduction in the incidence of lung cancer was found in statin users [167]. However, this finding was argued to be misleading due to a failure of correcting immortal time bias [168]. For OvC, statin use was found to be associated with longer progression-free and overall survival in women diagnosed with stage III/IV OvC [169].

The mechanism by which statins prevent cancer is an intense area of research. Statins are inhibitors of HMGCR, thus blocking the entire mevalonate pathway. As a result, not only cholesterol synthesis but also other cholesterol-independent reactions, including G-protein posttranslational modification, are inhibited by statins [139]. G-protein (e.g. Ras, Rac, and Rho) posttranslational modification has been shown to enhance many oncogenic events including cell proliferation and metastatic potential [139]. Nevertheless, it has been proposed that the protective effect of statins on cancer *in vivo* is largely attributed from their cholesterol-lowering capabilities [140, 143] instead of the local effects on cancer cells.

1.2.2 Intracellular Cholesterol Metabolism and Cancer

Inside cells, cholesterol is an essential molecule that plays important roles in the maintenance of membrane structure, signal transduction, and provision of precursor to hormone synthesis [93]. Cholesterol can be either *de novo* synthesized via the mevalonate pathway or taken up from exogenous lipoproteins LDL [93]. LDL is known to enter a cell via LDLr and traffic to the late endosome and lysosome to be hydrolyzed to free fatty acids and free cholesterol. The excess free cholesterol together with the fatty acyl CoA substrate is converted to CE by ACAT and stored in LDs [170] (Figure 1.2).

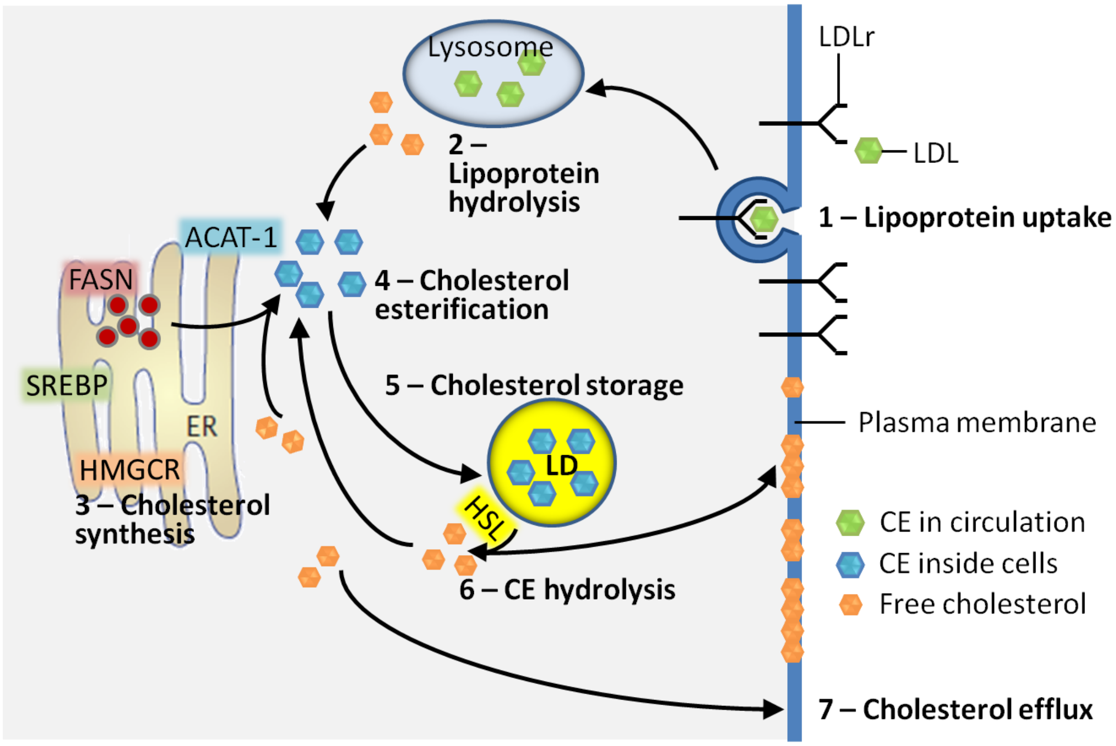

Figure 1.2 Intracellular cholesterol regulation. Cholesterol enters cells via LDLr-mediated endocytosis. CE in LDL is hydrolyzed to FC and FFAs in late endosome and lysosome system. Together with cholesterol synthesized *de novo* in the ER, excess FC is esterified into CEs and stored in LDs or effluxed to extracellular acceptors, such as HDL. FC majorly locates on plasma membranes. HSL is used for neutral lipid hydrolysis to mobile lipids for important signaling pathways.

1.2.2.1 Cholesterol Synthesis, Uptake, and Efflux in Cancer Cells

Whereas synthesis and uptake increase cellular cholesterol levels, efflux reduces cellular cholesterol levels. HMGCR is the rate-limiting enzyme that catalyzes important steps in cholesterol synthesis. A number of studies have shown that HMGCR is upregulated in many types of cancer cells and HMGCR inhibition leads to growth arrest and apoptosis [171-174]. With respect to cholesterol uptake, over-expression of LDLR has been observed in many types of aggressive cancer cells, including metastatic PCa [175, 176], ER- BrC [177, 178], and glioblastoma [179]. ABCA1 and ABCG1 are the major regulatory proteins for cholesterol efflux. ABCA1 downregulation was found in high-grade PCa tissues but not in benign prostate, and expression levels of ABCA1 were inversely associated with Gleason grades [180].

1.2.2.2 Cholesterol Homeostasis in Cancer Cells

Intracellular cholesterol homeostasis is regulated by two master transcriptional factors, the SREBP and LXR. The regulation of SREBP activity and the role of SREBP in cell metabolism have been thoroughly explored [70, 181]. In brief, when cellular cholesterol levels are low, SREBP gets activated and the cleaved form of SREBP migrates into nucleus to upregulate target genes, including HMGCR and LDLr, to promote cholesterol synthesis and uptake. SREBP has three isoforms, SREBP-1a, -1c, and -2, which play different roles in lipid synthesis. SREBP-1c is responsible for fatty acid synthesis, whereas SREBP-1a and -2 are relatively specific to cholesterol synthesis [71]. When cellular cholesterol levels are high, free cholesterol is oxidized to form oxysterols. The increased levels of oxysterols can be sensed by LXR, which activates MYLIP/IDOL for LDLr degradation and ABCA1 (or ABCG1) for cholesterol efflux [182]. Increased activation of SREBPs has been reported in advanced PCa [183] and glioblastoma [179]. LXR agonists have been shown to induce death of glioblastoma cells by reducing cholesterol uptake and increasing cholesterol efflux [179]. LXR agonist has also been reported to delay the progression of androgen-dependent PCa to androgen-independent PCa after castration [184].

1.2.2.3 Cholesterol as a Precursor of Steroidogenesis in Cancer Cells

Cholesterol is the common precursor of five different classes of steroid hormones. Steroid hormones are generally believed to be synthesized in specialized organs, the adrenal glands, testes, and ovaries. Steroid hormones are known to stimulate proliferation and differentiation of BrC, PCa, and endometrial cancer cells. Hormonal therapy has become standard therapy for several types of cancers. For men with advanced PCa, androgen deprivation therapy is an accepted standard therapy. Despite initial disease control, androgen deprivation therapy alone is non-curative and the subsequent development of castration-resistant PCa occurs in the lifespan of almost all men who do not succumb to non-cancer deaths [185]. Increasing evidence supports that androgen signaling pathways remain transcriptionally active in castration-resistant PCa [185]. The studies collectively demonstrate that castration-resistant PCa cells have the entire functional mevalonate-steroidogenesis pathway for *de novo* DHT synthesis [186-188]. Cholesterol has been shown to promote progression of castration-resistant PCa by activating the androgen signaling pathway *in vivo* [189]. These findings suggest that cholesterol could be a potential target for castration-resistant PCa [190].

1.2.2.4 Cholesterol-rich Membrane Domains (Lipid Raft) in Cancer Cells

The membrane domains rich in sphingolipids and cholesterol are called lipid rafts [191]. There are two types of lipid rafts: planar lipid rafts and caveolae. Lipid rafts function as hubs for the assembly of signaling molecules and cellular signal transduction [191]. Lipid raft signaling has been shown to be involved in various human pathogenesis, including cardiovascular disease, neurodegenerative disease, and cancer [192]. The essential role of cholesterol accumulation within membrane lipid raft in PCa progression has been thoroughly reviewed [193]. Caveolae are omega-shaped invaginations of the plasma membrane rich in caveolin protein family, including caveolin-1 [191]. Caveolin-1 has been implicated in cancer development, progression, and metastasis, particularly in PCa [194, 195]. In some cancer types, such as breast cancer, caveolin-1 may act as a negative regulator of tumorigenesis [196]. The ambiguous role of caveolin-1 in cancer may stimulate further research on the role of membrane lipid raft in cancer. **A molecular understanding of the contribution of membrane lipid rafts to cancer development has assisted the design of effective therapeutic strategies. The utility of membrane lipid rafts as diagnostic markers of cancer needs further research.**

1.2.2.5 Cholesterol Esterification and Storage in Cancer Cells

Increase cholesterol esterification and storage have been reported in leukemia [197-201], brain cancer [201-203], clear-cell renal carcinoma [201, 204-206], and BrC [177]. **Although CE accumulation in foam cells is known to be a hallmark of atherosclerosis, its exact clinical and biological role in cancer progression remains elusive. Further investigation into clinical relevance of CE accumulation in various types of human cancers would determine whether CE is a potential marker for cancer diagnosis. Future elucidation of the molecular mechanisms by which CE is accumulated in cancer cells and how CE accumulation contributes to cancer**

initiation and progression is also warranted for validation of cholesterol esterification as a potential target for cancer treatment.

In summary, the essential role of cholesterol metabolism in cancer development and progression has been increasingly recognized [166, 207-211]. Future study along this direction will open new avenue to cancer diagnosis and treatment.

1.3 Current Analytical Tools for Lipid Research

Conventionally, the investigation of intracellular lipid and its accumulation in cancer cells relies on nonspecific, invasive, or population-average measurements. Unlike many proteins where there are specific antibodies, most lipid molecules have no known specific markers, so fluorescent signals from lipophilic dyes (e.g. ORO for LD staining, and DiO or DiI for membrane staining) contain no information regarding lipid composition or organization. Similarly, electron microscopy imaging of intracellular lipid body lacks compositional information as well.

To analyze the composition of lipids, standard techniques, including mass spectrometry and NMR spectroscopy, have been employed. Although such analytical techniques are powerful, they require the most sample preparation and provide only population-average information without spatial distribution. The recent development of DESI-MS renders information of both lipid composition and spatial distribution [212], but the low resolution (~250 μm) hinders its application to cellular studies. Spontaneous Raman spectroscopy is another powerful analytical method that has been widely used in biomedical research [213-215]. However, spontaneous Raman signals are too weak to be used for high-speed imaging of lipids in biological samples.

One of the major roadblocks that prevent the research of lipids in cancer from advancing is a lack of suitable tools for charactering intracellular lipids at single cell level in a heterogeneous tissue context. Cancer tissues are known to comprise not only cancer cells but also many types of stromal cells, such as fibroblasts and inflammatory cells [15, 216]. Moreover, human cancer tissues are even more complex because they are very likely to contain both benign and cancerous cells with different histological grades within the same piece of tissue. **Undoubtedly, new methodologies which allow non-invasive, compositional, and single-cell measurement of lipids in an intact tissue environment are warranted to advance our understanding of the role of intracellular lipids in cancer development.**

1.4 Label-free Spectroscopic Imaging of Lipids in Single Live Cells

A portion of the work presented in this section was published in *Laser & Photonics Reviews* [217]. Reprinted with permission from [217]. Copyright © 1999-2013 John Wiley & Sons, Inc.

An attractive alternative to dye-labeled assay is coherent Raman microscopy, including CARS microscopy and recently developed SRS microscopy (Figure 1.2). Both of them are label-free chemical imaging techniques that probe intrinsic molecular vibrations. CARS is a NLO process in which the interaction of a pump field $E_p(\omega_p)$ and a Stokes field $E_s(\omega_s)$ with a sample generates an anti-Stokes field E_{as} at the frequency of $2\omega_p-\omega_s$. CARS microscopy is particularly sensitive to lipid-rich structures when the beating frequency ($\omega_p-\omega_s$) of the two pulsed lasers is tuned to 2840 cm^{-1} that matches

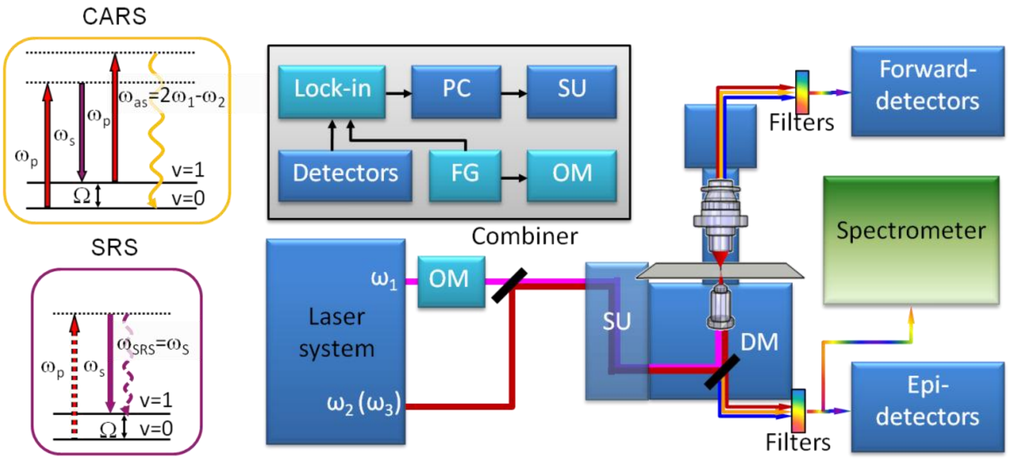

Figure 1.3 Energy diagrams and setup schematic of CARS and SRS microscopy, and Raman spectroscopy. Solid lines represent electronic and vibrational states of molecules, dashed lines are virtual states. The straight arrows are excitation beams, the wavy arrows are output signal beams. The gray arrows represent relaxation in electronically excited states. ω_1 and ω_2 are two beams available in the CARS microscope. $\omega_p = \omega_1$ and $\omega_s = \omega_2$ in CARS and SRS level diagram. Here SRG is shown as an example for SRS. Ω is a frequency of vibrational transition between vibrational ground state v = 0 and vibrationally excited state v = 1. ω_1 and ω_2 are pump and Stokes beams from the laser sources, respectively. OM is an optical modulator, SU is a scanning mirror unit. DM is an exchangeable dichroic mirror. The inset shows the connections between electronic components for phase-sensitive heterodyne detection. Lock-in is a lock-in amplifier, PD is a photodiode, PC is a computer, FG is a function generator. The blue-colored components are used for modalities with homodyne type of detection. The light blue color represents components required for modalities with heterodyne detection. The spectrometer is used for fingerprint spectral analysis.

the symmetric vibration of CH_2 bands. Such single-frequency CARS microscopy has been applied to image cellular membranes, myelin sheath, and intracellular lipids with 3D and sub-micron spatial resolution [218-222]. Compared to CARS, SRS microscopy offers two major advantages: (1) SRS signal is free of the nonresonant background, which makes it highly sensitive; (2) SRS signal is linearly proportional to the molecular concentration, which facilitates data interpretation and quantification [217]. In microscopy, the modulations of pump and Stokes beam intensities due to the SRS process are usually very small ($\Delta I/I < 10^{-4}$) as calculated for experimental imaging conditions [223]. Therefore, modulation of the excitation beam and phase-sensitive detection method are needed to pick the signal out of the laser noise. High-speed SRS microscopy has been recently demonstrated [224-229] and applied to vibrational imaging of tablets and biomass [230, 231]. We have published a detailed review on coherent Raman microscope and its biological applications (please see Ref. [217]).

In response to the strong demand for a novel technique that can visualize intracellular lipids with submicron resolution and analyze their composition *in situ*, we have developed a vibrational spectromicroscope that integrates coherent Raman microscopy and spontaneous Raman spectroscopy on the same platform [232]. With the capability of vibrational imaging and spectral analysis within a few seconds, vibrational spectromicroscope has been applied to analyze intracellular lipids in live tissues and obtain important information including lipid amount and size, degree of carbon chain unsaturation, and lipid-packing density [233]. We expect this label-free spectroscopic imaging technique to significantly advance the field of lipid metabolism in cancer.

CHAPTER 2. ALTERED CHOLESTEROL METABOLISM: NEW AVENUE TO DIAGNOSIS AND TREATMENT OF HUMAN PROSTATE CANCER

The work presented in this chapter has been submitted to *Cell Metabolism.*

Altered lipid metabolism is increasingly recognized as a signature of cancer cells. Enabled by label-free Raman spectromicroscopy, we performed the first quantitative analysis of lipogenesis at single cell level in human patient cancerous tissues. Our imaging data revealed an unexpected, aberrant accumulation of esterified cholesterol in LDs of high-grade PCa and metastases. Biochemical and molecular biological studies showed that such CE accumulation was a consequence of loss of tumor suppressor PTEN and subsequent activation of PI3K/AKT pathway in PCa cells. Furthermore, we found that such accumulation arose from significantly enhanced uptake of exogenous lipoproteins and required cholesterol esterification. Depletion of CE storage using pharmacological inhibitors or RNA interference significantly reduced cancer proliferation, impaired cancer invasion capability, and suppressed tumor growth in mouse xenograft models with negligible toxicity. These findings open new opportunities for diagnosing and treating PCa by targeting the altered cholesterol metabolism.

2.1 Introduction

Cancer cells adopt metabolic pathways that differ from their normal counterparts by high rates of glycolysis and biosynthesis of essential macromolecules to fuel rapid growth [8]. Among dysregulated metabolic pathways, increased *de novo* synthesis of lipids has become a common characteristic of human cancers [21]. For instance, FASN, the key enzyme that catalyzes the terminal steps in fatty acid synthesis, is frequently upregulated in human malignancies and plays important roles in cancer pathogenesis [62, 234]. In parallel with lipogenesis, lipolysis has also been shown to be elevated in multiple human cancers [73]. Specifically, MAGL, the lipolytic enzyme that hydrolyzes monoacylglycerols to release FFAs, was found to be overexpressed in aggressive cancer cells. Based on the findings of upregulated expressions of both lipogenic and lipolytic enzymes, it is conceivable that cancer cells require reservoirs for lipids, namely LDs, to store newly synthesized lipids on one hand and provide lipids for hydrolysis on the other hand. Indeed, as early as the 1970s, LDs were reported in clinical studies of mammary carcinoma [82]. Since then, lipid accumulation has been described in many types of human cancers, including breast, brain, colon and others [83-85]. Nonetheless, lipid accumulation has not, to date, been used as a prognostic factor or therapeutic target of cancer. In particular, because compositions of LDs are not readily accessible with traditional methods, the exact role of lipid accumulation in cancer progression remains elusive.

LDs are visualized mainly through labeling with lipophilic dyes, which requires fixation and lacks compositional information. To assay for lipid composition, analytical tools, such as mass spectrometry and nuclear resonance spectroscopy, are commonly used. Because such techniques analyze tissue homogenates, it is impossible to obtain compositional information of individual LDs inside cells. The recently developed coherent Raman scattering microscopy [235] has shed new light on the study of LD biology [217, 236], with its label-free detection capability, high imaging speed, and submicron spatial resolution. Using this technique, high-speed vibrational imaging of LD dynamics in live cells and embryos has been demonstrated [237-241]. Multiplex CARS microscopy has been used to study phase separation in LDs of 3T3-L1 cells [242]. Coupling the high-speed imaging capability of coherent Raman scattering microscopy and full spectral analysis capability of spontaneous Raman spectroscopy allowed quantitation of not only the amount, but also the composition, of individual LDs in live cells [243].

Here, we report the first quantitative analysis of lipogenesis at the single cell level in intact tissues from a spectrum of human prostate pathologies. Our label-free imaging study revealed an unexpected accumulation of CE in high-grade and metastatic human PCa tissues, but not in normal prostate, BPH, prostatitis, or PIN tissues. Our biochemical study further showed that such CE accumulation was induced by loss of tumor suppressor PTEN, upregulation of PI3K/AKT/mTOR pathway, and consequent activation of SREBP and LDLr. Pharmacological inhibition of cholesterol esterification significantly suppressed cancer proliferation, migration, invasion, and tumor growth *in vivo*. These data collectively herald the potential of using CE as a marker for diagnosis of aggressive PCa and open a new way of treating advanced PCa by targeting the altered cholesterol metabolism.

2.2 Experimental Section

2.2.1 Human Prostate Tissue Specimens

This study was approved by institutional review board. Frozen specimens of human prostate tissues derived from patients who underwent radical prostatectomy for PCa were obtained from Indiana University Simon Cancer Center Solid Tissue Bank. These patients had not received hormone therapy before radical prostatectomy. In addition, frozen specimens of normal prostate tissues donated from healthy subjects and metastatic PCa tissues collected by warm body autopsy from patients who had failed hormone therapy were obtained from Johns Hopkins Hospital. Totally, 19 normal prostates, 10 BPH, 3 prostatitis, 3 PIN lesions, 12 low-grade PCa (Gleason grade 3), 12 high-grade PCa (Gleason grade 4/5), and 9 metastatic PCa [liver (n = 2), lymph node (n = 3), rib (n = 1), lung (n = 1), adrenal (n = 1), and abdominal soft tissue (n = 1)] from 64 different patients or healthy donors were analyzed. For each tissue specimen, pairs of neighboring slices were prepared, with one slice remained unstained for spectroscopic imaging and the other stained with H&E. Pathological examination was made by genitourinary pathologists.

2.2.2 Cell Culture

K-SFM with additives BPE and hEGF, RPMI 1640, T-medium, and FBS were purchased from Invitrogen. F-12K and EMEM were obtained from ATCC. Cells were cultured in the following media: RWPE1 in K-SFM supplemented with BPE (0.05 mg/ml) and hEGF (5 ng/ml). LNCaP-LP, LNCaP-HP, and 22Rv-1 in RPMI 1640 supplemented with 10% FBS. PC-3 in F-12K supplemented with 10% FBS. DU145 in EMEM supplemented with 10% FBS. C4-2 in T-medium supplemented with 10% FBS. LNCaP-

HP was derived upon continuous passage from original LNCaP from ATCC (LNCaP-LP) until the passage number was over 60, and is an established cell line of AR-positive but androgen-independent PCa [244-247].

2.2.3 Chemicals

LY294002, MK2206, rapamycin, avasimibe, simvastatin, Sandoz 58-035, DEUP, cholesteryl oleate, glyceryl trioleate, A922500, DHT, and AA were purchased from Sigma-Aldrich. Human LDL was obtained from Creative Laboratory Products. LPDS was purchased from Biomedical Technologies. The PTEN inhibitor BPV(pic) was purchased from Enzo Life Sciences.

2.2.4 Label-free Spectroscopic Imaging

Label-free spectroscopic imaging was performed on unfixed and unstained tissue slices (~ 20 µm) and live cells without any processing or labeling. SRL imaging was performed on a femtosecond SRL microscope, with the laser beating frequency tuned to the C-H stretching vibration band at 2845 cm^{-1}, as described previously [248]. Compositional analysis of individual LDs and autofluorescent granules was performed by integration of high speed CARS imaging and confocal Raman spectral analysis on a single platform [243]. We quantify lipid metabolism profiles in two aspects, that is, LD amount (or LD area fraction) and CE percentage. By using ImageJ “Threshold” function, LDs in the cells can be selected because of their significantly higher signal intensities compared to other cellular compartments. Then, by using ImageJ “Analyze Particles” function, area fraction of LDs out of total image area can be quantified. For tissue specimen, the area fractions of LDs from the two different locations were averaged to obtain the final value of LD area fraction. For cultured cells, the area fraction of LDs was normalized by cell number to obtain LD amount, and 50~100 cells were analyzed. The percentage of CE in individual LDs was quantified by using the equation, that is, Height ratio (the height ratio of the 702 cm^{-1} peak to the 1442 cm^{-1} peak, I_{702}/I_{1442}) = 0.00255 × CE percentage (%). The corresponding calibration curve is shown in Figure 2.2T. For statistical analysis, CE percentage for each specimen or cell culture was obtained by averaging the CE percentage of LDs in 5~10 cells, given that Raman profiles of LDs in different cells in the same specimen or cell culture were nearly the same (Figure 2.2R).

Average acquisition time for a 512 x 512 pixels SRL image was 1.12 second. Large-area SRL imaging was performed on a motorized stage. Each large-area SRL image was generated by stitching 100 images of ~157 µm × 157 µm in size together. Two different locations were imaged for each specimen. Simultaneously, backward-detected two-photon fluorescence signal was collected through a 520/40 nm bandpass filter for the imaging of autofluorescent granules.

The background of Raman spectrum was removed as described [243]. 5-10 spectra of LDs or autofluorescent granules in 5-10 different cells were taken for each specimen. Each Raman spectrum ranged from 380 to 3100 cm^{-1} and was acquired in 20 seconds. The laser (~707 nm) power at the specimen was maintained at 15 mW, and no cell or tissue damage was observed.

2.2.5 Fluorescence Imaging of LDL Uptake

DiI-LDL was made using dry film method [249]. Cells in growth medium containing 10% lipoprotein deficient serum with or without the indicated inhibitors (for 2d) were incubated with DiI-LDL (20 µg/ml) for 3 hr at 37 °C and then imaged by two-photon fluorescence microscopy through a 600/60 nm bandpass filter. The LDL uptake was quantified based on fluorescence intensity of DiI using ImageJ, and normalized by cell number. No LDL uptake was detected in cells incubated at 4 °C.

2.2.6 Cell Viability Assay

Cells were grown in 96-well plates (~5000 cells/well) and cultured for 1 day followed by indicated treatments. Cell viability was measured with the MTT colorimetric assay (Sigma). IC50 was obtained by fitting the data with sigmoidal dose response model.

2.2.7 Cell Cycle Analysis

PC-3 cells treated with 7.5 µM avasimibe for 3 days and the untreated ones were collected, fixed, and stained with 50 µg/ml PI at 37 °C for 30 min. The DNA content was measured by Cytomics FC500 flow cytometer (Beckman Coulter). Data were processed and analyzed by FlowJo software (Tree Star). Cell-cycle phases and frequencies of each phase were determined by fitting the data with Watson-Pragmatic model.

2.2.8 Migration and Invasion Assays

Invasion and migration assays were performed in Transwell chambers (Corning) with 8 µm pore-sized membranes, coated with and without Matrigel (BD Bioscience) respectively. One to two days before the start of the assays, cells received indicated treatments. At the start of the assays, cells were harvested and counted. 1×10^6 cells were seeded in the upper chamber of the transwells in 1.5 ml serum-free media. The media in lower chamber contain 20% FBS. Cells were allowed to migrate for 12 hr and invade for 24 hr at 37 °C. The transwell membranes were then fixed and stained with PI. Cells that had not migrated or invaded through the chamber were removed with a cotton swab. The cells that migrated or invaded were imaged by two-photon fluorescence microscopy, and

4 fields were independently counted from each migration or invasion chamber. An average of cells in 4 fields for one migration or invasion chamber represents n = 1.

2.2.9 ESI-MS Measurement of Lipid Extraction

Lipid extraction from cell pellets and tissues was performed according to Folch *et al* [250]. Cells with indicated treatments were collected and counted. ESI-MS analysis was conducted according to the protocol described previously [251]. The relative level of cholesteryl oleate (18:1) was normalized by cell number for comparison between control and avasimibe-treated cells, and was normalized by tissue weight for comparison between normal prostate and PCa tissues.

2.2.10 Biochemical Measurement of Cellular Lipids

Lipids were extracted as described above. CE, free cholesterol, and TG concentrations were measured according to the manufacturer’s protocol (Amplex Red Cholesterol kit from Molecular Probes, Serum Triglyceride Determination Kit from Sigma), and finally normalized by protein content that was determined by bicinchoninic acid assay.

2.2.11 LC-MS Analysis of AA

Cells cultured in 10% LPDS were pre-treated with 7.5 µM avasimibe for 2 days or transfected with ACAT-1 shRNA for 3 days. LDL (20 µg/ml) were then added back to the medium for 6 hr before the cells were collected and counted. Fatty acids were extracted and measured according to the methods described previously [252]. The final AA concentration was normalized by cell number.

2.2.12 Immunoblotting

After indicated treatments, cells were lysed in AMI lysis buffer (Active Motif), and proteins were detected by immunoblotting with the antibodies against SREBP-1 (BD Pharmingen, 557036), SREBP-2 (Santa Cruz, sc-5603), p-AKT (Cell Signaling, 4060L), p-S6 (Cell Signaling, 2211L), LDLr (Millipore, MABS26), ACAT-1 (Santa Cruz, sc-69836), and β-actin (Sigma, A5441).

2.2.13 IHC

Murine paraffin-embedded slides were deparaffinized and rehydrated. Then antigens were retrieved in antigen unmasking solution (Vector Laboratories) with a 2100-Retriever (PickCell Laboratories). Samples were then incubated with the antibody against Ki67 (Abcam, ab16667) or subjected to TUNEL assay (Roche, 11684817910).

2.2.14 RNA Interference

RNA interference was employed to specifically deplete endogenous SREBP-1, SREBP-2, ACAT-1, and PTEN. Plasmids pLKO.1-SREBP-1 and pLKO.1-SREBP-2 were constructed with the targeting sequences CAACCAAGACAGUGACUUCCC and CAACAGACGGUAAUGAUCACG. The ACAT-1 shRNA plasmid and PTEN shRNA lentiviral particle were purchased from Santa Cruz (sc-29624-SH, sc-29459-V). Plasmid DNA was transfected with Lipofectamine®2000 (Invitrogen 11668030) as described in the manufacturer’s protocols.

2.2.15 Treatment of PCa in a Mouse Xenograft Model

The protocol for this animal study was approved by the Purdue Animal Care and Use Committee. PC-3 cells (2×10^6) were mixed with an equal volume of Matrigel (BD Bioscience) and inoculated subcutaneously into the right flank of 6-week-old athymic nude mice (Harlan Laboratories). Treatments started 2 weeks after tumor implantation when the xenografts were about ~100 mm^3 (day 0). Inhibitors were dissolved in DMSO, diluted with the solvent PBS containing 1% Tween-80, and administrated via daily intraperitoneal injections for 30 days at the dose of 15 mg/kg for avasimibe and Sandoz 58-035, and at the dose of 3 mg/kg for A922500. The reason that the dosage of A922500 is lower than that of Sandoz 58-035 and avasimibe is A922500 has substantially lower IC50 compared to Sandoz 58-035 or avasimibe for inhibition of the target enzyme, that is, IC50 of A922500 to inhibit DGAT-1 is ~7 nM vs. IC50 of Sandoz 58-035 and avasimibe is ~3.3 µM [253-255]. Thus, the dosages for injections were selected based on previous animal studies on these inhibitors [253, 256, 257]. Tumor volume, estimated from the formula: $V=L\times W^2/2$ (V: volume, mm^3; L: length, mm; W: width, mm), was measured twice a week with digital calipers. Relative tumor volume = tumor volume / initial tumor volume (measured on day 0), for each mouse. Body weight was also measured twice a week. Tumors and major organs, including heart, liver, lung, kidney, and spleen, were harvested on day 30 and prepared for tumor weight measurement, spectroscopic imaging, H&E, and IHC staining.

2.2.16 Statistical Analysis

Results of LD area fraction and CE percentage in human prostate tissues were shown as mean ± SD. Other results were shown as mean ± SEM. One-way ANOVA was used for comparisons of LD area fraction, LD amount, and CE percentage among different lesion types of human PCa and different treatment conditions of cell cultures. All other comparisons that only include two groups in cellular and animal studies were performed using the Student’s t test. $p < 0.05$ was considered statistically significant.

2.3 Results

2.3.1 Aberrant Accumulation of Esterified Cholesterol in Advanced Human PCa Revealed by Raman Spectromicroscopy

We examined a spectrum of human prostate pathologies, including normal prostate from healthy donors and normal adjacent tissues from PCa patients (n = 19), BPH (n = 10), prostatitis (n = 3), PIN (n = 3), low-grade (Gleason grade 3, n = 12) and high-grade (Gleason grade 4/5, n = 12) PCa from patients who had not received hormone therapy, and metastases (n = 9) from patients who had failed hormone therapy. By tuning the laser beating frequency to be resonant with C-H stretching vibration, substantial SRL signals arose from the lipid-rich cell membranes and intracellular LDs, whereas weak SRL signals were derived from the lipid-poor cell nuclei. Morphologically, the SRL images provided identical information as H&E-stained slides. In normal prostate, BPH, PIN, and prostatitis, single layers of epithelial cells facing large lumens were identified by SRL imaging (Figures 2.1A, 2.2). In cancerous specimens, the SRL signals revealed small glandular structures in low-grade PCa (Figure 2.1B) and cell clusters or sheets without any glandular structures in high-grade PCa (Figure 2.1C). SRL image of metastasis is shown in Figure 2.1D. All diagnoses were confirmed by pathologic assessment of the neighboring slices stained with H&E (Figures 2.1E-H, 2.2). By combining SRL with two-photon fluorescence on the same microscope, we found that the intracellular granules present in normal prostate expressed both SRL and fluorescence signal (Figure 2.1I), which peaked at 520 nm (Figure 2.2M).

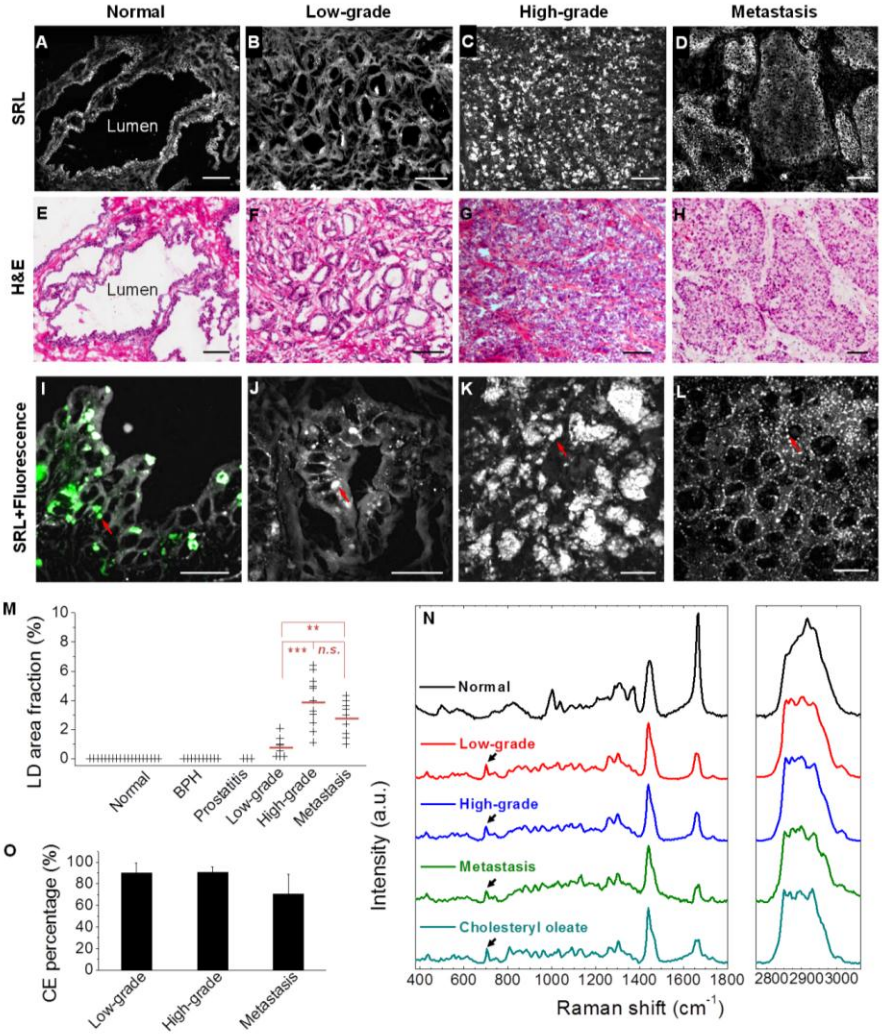

Figure 2.1 Aberrant CE accumulation in human PCa tissues. (A-D) Large-area SRL images and benign prostate, low-grade PCa (Gleason grade 3), high-grade PCa (Gleason grade 4), and metastatic PCa (liver), respectively. (E-H) Corresponding hematoxylin and eosin (H&E) staining of adjacent slices. Scalar bar, 100 µm. (I-L) High magnification SRL and two-photon fluorescence images of the lesions shown in (A-D) (grey: SRL, green: two-photon fluorescence). Autofluorescent granules and LDs indicated by red arrows. Scalar bar, 20 µm. (M) LD area fraction in 58 specimens: normal prostate (n = 19), low-grade PCa (n = 9), high-grade PCa (n = 11), and metastatic PCa (n = 9). Mean of LD area fraction indicated by red line. n.s. means not significant. (N) Raman spectra of autofluorescent granules in normal prostate, LDs in PCa, and pure cholesteryl oleate. Spectral intensity was normalized by CH_2 bending band at 1442 cm^{-1}. Black arrows indicate the bands of cholesterol rings at 702 cm^{-1}. (O) CE molar percentage in LDs of low-grade PCa (n = 9), high-grade PCa (n = 11), and metastatic PCa (n = 9). Error bars represent SD.

These autofluorescent granules were consistently seen in all 19 normal prostates, 10 BPH, and 3 PIN lesions (Table 2.1, Figure 2.2G-I), and were determined to be lipofuscin according to previous reports on pigments in benign prostate [258]. No LDs or autofluorescent granules were observed in prostatitis specimens (Figure 2.2J-L). In contrast, with the exception of 4 borderline PCa cases, the 20 primary PCa and all 9 metastases contained significant amount of LDs but no autofluorescent granules (Figure 2.1J-L, Table 2.1). Interestingly, we have found in a spontaneous mouse model of PCa (TRAMP) that whereas normal mouse prostate only contains autofluorescent granules, cancerous mouse prostate show accumulation of neutral LDs (Figure 2.2N-O). By large-area mapping and quantitation, the area fraction of LDs in human PCa tissues was found to be 0.78 ± 0.65% for low-grade PCa, 3.93 ± 1.74% for high-grade PCa, and 2.76 ± 1.19% for metastatic PCa (Figure 2.1M, Table 2.1). The high-grade PCa has significantly higher LD area fraction by ~5 folds (p = 8.9E-5) compared to low-grade PCa.

To evaluate the lipid composition, we performed confocal Raman spectral analysis of individual autofluorescent granules or LDs accumulated in each lesion type. Figure 2.1N shows representative spectra collected from normal prostate, low-grade PCa

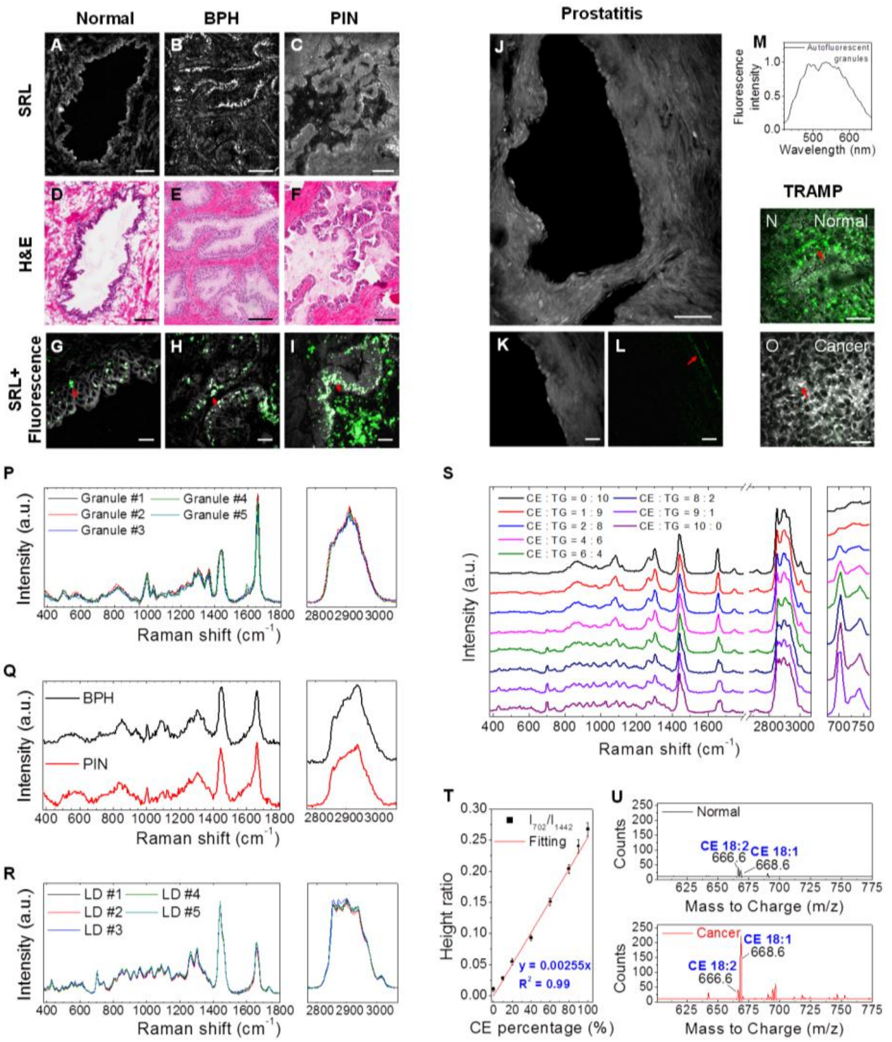

Figure 2.2 CE accumulation in normal prostate, BPH, PIN, or prostatitis. (A-I) Label-free SRL and two-photon fluorescence imaging of normal prostate, BPH, and PIN. (J-L) Label-free SRL and two-photon fluorescence imaging of prostatitis tissue. Grey: SRL; Green: two-photon fluorescence. Scalar bar: 100 µm for large-area images, 20 µm for high-magnification images. (M) Normalized two-photon fluorescence spectrum of autofluorescent granule in normal prostate. (N-O) SRL and two-photon fluorescence images of normal and cancerous mouse prostate tissues in a spontaneous PCa TRAMP model. Scalar bar, 20 µm. (P) Raman spectra of different autofluorescent granules in one normal prostate tissue. (Q) Raman spectra of autofluorescent granules in BPH and PIN lesion. (R) Raman spectra of LDs in different cells in one PCa specimen. (S) Raman spectra of CE-TG emulsions with eight different CE:TG molar ratios, ranging from 0:10 to 10:0. (T) Calibration curve for quantification of CE percentage out of total neutral lipid. (U) Mass spectra of lipids extracted from normal prostate and high-grade PCa tissues.

(Gleason grade 3), high-grade PCa (Gleason grade 4), metastatic PCa (liver), and pure cholesteryl oleate. The autofluorescent granules seen in normal prostate consistently showed readily detectable bands for lipid (1200-1800 cm^{-1}), phenylalanine (~1000 cm^{-1}), and prominent CH_3 stretching (~2930 cm^{-1}), but lacked the characteristic C=O ester stretching band at 1742 cm^{-1} (Figure 2.2P). These data suggest that the autofluorescent granules are primarily composed of unesterified lipids and proteins. Similar Raman profiles were seen in both BPH and PIN lesion (Figure 2.2Q). Importantly, the spectra of intracellular LDs in low-grade, high-grade, and metastatic PCa (Figure 2.1N) were distinctly different from those collected in normal prostate, BPH, and PIN lesions, but nearly identical to the spectrum of pure cholesteryl oleate, with characteristic bands at 428, 538, 614 and 702 cm^{-1} for cholesterol ring and for ester bond at 1742 cm^{-1} [259]. Spectra taken from various LDs in the same cancer specimen are nearly identical (Figure 2.2R), which allowed quantitation of CE percentage. Given that neutral lipids in LDs are predominantly TG and CE [81], we recorded Raman spectra of mixed emulsions containing cholesteryl oleate and glyceryl trioleate (Figure 2.2S). We found that the height ratio between the most prominent cholesterol band at 702 cm^{-1} and the CH_2 bending band at 1442 cm^{-1} was linearly proportional to the molar percentage of CE present in the total lipids (Figure 2.2T). Based on this calibration curve, we found that LDs were ubiquitously rich in CE independent of the types of PCa, specifically 90.2 ± 9.1 % for low-grade, 90.6 ± 4.9 % for high-grade, and 70.3 ± 18.5 % for metastasis (Figure 2.1O, Table 2.1). Electrospray ionization mass spectrometry analysis of extracted lipids from tissues confirmed that CE accumulated in high-grade PCa, but not in normal

Table 2.1 Detection of LDs and autofluorescent granules in prostate specimens from healthy donors and PCa patients

	Autofluorescent granule	LD area fraction (%)	LD area fraction Mean ± SD[a](%)	CE percentage (%)	CE percentage Mean ± SD (%)
Normal [b] (n = 19)	Positive	ND [c]			
BPH (n = 10)	Positive	ND			
Prostatitis (n = 3)	Negative	ND			
PIN (n = 3)	Positive	ND			
Low-grade PCa (Gleason 3, n = 9) [d]	Negative	0.155	0.78 ± 0.65	69.9	90.2 ± 9.1
		1.376		97.7	
		0.527		94.2	
		0.146		88.1	
		0.709		101.3	
		0.998		92.6	
		2.084		84.0	
		0.145		92.6	
		0.909		91.6	
High-grade PCa (Gleason 4/5, n = 11) [e]	Negative	3.974	3.93 ± 1.74	84.0	90.6 ± 4.9
		2.466		99.6	
		6.094		86.1	
		4.831		88.5	
		4.940		83.5	
		1.830		93.2	
		3.275		94.5	
		3.030		91.3	
		6.391		89.1	
		1.100		91.7	
		5.279		94.6	
Metastases [f] (n = 9)	Negative	1.431	2.76 ± 1.19	89.0	70.3 ± 18.5
		3.998		82.0	
		3.006		44.6	
		4.311		42.4	
		3.364		60.7	
		3.622		82.8	
		0.996		60.6	
		2.364		82.9	
		1.710		88.1	

[a] SD = standard deviation

[b] Normal prostate tissues were collected from healthy donors (n = 3) and PCa patients (n = 16).

[c] ND = not detectable

[d] Borderline cases (Gleason 3): one tissue specimen does not have any lipid accumulation; two tissue specimens only contain autofluorescent granules but not LDs.

[e] Borderline case (Gleason 4/5): one tissue specimen only contain autofluorescent granules but not LDs.

[f] Metastases: liver (n = 2), lymph node (n = 3), rib (n = 1), lung (n = 1), adrenal (n = 1), and abdominal soft tissue (n = 1)

prostate, and further showed that cholesteryl oleate was the dominant species (Figure 2.2U).

2.3.2 CE Accumulation in PCa Is Not Correlated with Androgen Signaling

Because the AR remains transcriptionally active in castration-resistant PCa [185], and cholesterol is the precursor of the entire androgen synthesis cascade, we first speculated that CE accumulation is associated with androgen signaling in PCa. To test this hypothesis, we examined non-transformed human prostate epithelium and a panel of human PCa cells (Figure 2.3A, B, Table 2.2). As shown in Figure 2.3C, the LDs in non-transformed prostate RWPE1 cells showed a low CE level (< 20%), which remained low upon addition of 10% FBS into the culture medium (Figure 2.4A). For AR-negative cancer cells, we examined bone metastasis-derived PC-3 and brain metastasis-derived

Table 2.2 Origin, AR expression, androgen dependence, and PTEN status in various human prostate cells

Cell lines	Origin	AR expression	Androgen dependence	PTEN
RWPE1	Normal prostate	+	Dependent	Normal
LNCaP-LP	Lymph node metastasis	+	Dependent	Mutated
LNCaP-HP	Lymph node metastasis	+	Independent	Mutated
PC-3	Bone metastasis	-	Independent	Deleted
DU145	Brain metastasis	-	Independent	Normal
C4-2	Derivative of LNCaP-LP by passing through castrated mice	+	Independent	Mutated
22Rv-1	Derivative of CWR22 (primary PCa cell) by passing through castrated mice	+	Independent	Normal

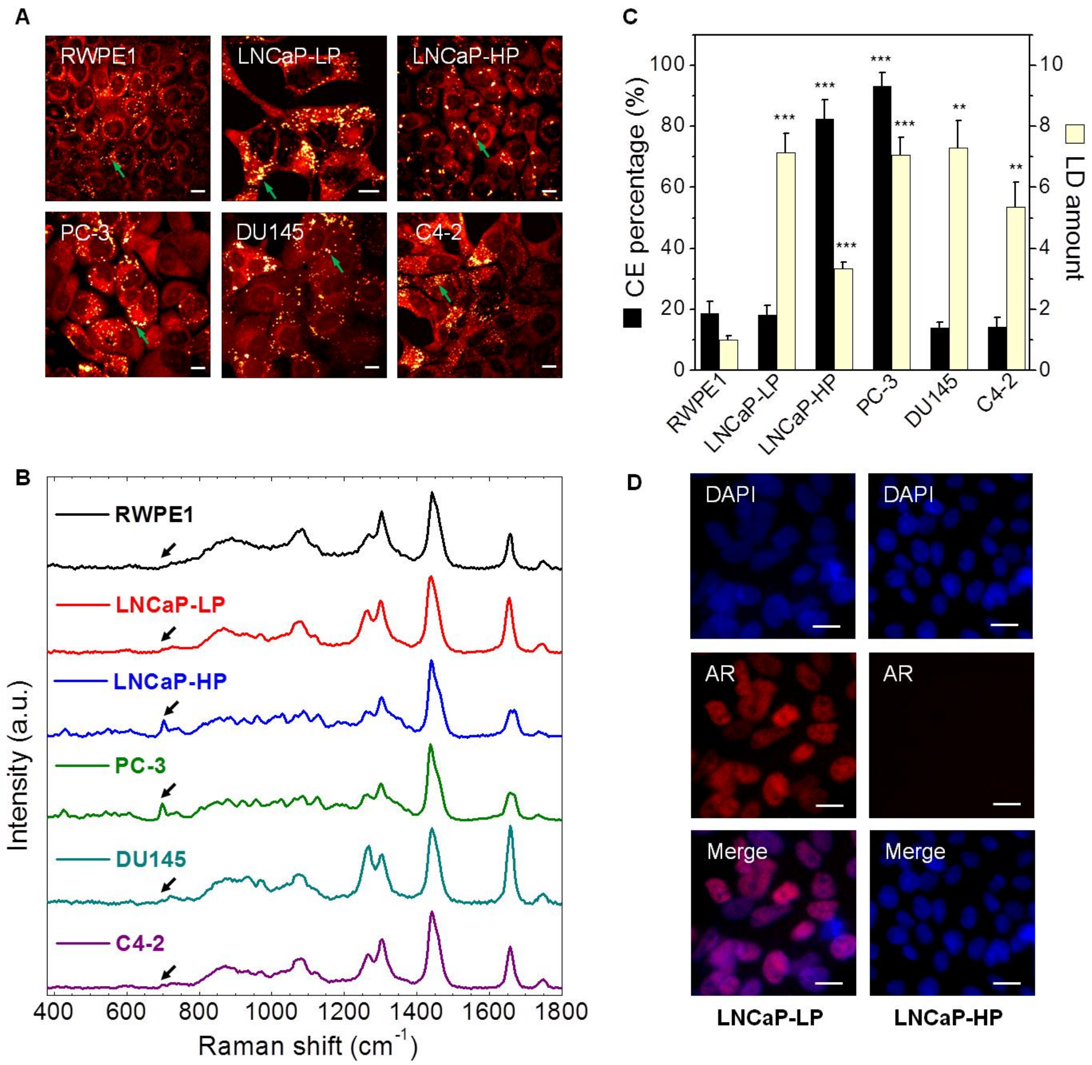

Figure 2.3 CE accumulation is not correlated with androgen signaling. (A) SRL images of various types of cells, including RWPE1, LNCaP-LP, LNCaP-HP, PC-3, DU145, and C4-2. LDs indicated by green arrows. (B) Raman spectra of LDs in different cell lines shown in (A). Spectral intensity was normalized by the peak at 1442 cm^{-1}. Black arrows indicate the bands of cholesterol rings at 702 cm^{-1}. (**C**) Quantitation of LD amount and CE percentage. LD amount was normalized by the RWPE1 group. Error bars represent SEM. n > 5. **: $p < 0.005$, ***: $p < 0.0005$. (**D**) Nuclear translocation of AR in LNCaP-LP and LNCaP-HP cells. Blue: DAPI, Red: AR immunofluorescence. Scalar bar, 10 µm.

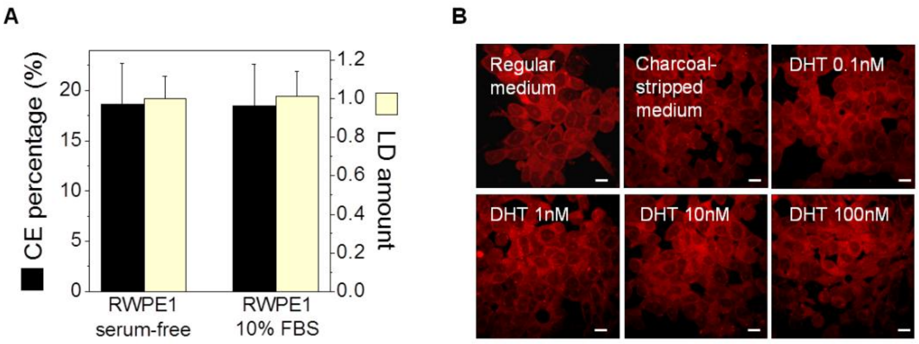

Figure 2.4 CE measurements of RWPE1 and 22Rv-1 cells in various culture conditions. (A) CE measurement of RWPE1 cells cultured in regular serum-free medium and the medium supplemented with 10% FBS. (B) SRL images of 22Rv-1 cells treated with different concentrations of dihydrotestosterone (DHT). DHT was diluted in phenol-red free RPMI + 10% charcoal-stripped serum, 4 days incubation. Scalar bar, 10 µm.

DU145, and found that CE level was high in PC-3 (> 90%) but low in DU145 (< 20%). For AR-positive cancer cells, we used low passage LNCaP (LNCaP-LP) and high passage LNCaP (LNCaP-HP) as models for PCa progression [244]. The CE level was high (> 80%) in the androgen-independent LNCaP-HP, but low (< 20%) in the androgen-dependent LNCaP-LP. Notably, LD accumulation in LNCaP-LP was reported and attributed to the upregulation of FASN [87, 88]. Our data showed a dramatic increase of CE levels in LDs during progression of LNCaP cells from androgen-dependent to androgen-independent stage. Meanwhile, a key step of androgen signaling, nuclear translocation of AR, was seen in CE-poor LNCaP-LP cells but not in CE-rich LNCaP-HP cells (Figure 2.3D). Finally, we found, in AR-positive and androgen-independent C4-2 and 22Rv-1 cells, that CE level was low (< 20%) in C4-2 cells (Figure 2.3C) and LD accumulation remained low upon dihydrotestosterone treatment in 22Rv-1 cells (Figure

2.4B). These data collectively imply that CE accumulation may be linked to a pathway that is independent of androgen signaling.

2.3.3 CE Accumulation Is Driven by Loss of PTEN and Consequent Upregulation of PI3K/AKT/mTOR/SREBP Pathway

The finding that CE accumulated in PC-3 cells (PTEN-deleted) but not in DU145 cells (PTEN-normal) then triggered us to ask whether CE accumulation resulted from loss of tumor suppressor PTEN, which is known to activate a pathway bypassing the AR [185]. Loss of PTEN has been widely observed in both localized and metastatic PCa and is correlated with high Gleason grade [260]. With loss of PTEN, PI3K signaling is hyperactivated, which, in turn, leads to AKT activation. The upregulated PI3K/AKT pathway has been implicated in carcinogenesis and metastasis of PCa [261, 262]. To determine the extent to which PTEN is involved, we first reintroduced wild-type PTEN into PC-3 cells and found CE levels to be significantly reduced (Figure 2.5A). Then, we knockdowned PTEN in DU145 cells using shRNA and found a significant increase in CE levels (Figure 2.5B). We further inhibited PTEN in DU145 cells using BPV (a PTEN inhibitor) and also found a significant increase in CE levels (Figure 2.6A). To determine the potential role of the PI3K/AKT/mTOR pathway in regulating CE accumulation, we treated PC-3 cells (the CE-rich cell line) with LY294002 (a selective PI3K inhibitor), MK2206 (a selective AKT inhibitor), and rapamycin (a selective mTOR inhibitor), respectively. Although total LD amounts were not markedly reduced upon inhibitor treatments (Figure 2.5C, D), CE levels were significantly reduced (Figure 2.5D),

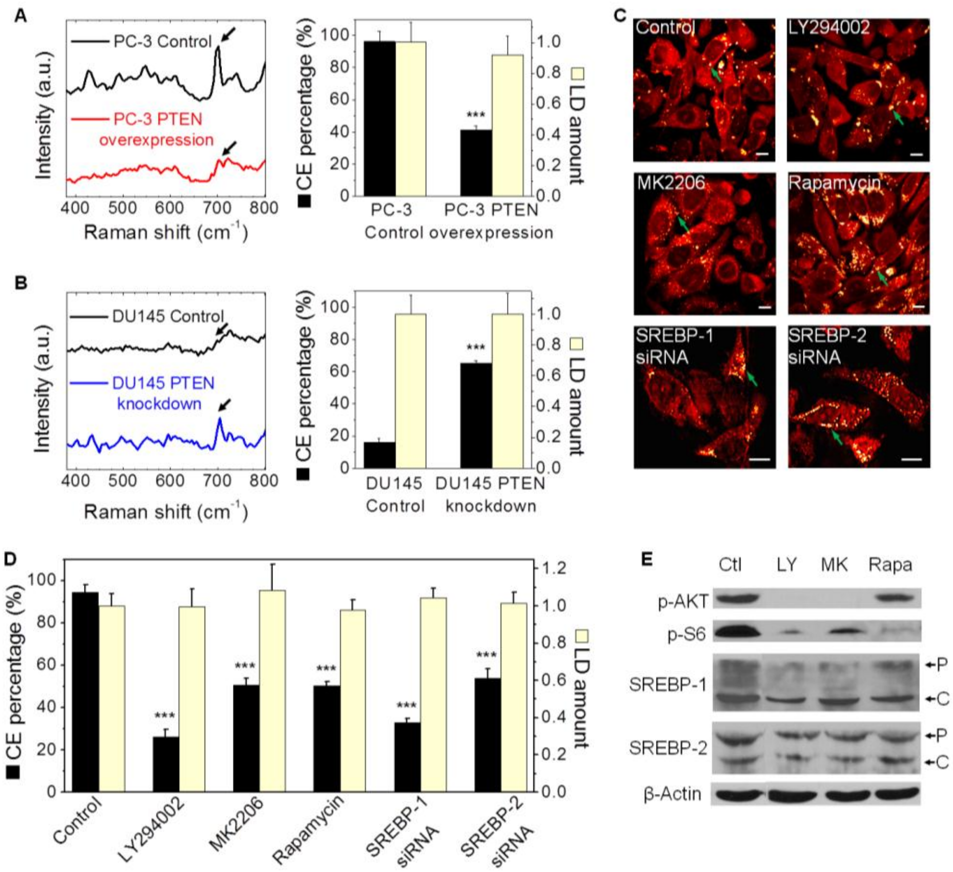

Figure 2.5 CE accumulation is induced by loss of PTEN and activation of PI3K/AKT pathway. (A) CE levels in PC-3 cells transfected with PTEN^{WT} plasmid for 3 days. Raman spectra of LDs in control and PTEN-overexpressed cells are shown on the left. The band of cholesterol rings at 702 cm^{-1} nearly disappeared after the treatment, as indicated by the arrows. Quantitation of CE percentage and LD amount is shown on the right. n > 5. (B) CE measurement of DU145 cells transfected with PTEN shRNA lentiviral particle for 3 days. Raman spectra of LDs in control and transfected cells are shown on the left. The band of cholesterol rings at 702 cm^{-1} significantly increased after the treatment, as indicated by the arrows. Quantitation of CE percentage and LD amount is shown on the right. n > 5. (C) SRL images of cells treated with DMSO as control, LY294002 (50 µM, 3d), MK2206 (10 µM, 2d), rapamycin (100 nM, 2d), and SREBP-1 and -2 siRNA (2d transfection). LDs indicated by green arrows. Scalar bar, 10 µm. (D) Quantitation of CE percentage and LD amount in cells shown in (C). n > 5. (E) Immunoblot of the antibodies against p-AKT, p-S6, SREBP-1 and -2, and β-Actin in cells treated with DMSO as control (Ctl), LY294002 (LY), MY2206 (MK), and rapamycin (Rapa). P: precursor form, C: cleaved form. The expression levels of p-AKT and p-S6 were reduced after inhibitor treatments as expected. Error bars represent SEM. ***: $p < 0.0005$.

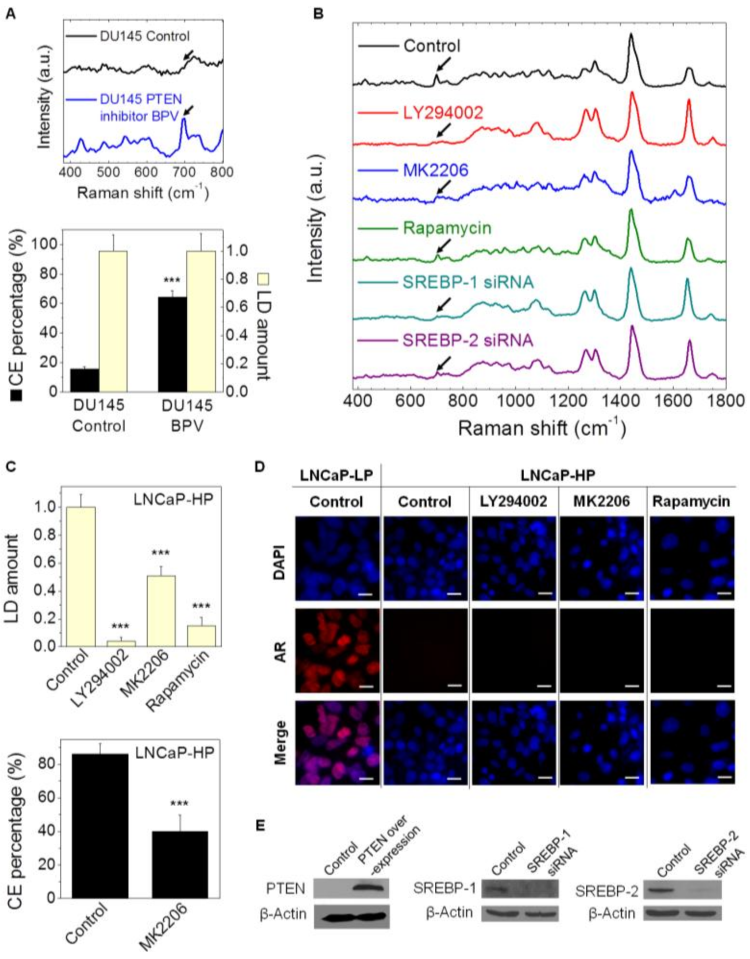

Figure 2.6 CE accumulation is not correlated with androgen signaling, but rather induced by loss of PTEN and activation of PI3K/AKT pathway. (A) CE measurement of DU145 cell treated with a potent inhibitor of PTEN, BPV(pic) (10 µM) for 3 days. Raman spectra of LDs in control and transfected cells are shown on the upper row. The band of cholesterol rings at 702 cm^{-1} significantly increased after the treatment, as indicated by the arrows. Quantitation of CE percentage and LD amount is shown on the bottom row. n > 5. (B) Raman spectra of LDs in PC-3 cells undergone various treatments including LY294002 (50 µM, 3d), MK2206 (10 µM, 2d), rapamycin (100 nM, 2d), SREBP-1 and -2 siRNA (2d transfection). The bands of cholesterol rings at 702 cm^{-1} were significantly reduced after the treatments, as indicated by the arrows. (C) LD amount and CE percentage of LNCaP-HP cells treated with DMSO as control, LY294002 (50 µM, 3d), MK2206 (10 µM, 2d), and rapamycin (100 nM, 2d). (D) Immunofluorescence images of DAPI (blue) and AR (red) in LNCaP-LP cells and LNCaP-HP cells treated with DMSO as control, LY294002, MK2206, and rapamycin. (E) Immunoblot of the antibodies against PTEN, SREBP-1 or -2 (precursor forms), and β-Actin in control, PTEN overexpressed, SREBP-1 or -2 siRNA-transfected PC-3 cells.

as shown by spectral analysis (Figure 2.6C). We have also inhibited PI3K/AKT/mTOR pathway in LNCaP-HP cells and found that both LD amount and CE levels were significantly reduced upon inhibitor treatments (Figure 2.6D). In the meanwhile, AR translocation was still not detected in the LNCaP-HP cells upon inhibition of PI3K/AKT/mTOR pathway (Figure 2.6E), which further supports that CE accumulation is not correlated with androgen signaling.

It is known that AKT mediates the activation of mTOR complex 1 that plays a critical role in regulating the function of SREBPs [69]. The SREBPs are transcription factors that function to control lipid and cholesterol homeostasis by sensing cellular cholesterol [70]. Increased activation of SREBPs was found in advanced PCa [183]. Using RNA interference, we found that knockdown of both SREBP-1 and -2 led to significant reduced CE levels in PC-3 cells without affecting LD amount, and knockdown of SREBP-1 resulted in a stronger effect than knockdown of SREBP-2 (Figures 2.5C, D, and 2.6C). Using immunoblotting, we further found that inhibition of the PI3K/AKT/mTOR pathway significantly suppressed both the level and cleavage of SREBP-1 in PC-3 cells (Figure 2.5E), indicating that CE accumulation is closely related to the activity of SREBP-1 isoforms. These results collectively suggest that CE accumulation is regulated by the PI3K/AKT/mTOR/SREBP pathway.

2.3.4 CE Accumulation in PCa cells Arises from Enhanced Uptake of Exogenous LDL

Because cholesterol can be either *de novo* synthesized via the mevalonate pathway or taken up from exogenous lipoproteins, we investigated the source of

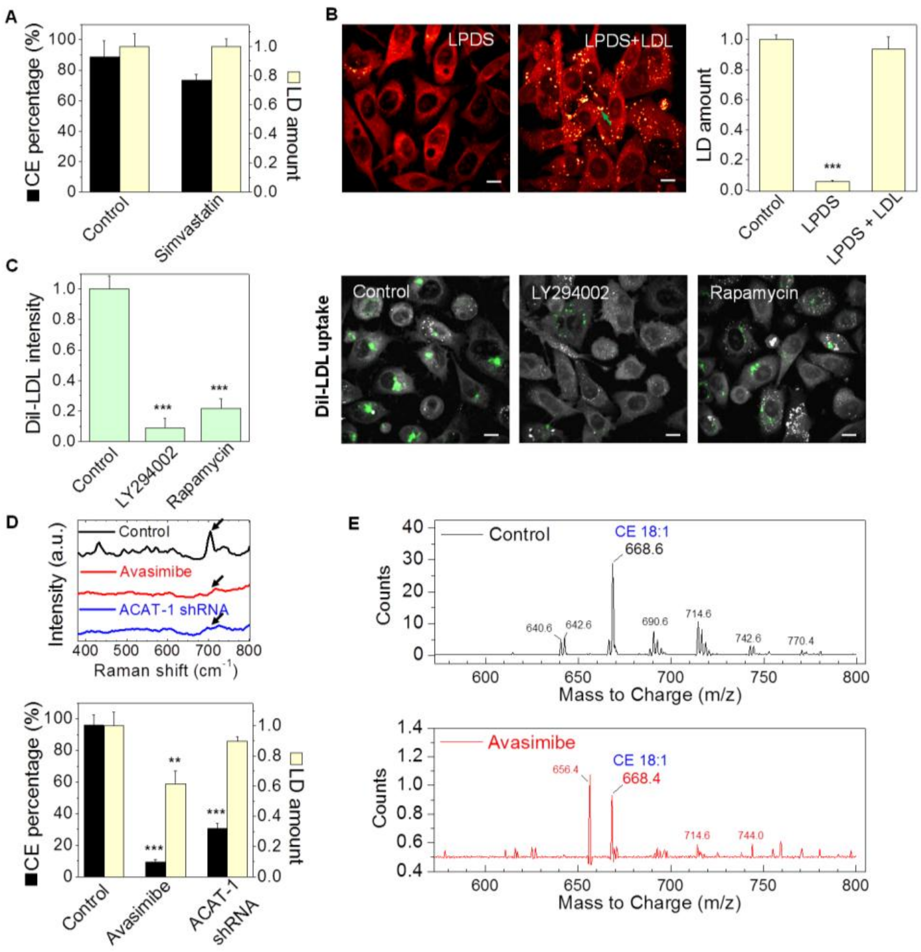

Figure 2.7 CE accumulation arises from enhanced uptake of exogenous LDL and involves cholesterol esterification by ACAT-1. (A) LD amount and CE percentage in PC-3 cells treated with or without simvastatin (10 µM, 1d), n > 5. (B) SRL images and quantitation of LD amount in PC-3 cells treated with LPDS (10%, 1d) and subsequent LDL re-addition (45 µg/ml, 1d), n = 6. LDs indicated by green arrows. (C) Quantitation and representative images of DiI-LDL uptake by PC-3 cells treated with DMSO as control, LY294002, and rapamycin (grey: SRL, green: two-photon fluorescence), n = 5. DiI-LDL intensity was normalized by the control group. (D) Raman spectra of LDs and quantitation of LD amount and CE percentage in PC-3 cells treated with avasimibe (7.5 µM, 1d) and ACAT-1 shRNA (3d transfection). n > 5. Spectral intensity was normalized by the peak at 1442 cm^{-1}. The bands of cholesterol rings at 702 cm^{-1} nearly disappeared after the treatments, as indicated by the arrows. LD amount was normalized by the control group in (B, D). (E) Mass spectra of lipids extracted from control and avasimibe-treated PC-3 cells (7.5 µM, 2d). The m/z 668 peak stands for cholesteryl oleate (CE 18:1). Error bars represent SEM. **: $p < 0.005$, ***: $p < 0.0005$. Scalar bar, 10 µm. LPDS: lipoprotein deficient serum; DiI-LDL: DiI-LDL.

cholesterol used for CE accumulation. We first treated PC-3 cells with simvastatin, an inhibitor of HMGCR, the rate-limiting enzyme of the mevalonate pathway. As shown in Figure 2.7A, simvastatin neither decreased LD amount nor significantly reduced CE levels. In contrast, after treating cells with lipoprotein-deficient serum, LDs nearly disappeared in CE-rich PC-3 cells (Figure 2.7B), but remained the same amount in CE-poor cells, including LNCaP-LP, DU145, and C4-2 (Figure 2.8A-B). Re-addition of LDL into the lipoprotein-deficient medium restored LDs in PC-3 cells (Figure 2.7B) and the CE level in these LDs was 93.6 ± 5.5 %. By treating cells with DiI-LDL, it was found that LDL uptake was the most prominent in the CE-rich PC-3 cells compared to CE-poor PCa cells (Figure 2.8C-D). Moreover, inhibition of the PI3K/AKT/mTOR pathway significantly reduced expression levels of LDLr (Figure 2.8E) and blocked the uptake of DiI-LDL in PC-3 cells (Figure 2.7C). Knockdown of SREPB-1 using siRNA also reduced the LDL uptake in PC-3 cells (Figure 2.8F). These results collectively indicate that exogenous LDL is the primary source for CE accumulation.

2.3.5 CE Accumulation in PCa Cells Requires Cholesterol Esterification by ACAT-1

LDL is known to enter a cell via LDLr and traffic to the late endosome and lysosome to be hydrolyzed to FFAs and free cholesterol. The excess free cholesterol together with the fatty acyl CoA substrate is then converted to CE by ACAT and stored in LDs [170]. Thus, we treated cells separately with avasimibe and Sandoz 58-035, two different ACAT inhibitors. Both inhibitors effectively suppressed CE accumulation in PC-3 cells (Figures 2.7D, 2.8G), with the amount of LDs slightly decreased (Figure 2.7D).

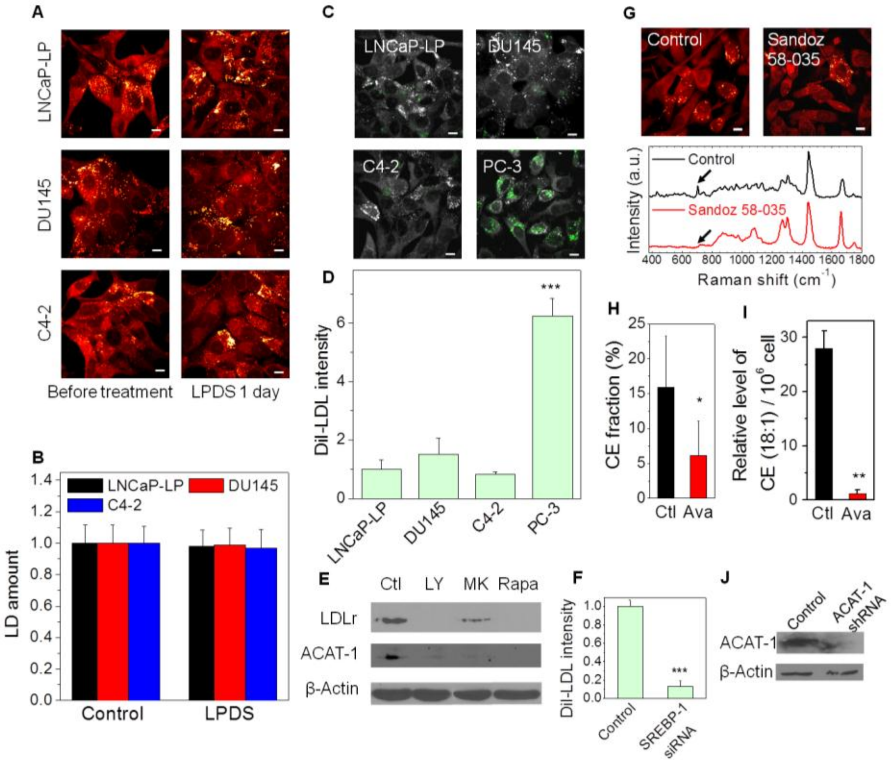

Figure 2.8 LDs in CE-poor cells do not arise from exogenous LDL, whereas CE accumulation in CE-rich cells arises from enhanced uptake of exogenous LDL. (A-B) Representative SRL images and quantitation of LD amount of various CE-poor cancer cells, including LNCaP-LP, DU145, and C4-2, before and after LPDS treatment (1d). LD amounts in cells before treatments were normalized for each cell line. (C-D) Representative images and quantitation of DiI-LDL uptake in various cell lines, including RWPE1, LNCaP-LP, LNCaP-HP, PC-3, DU145, and C4-2. DiI-LDL treatment: 20 µg/ml for 3 hr. Grey: SRL; Green: two-photon fluorescence. (E) Immunoblot of the antibodies against LDLr, ACAT-1, and β-Actin in PC-3 cells treated with DMSO as control, LY294002 (50 µM, 3d), MK2206 (10 µM, 2d), and rapamycin (100 nM, 2d). (F) Quantitation of DiI-LDL uptake in PC-3 cells transfected with SREBP-1 siRNA. (G) SRL images and Raman spectra of LDs in PC-3 cells with and without Sandoz 58-035 treatment (10 µM, 1d). The bands of cholesterol rings at 702 cm^{-1} nearly disappeared after the treatments, as indicated by the arrows. (H) Effect of avasimibe treatment (7.5 µM, 2d) on fraction of CE out of total cholesterol in PC-3 cells, measured by biochemical assay. (I) Relative levels of cholesteryl oleate (CE 18:1) in control and avasimibe-treated PC-3 cells (7.5 µM, 2d), measured by mass spectrometry and normalized by cell number (n = 3). (J) Immunoblot of the antibodies against ACAT-1 and β-Actin in control and ACAT-1 siRNA-transfected PC-3 cells. Scalar bar = 10 µm. Error bars represent SEM. *: $p < 0.05$. **: $p < 0.005$, ***: $p < 0.0005$. LPDS: lipoprotein deficient serum; DiI-LDL: DiI-LDL.

The significant reduction of CE accumulation upon avasimibe treatment was verified by biochemical assay (Figure 2.8H) and mass spectrometry of extracted lipids from PC-3 cells (Figures 2.7E, 2.8I). The mass data further showed that cholesteryl oleate was the dominant species present. Because avasimibe inhibits both ACAT-1 and -2 isoforms, we specifically knocked down ACAT-1 using shRNA and found significant reduction of the CE level in PC-3 cells (Figures 2.7D, 2.8J). In addition, inhibition of PI3K/AKT/mTOR pathway significantly reduced expression levels of ACAT-1 (Figure 2.8E). These results collectively confirm the involvement of ACAT-1 in CE storage in PCa cells.

2.3.6 Pharmacological Depletion of CE Storage Impairs PCa Aggressiveness

Because CE accumulation was found in PCa but was not detectable in normal prostate, we evaluated how cell viability could be affected by regulating CE levels with ACAT inhibitors. As shown in Figure 2.9A and Figure 2.10A, treatments of two ACAT inhibitors, avasimibe and Sandoz 58-035, significantly reduced viability of PC-3 cells, with IC50 value of 7.3 µM and 17.2 µM, respectively. The inhibitory effect of avasimibe on the growth of PC-3 and LNCaP-HP cells was considerably greater than that in CE-poor PCa cells, including LNCaP-LP, DU145, and C4-2 (Figure 2.10B), with IC50 value of 9.6 µM in LNCaP-HP cells (Figure 2.10C). Results from flow cytometry analysis (Figure 2.9B) revealed that exposure of PC-3 cells to avasimibe resulted in both cell cycle arrest and apoptosis, i.e. the G2/M phase population was ~2 times smaller whereas the sub-G1 population was ~3 times larger in avasimibe-treated group compared to control group. To confirm the effect of ACAT inhibition on cell viability, we treated PC-3 cells with a potent and selective inhibitor of diacylglycerol acyltransferase (DGAT)-1,

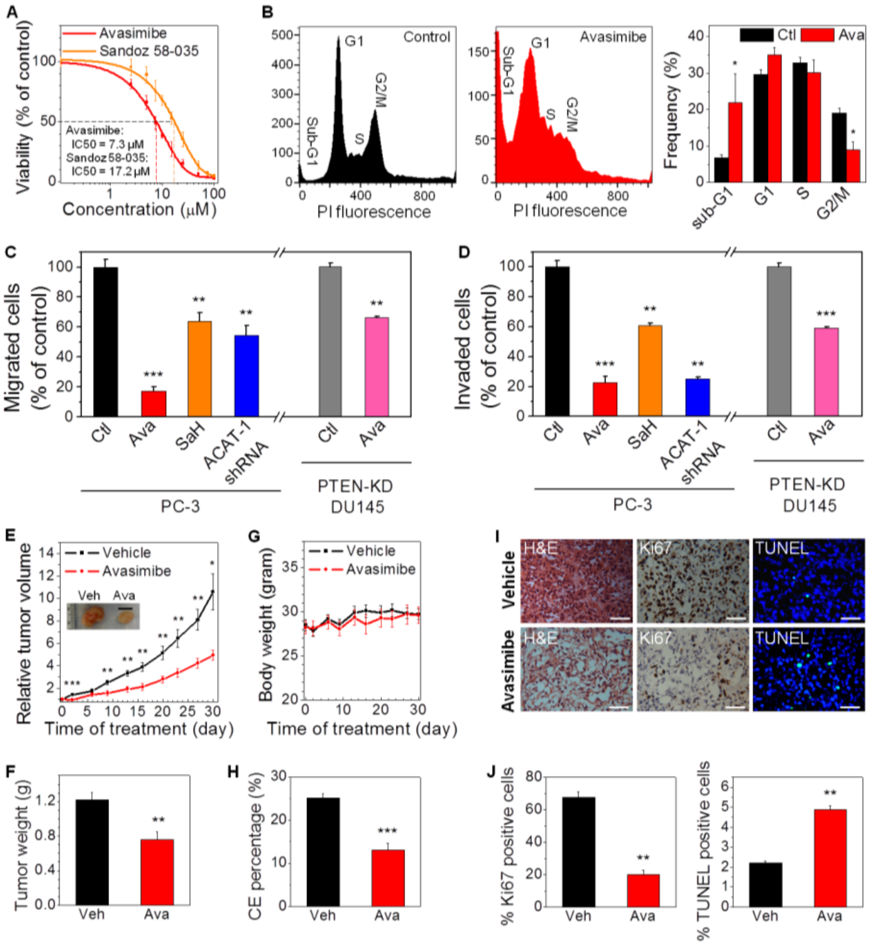

Figure 2.9 CE depletion impairs human PCa aggressiveness. (A) IC50 curves of avasimibe and Sandoz 58-035 treatments on PC-3 cells. n = 6 per group. (B) Flow cytometry analysis of cell cycle in control and avasimibe-treated PC-3 cells (n = 3). (C, D) Quantitation of migrated and invaded PC-3 cells that were pretreated with DMSO as control, avasimibe (5 μM), Sandoz 58-035 (SaH, 10 μM), and ACAT-1 shRNA for 2d (n = 3). And quantitation of migrated and invaded PTEN knockdown (PTEN-KD) DU145 cells that were pretreated with DMSO as control and avasimibe (5 μM) for 1d (n = 3). (E) Relative tumor volume of PC-3 xenograft (n = 9). Relative tumor volume = tumor volume / initial tumor volume (day 0) for each mouse. Representative tumors harvested on day 30 are shown in the inset. Scalar bar, 1 cm. (F) Weight of tumor tissues harvested from mice (n = 8). (G) Body weight of mice over 30-day treatments (n = 9). (H) CE percentage of tumor tissues harvested from mice (n = 5). (I) Representative images of H&E staining, IHC of Ki67, and TUNEL labeling (blue: DAPI, cyan: TUNEL-positive) of vehicle and avasimibe groups. Scalar bar, 100 μm. (J) Percentage of Ki67 and TUNEL positive cells in vehicle and avasimibe groups (n = 5). Error bars represent SEM. *: $p < 0.05$, **: $p < 0.005$, ***: $p < 0.0005$.

which catalyzes the terminal step of TG formation, and found that DGAT inhibition did not affect cell viability until high doses (Figure 2.10C). We also showed that specific knockdown of ACAT-1 using shRNA significantly reduced viability of PC-3 cells (Figure 2.10D). Moreover, ACAT inhibition by avasimibe significantly suppressed viability of PTEN knockdown DU145 cells (Figure 2.10D). To evaluate whether CE depletion affects tumor aggressiveness, we conducted standard transwell assays and found that both migration and invasion capabilities of PC-3 cell were markedly suppressed upon ACAT inhibition by avasimibe, Sandoz 58-035, and ACAT-1 shRNA (Figures 2.9C, D, 2.10E). And also in PTEN knockdown DU145 cells, ACAT inhibition by avasimibe significantly suppressed cell migration and invasion capabilities (Figure 2.9C, D). In contrast, DGAT inhibition slightly increased PC-3 cell migration and invasion (Figure 2.10F). Notably, negligible toxic effects on non-transformed prostate RWPE1 cells were found at the same dose of avasimibe treatments (Figure 2.10B).

To test the potential of using ACAT inhibition to treat advanced PCa *in vivo*, we administered two ACAT inhibitors, avasimibe and Sandoz 58-035 (15 mg/kg, via intraperitoneal injection), to athymic nude mice bearing PC-3 xenografts. Daily treatment of mice with ACAT inhibitors inhibited the growth of PC-3 tumors by ~2 fold (Figures 2.9E, 2.10G), and significantly reduced weight of tumor tissues (Figures 2.9F, 2.10H). Importantly, ACAT inhibitors did not cause general toxicity to animals, as indicated by no change observed in animal behavior or body weight (Figures 2.9G, 2.10I). Pathological review of sections of heart, kidney, liver, lung, and spleen harvested from mice receiving avasimibe showed no detectable signs of toxicity (Figure 2.10J). Spectroscopic imaging of extracted tissues revealed that CE levels significantly dropped

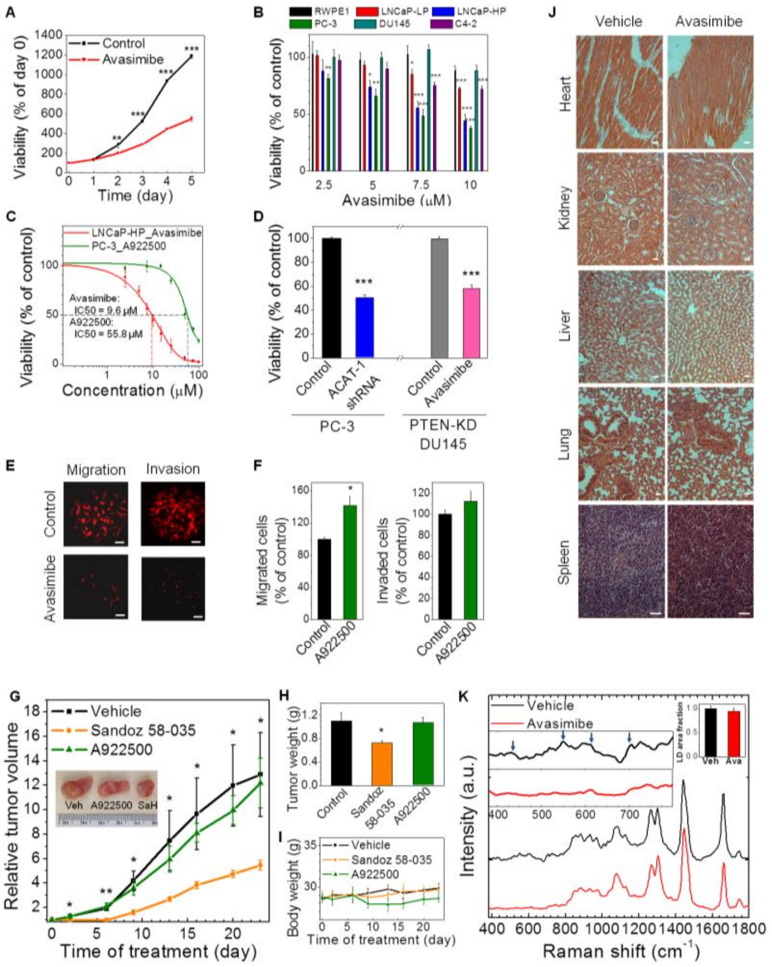

Figure 2.10 CE depletion using various ACAT inhibitors or RNA interference suppresses PCa viability and growth *in vivo* with negligible toxicity. (A) Proliferation curves of control and avasimibe-treated PC-3 cells (n = 6). (B) Viability of various cell lines, including RWPE1, LNCaP-LP, LNCaP-HP, PC-3, DU145, and C4-2, treated with avasimibe. n = 6 per group. (C) IC50 curves of avasimibe treatment on LNCaP-HP cells and DGAT-1 inhibitor A922500 treatment on PC-3 cells. n = 6 per group. (D) Viability of PC-3 cells transfected with ACAT-1 shRNA for 3 days. And viability of PTEN knockdown (PTEN-KD) DU145 cells treated with avasimibe (7.5 µM) for 2 days. (E) Images of migration and invasion of PC-3 cells pre-treated with avasimibe (5 µM, 2d). Red: PI staining. Scalar bar, 50 µm. (F) Quantitation of migrated and invaded PC-3 cells pre-treated with DGAT-1 inhibitor A922500 (10 µM, 2d), n = 3. (G) Relative tumor volume of PC-3 xenograft (n = 8). (H) Weight of tumor tissues (n = 8). (I) Body weight of mice (n = 8). (J) H&E staining of tissue sections. Scalar bar, 100 µm. (K) Raman spectra of PC-3 tumor tissues. Error bars represent SEM. *: $p < 0.05$. **: $p < 0.005$, ***: $p < 0.0005$.

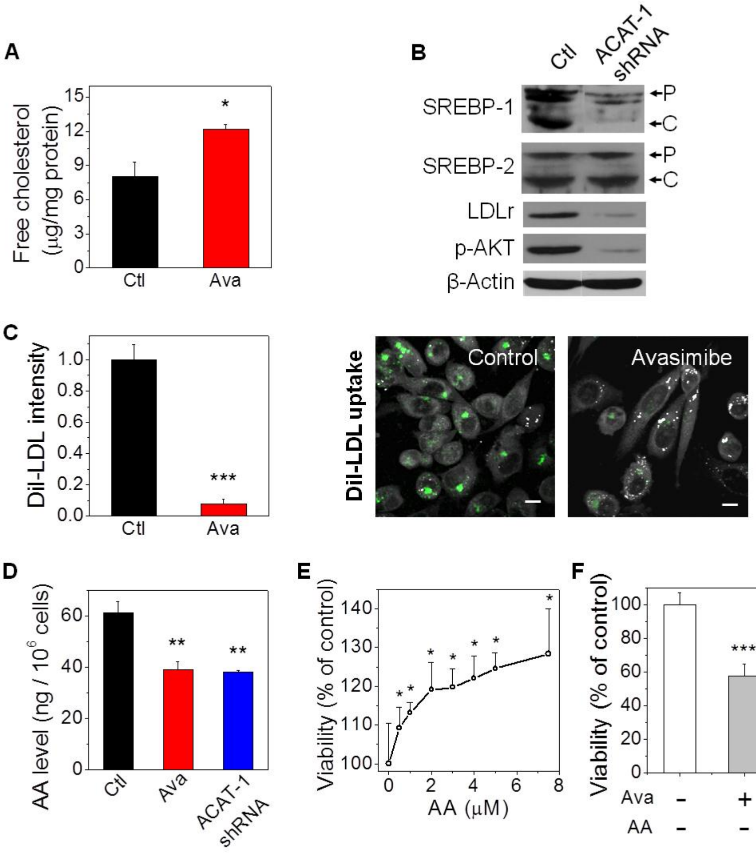

Figure 2.11 CE depletion reduces human PCa cell proliferation by limiting uptake of essential fatty acids. (A) Free cholesterol level in control (Ctl: DMSO as control) and avasimibe (Ava)-treated PC-3 cells (n = 3). (B) Immunoblot of the antibodies against SREBP-1 and -2, LDLr, p-AKT, and β-Actin in ACAT-1 knockdown PC-3 cells. P: precursor form, C: cleaved form. (C) Quantitation and representative images and of DiI-LDL uptake in control and avasimibe-treated PC-3 cells (n = 5). Grey: SRL; Green: two-photon fluorescence. Scalar bar, 10 µm. DiI-LDL intensity was normalized by the control group. (D) AA levels in control and avasimibe-treated PC-3 cells (n = 3). (E) PC-3 cell viability upon AA treatments. (F) PC-3 cell viability upon AA and/or avasimibe treatments. Viability was measured by MTT assay. The absorbance value measured for control group was used for normalization. Comparisons were made between control and treated groups (n = 6 per group). Error bars represent SEM. *: $p < 0.05$, ***: $p < 0.0005$.

in avasimibe-treated tumors compared to vehicle-treated ones, even though LD area fraction was not affected (Figures 2.9H and 2.10K), indicating that ACAT inhibitor worked to inhibit CE formation in tumor cells *in vivo*. IHC using markers for proliferation (Ki67) and apoptosis (TUNEL) showed that ACAT inhibitor avasimibe significantly reduced tumor proliferation by ~70% and increased apoptosis by ~2 fold (Figure 2.9I, J).

2.3.7 CE Depletion Impairs PCa Growth by Limiting Uptake of Essential Fatty Acids

We first suspected that CE storage might act as a pool of fatty acid and cholesterol which can be released from LDs for cancer cell proliferation. The result that inhibition of CE hydrolysis using diethylumbelliferyl phosphate, a selective cholesterol esterase inhibitor, slightly enhanced PC-3 cell growth (Figure 2.12A) excluded such possibility. We then asked whether CE depletion suppresses PCa proliferation by downregulation of the upstream pathways including LDL uptake. We notice that LDL is the primary carrier of essential PUFAs, including AA [263]. Inside cells, AA is released from LDL and converted to a range of eicosanoids that have been implicated in various pathological processes, including inflammation and cancer [77]. Because cholesterol esterification is known to play a vital role in maintaining intracellular cholesterol homeostasis [170], we hypothesized that abrogating ACAT activity can inhibit PCa growth by elevating free cholesterol levels, downregulating expression levels of SREBP and LDLr, and consequently reducing the uptake of LDL. To test this hypothesis, we measured free cholesterol levels in PC-3 cells with a biochemical assay and found that avasimibe treatment significantly increased the free cholesterol levels (Figure 2.11A). Immunoblotting measurement showed that ACAT inhibition by specific knockdown of ACAT-1 using shRNA and the two ACAT inhibitors (avasimibe and Sandoz 58-035) resulted in reduced cleavage of SREBP-1 and downregulation of expression levels of

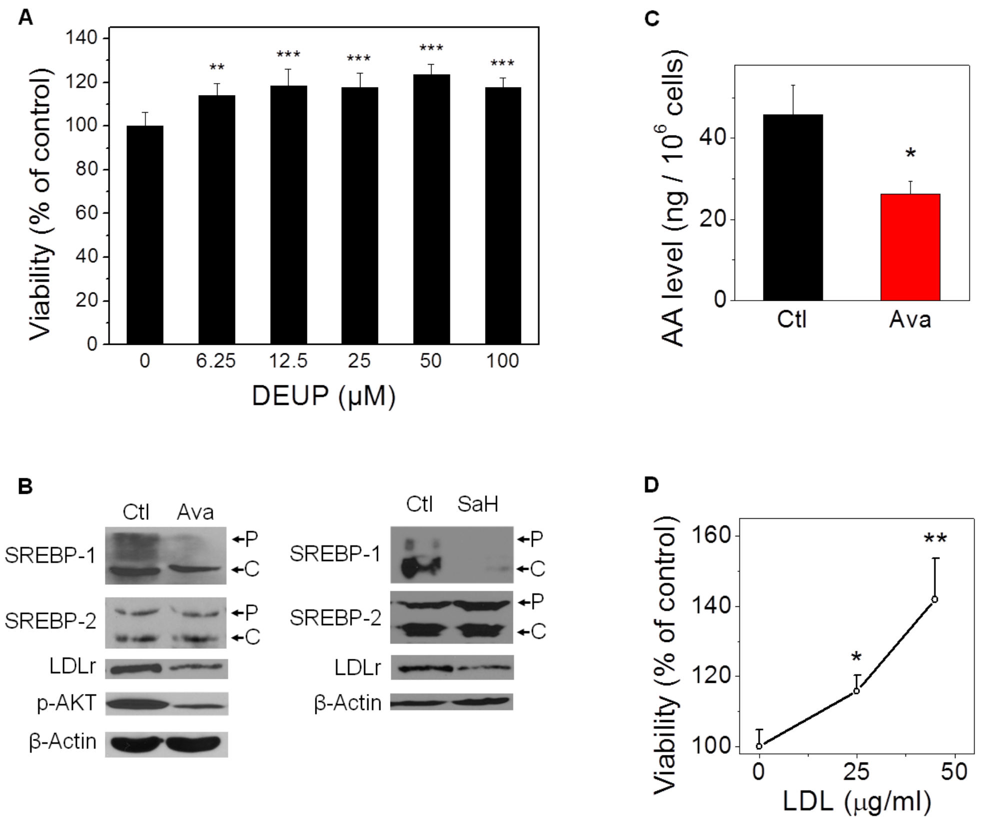

Figure 2.12 Mechanistic studies about the effects of ACAT-1 inhibition on intracellular cholesterol homeostasis. (A) Viability of PC-3 cells treated with different concentrations of CE hydrolase inhibitor, diethylumbelliferyl phosphate (DEUP), for 3 days. (B) Immunoblot of the antibodies against SREBP-1, -2, LDLr, p-AKT, and β-Actin in PC-3 cells treated with avasimibe (7.5 μM, 3d) and Sandoz 58-035 (SaH, 10 μM, 3d). P: precursor form, C: cleaved form. (C) AA levels in control and avasimibe-treated LNCaP-HP cells (n = 3). (D) PC-3 cell viability upon LDL treatments. Viability was measured by MTT assay. The absorbance value measured for control group was used for normalization. Comparisons were made between control and treated groups (n > 6 per group). Error bars represent SEM. *: $p < 0.05$, **: $p < 0.005$, ***: $p < 0.0005$.

SREBP-1, and LDLr (Figures 2.11B, 2.12B). We further monitored cellular uptake of DiI-LDL upon ACAT inhibitor treatment, and found that avasimibe treatment resulted in reduced LDL uptake by ~10 fold (Figure 2.11C). Further, liquid chromatography-mass spectrometry analysis of cell lysates revealed that ACAT-1 inhibition by both inhibitor avasimibe and shRNA significantly reduced the level of AA in PC-3 cells (Figure 2.11D), and avasimibe also significantly reduced AA levels in LNCaP-HP cells (Figure 2.12C). As shown elsewhere [264, 265] and confirmed herein, LDL and AA separately promoted the growth of PC-3 cells in a dose-dependent manner (Figure 2.11E, 2.12D). AA was also shown to rescue the inhibitory effect of ACAT inhibitor avasimibe on cancer cell viability (Figure 2.11F). Moreover, expression levels of p-AKT were significantly reduced upon ACAT-1 inhibition in PC-3 cells (Figures 2.11B, 2.12B). This might be caused by reduced levels of AA, which has been shown to activate PI3K/AKT signaling in PCa [266]. These data collectively provide evidence that ACAT inhibition might have hindered proliferation of CE-rich PCa cells by limiting the uptake of a critical proliferative factor, AA, via downregulation of LDLr. The molecular basis for CE accumulation and the impact of CE depletion on PCa proliferation are summarized in Figure 2.13.

2.4 Discussion

Through integrated analyses of PCa clinical samples, cell lines, and mouse xenograft model, we have revealed a novel role of CE, a lipid metabolite, in human PCa progression. CE accumulation is known to be a hallmark of atherosclerosis and hormone-producing organ [81, 267], however its exact role in cancer progression remains elusive. In this study, prominent CE accumulation that only occurs in advanced PCa is shown to be a consequence of the loss of tumor suppressor PTEN and subsequent activation of PI3K/AKT/mTOR pathway. Blockage of CE accumulation significantly impairs PCa aggressiveness without inducing toxicity. As discussed below, these findings improve

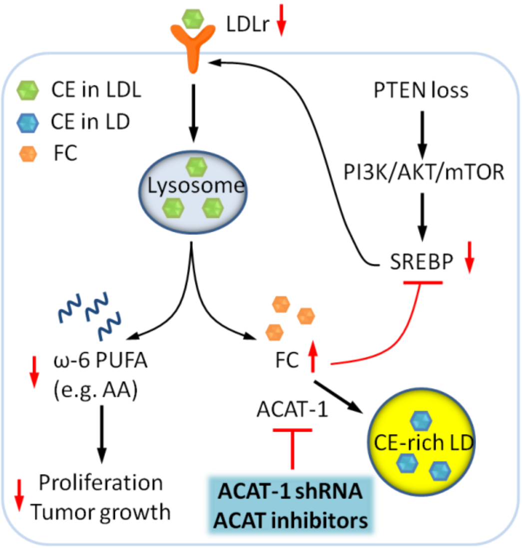

Figure 2.13 Molecular pathways underlying accumulation of CE in advanced human PCa and suppression of cancer proliferation upon CE depletion. The schematic shows that loss of tumor suppressor PTEN activates PI3K/AKT/mTOR pathway, which in turn upregulates SREBP and LDLr. LDL is then hydrolyzed to FFAs and free cholesterol (FC) in lysosome. The excess FC together with the fatty acyl CoA substrate is converted to CE by ACAT-1 and stored in LDs. LDL also serves as an important carrier of ω-6 PUFA, such as AA, which promotes cell proliferation and tumor growth. The red arrows depict the consequences of CE depletion. Depletion of CE storage by specific ACAT-1 knockdown using RNA interference or ACAT inhibitors disturbs cancer cell cholesterol homeostasis by elevating FC levels and consequently downregulating expression levels of SREBP and LDLr. Subsequently reduced uptake of ω-6 PUFA from LDL suppresses cancer proliferation.

current understanding of the role of cholesterol in cancer and also open new opportunities for diagnosis and treatment of aggressive PCa.

First, our study contributes to the understanding of metabolic pathways that drive PCa progression. Increasing evidence supports that androgen signaling pathways remain active throughout every stage of PCa progression [185]. However, expression levels of AR are heterogeneous and even absent in some metastases [268]. Such clinical observations suggest that PCa cells may also depend on other compensatory signaling pathways to survival and grow. One of the most important pathways that bypass AR is the PI3K/AKT/mTOR pathway, which is negatively regulated by the tumor suppressor PTEN. PTEN has been identified as one of the most commonly lost or mutated tumor suppressor genes in human cancers [269]. In particular, nearly 70% of advanced PCa exhibit loss of PTEN or consequent activation of the PI3K/AKT pathway [270], which leads to enhanced cell survival, proliferation, migration, invasion, metastasis, and castration-resistant growth as well [261, 270, 271]. Our results, as illustrated in Figure 2.13, show that PTEN loss induces CE accumulation by activating the PI3K/AKT/mTOR pathway and subsequently upregulating the expression levels of SREBP and LDLr. This finding elucidates the mechanism by which tumor suppressor PTEN regulates metabolic pathways to meet the increased demand of aggressive PCa cell for LDL cholesterol uptake. Our study further showed that such enhanced LDL uptake is linked to AA, a proliferation factor of PCa [264, 265].

Whereas alterations to metabolism of glucose, amino acids, and fatty acids have been extensively studied [8], cholesterol metabolism in cancer is a relatively understudied field [21]. Inside cells, cholesterol is an essential molecule that plays important roles in the maintenance of membrane structure, signal transduction, and provision of precursor to hormone synthesis [93]. As early as 1942, increased level of free cholesterol in the adenoma of enlarged prostates was reported by analysis of tissue homogenates [272]. More recently, immunohistochemical staining of PCa bone metastases showed intense staining of the LDLr, which supports the important role of LDL uptake in PCa progression [176]. However, the molecular mechanisms by which advanced PCa cells obtain sufficient cholesterol and in the meanwhile maintain intracellular cholesterol homeostasis remain poorly understood. Our imaging study of human tissues identified a possible culprit, that is, accumulation of esterified cholesterol in LDs of advanced PCa cells. Advanced PCa cells take advantage of the esterified form not only to avoid toxicity of excess cholesterol [170], but also to keep free cholesterol at relatively low level so that SREBP, which controls cholesterol biogenesis, is always active. This mechanism explains why PCa cells could maintain high expression levels of SREBP and LDLr even in the presence of exogenous cholesterol [175].

We note that statin use has been linked with a decreased risk of advanced PCa [273], and its benefits against PCa were found to be based on systemic cholesterol-lowering effect rather than direct effect on *de novo* cholesterol synthesis [274]. In accordance, our cellular studies reveal that cholesterol stored in the LDs of advanced PCa cells is not synthesized *de novo*, but rather derived from enhanced uptake of exogenous LDL. Using mass spectrometry, we find that cholesteryl oleate is the dominant species of CE inside the LDs. This result suggests that LDL with cholesteryl linoleate as the dominant form is hydrolyzed into free cholesterol and then re-esterified to CE by ACAT-1. Together, our finding offers a biological foundation that supports the beneficial effect of cholesterol-lowering drugs.

Second, our study opens a possibility of distinguishing the aggressive forms of PCa from the indolent ones that can be left without treatment. Since the introduction of prostate specific antigen screening, PCa has become the most widely diagnosed non-skin cancer in men in the United States [275]. The fact that 1410 men need to be screened and 48 cases of PCa need to be treated to prevent one death [276] has raised a controversy not only about the usefulness of prostate specific antigen screening, but also about the clinical management, of PCa. Indeed, most PCa are slowly growing, and only the aggressive ones eventually spread to other organs and require early diagnosis and effective treatment. The current standard for PCa diagnosis remains biopsy and histopathology. While PCa with Gleason score ≤ 6 (e.g. 3+3) is considered to be low-risk and is left without active treatment, PCa with Gleason score ≥ 7 (e.g. 3+4) is considered to be high-risk and is often treated with radical prostatectomy, androgen deprivation therapy, radiation, and/or chemotherapy. Nonetheless, the subjective nature of histopathology leads to inevitable discordance among pathologists. Especially for the differentiation between Gleason score 6 and 7, the inter-observer discordance can be up to 40% [277], which may result in overtreatment for some low-risk tumors and undertreatment for some high-risk tumors. Our study provides an opportunity towards more accurate prediction of aggressiveness. Because CE accumulation is quantifiable and is significantly (~5 fold) greater in Gleason grade 4/5 compared to that in Gleason grade 3, it presents a promising molecular marker to improve the current PCa diagnosis. Notably, massive CE accumulation only occurs in metastases and most of, but not all, high-grade PCa (Table 2.1). Moreover, depleting CE significantly impairs PCa aggressiveness, including survival, migration, invasion, and growth *in vivo*. These results together suggest that CE accumulation might be used for more accurate prediction of PCa aggressiveness. We note that validation of CE as an aggressiveness marker necessitates further examination of a large number of tissue biopsies and correlation assessment of CE levels and clinical outcomes of patients.

Third, our study heralds the potential of using CE as a therapeutic target for treatment of advanced PCa. While often diagnosed in clinically localized stages, PCa remains the second leading cause of cancer-related mortality in American men with over 28,000 projected deaths in 2012 [275]. For men with advanced PCa, androgen deprivation therapy is an accepted standard therapy. Despite initial disease control, androgen deprivation therapy alone is non-curative and the subsequent development of castration-resistant PCa occurs in the lifespan of almost all men who do not succumb to non-cancer deaths [185]. There has been a tremendous increase in treatment options available for metastatic castration-resistant PCa patients, including novel anti-androgen therapy [278] and others. Nevertheless, the effectiveness of current therapies is palliative with an improvement in overall survival of 2-5 months compared to placebo. In this study, we show that CE depletion by abrogating ACAT activity with avasimibe significantly hinders advanced PCa growth via cell cycle arrest and apoptosis induction. One possible explanation for such anti-cancer effect of avasimibe, as illustrated in Figure 2.13, is that depleting CE storage disrupts intracellular cholesterol homeostasis and consequently reduces the uptake of essential fatty acids, such as AA, which stimulates PCa growth and progression [264, 265]. Because CE depletion leads to elevation of free cholesterol levels, apoptosis induced by avasimibe could be due to free cholesterol toxicity. The alteration of cholesterol metabolism might also be linked to regulation of lipid rafts in PCa [193]. Importantly, the CE-depleting drug does not cause detectable toxicity in the non-transformed cell or in the mouse model. Owing to the much stronger dependence of advanced PCa on CE compared to its normal counterparts, cholesterol esterification may be a cancer-specific target for developing an effective, non-toxic anti-cancer therapy.

Blockage of cholesterol esterification with ACAT inhibitors was used to treat lymphocytic leukaemia [197], glioblastoma [279], and breast cancer [280] cells *in vitro*. In this work, we demonstrated, for the first time, its effectiveness in suppressing growth of aggressive tumor *in vivo*. We note that avasimibe was previously used to treat atherosclerosis [256] but halted by Pfizer due to the lack of effectiveness in reducing plaque size. Thus, the present study highlights a novel use of avasimibe to treat advanced PCa. Collectively, abrogating ACAT-1 activity offers a potentially effective way of treating advanced PCa.

Finally, given that the PI3K pathway is hyperactivated not only in advanced PCa, but also in many other human cancers, including brain, breast, renal, lymphocyte, cervical, and lung [67], CE accumulation in LDs might be a common characteristic of PI3K-driven cancers. Indeed, CE was found to be a proliferative factor for leukemia [197]. And dysregulation of cholesterol metabolism in glioblastoma was shown to be driven by PI3K pathway [179]. Future elucidation of the molecular mechanisms by which PI3K pathway differentially regulates cholesterol metabolism in cancer cells from multiple tissues of origin will determine whether CE is a compelling drug target across multiple cancer types. Such studies will further improve current understanding of how metabolic reprogramming is linked to oncogenic transformation.

CHAPTER 3. LABEL-FREE ANALYSIS OF BREAST TISSUE POLARITY BY RAMAN IMAGING OF LIPID PHASE

The work presented in this chapter was published in *Biophysical Journal* [281]. Reprinted with permission from [281].

The formation of the basoapical polarity axis in epithelia is critical for maintaining the homeostasis of differentiated tissues. Factors that influence cancer development notoriously affect tissue organization. Apical polarity appears as a specific tissue feature that, once disrupted, would facilitate the onset of mammary tumors. Thus, developing means to rapidly measure apical polarity alterations would greatly favor screening for factors that endanger the breast epithelium. A Raman scattering based platform was used for label-free determination of apical polarity in live breast glandular structures (acini) produced in 3D cell culture. The CARS signal permitted the visualization of the apical and basal surfaces of an acinus. Raman microspectroscopy subsequently revealed that in polarized acini lipids were more ordered at the ApM compared to BaM, and that an inverse situation occurred in acini that lost apical polarity upon treatment with Ca^{2+}-chelator EGTA. This method overcame variation between different cultures by tracking the status of apical polarity longitudinally for the same acini. Therefore the disruption of apical polarity by dietary breast cancer risk factor, ω6 fatty acid, could be observed with this method, even when the effect was too moderate to permit a conclusive assessment by traditional immunostaining method.

3.1 Introduction

With advantages over conventional 2D cell culture models that they provide by mimicking tissue-specific architectures and functions, 3D cell culture models have been increasingly used in a broad range of research, including epithelial morphogenesis, tumor biology, cell migration, regenerative medicine, and drug screening [282-284]. In particular, increased knowledge in mammary gland morphogenesis and neoplastic transformation has been obtained from studies using 3D culture of different types of mammary epithelial cells that take into account alterations in tissue architecture (i.e., the specific cellular organization within an assembly of cells) to decipher the mechanisms that control cell proliferation, survival, differentiation and resistance to chemotherapeutic drugs [285-295]. However, a wide implementation of the evolving paradigm of physiologically relevant 3D culture has been hampered by the lack of proper visualization tools to study tissue phenotypes. A tremendous challenge to quantitatively measure cellular responses in 3D cultures by conventional fluorescence microscopy is the inefficient diffusion of fluorescent dyes in thick tissue samples [283] and the fluorescent background triggered by the ECM used as cell culture substratum [296]. Continuous analyses of cellular responses over periods of time are limited to bright field microscopy and the occasional GFP-tagged expression of a specific protein. Therefore, innovations in label-free analysis of cellular responses are crucial to fully exploit the benefits of 3D cultures.

An important area of investigation is the alteration of tissue architecture that precedes tumor development. Inhibiting or reversing such alterations would play a key role in the design of prevention interventions that are so much needed. A number of factors that favor cancer development have been associated with changes in tissue architecture. Indeed, epidemiological and/or animal studies reported that estrogen and high fat diet [297], as well as obesity [298] and alcohol consumption [299] could modify mammary morphogenesis (notably the density of epithelial structures, a factor known to influence breast cancer risk).

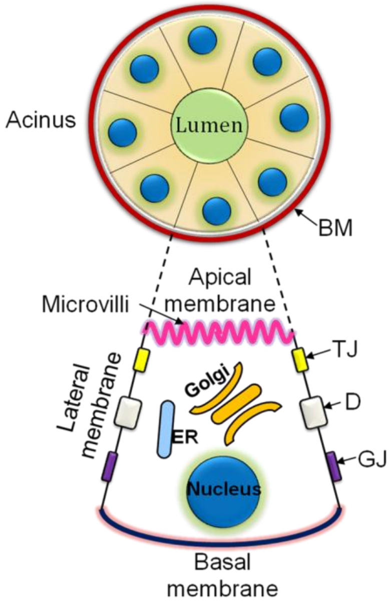

Figure 3.1 Organization of Mammary Acinus. TJ: tight junction; D: desmosome; GJ: gap junction.

Models that mimic phenotypically normal breast glandular differentiation exist and have been used to unravel pathways involved in the initiation of tumors. Cells are cultured in the presence of EHS-derived ECM, which resembles a BM, and functionally reproduce mammary glandular structures (acini) with, for certain cell lines like the HMT-

3522 S1, complete tissue polarity axis [290, 295, 296] (Figure 3.1). This axis largely determines the functional integrity of epithelia and includes both apical polarity and basal polarity [292, 300, 301]. Basal polarity is determined by the presence of specific cell-BM contacts [292]. Apical polarity is characterized by the polarized distribution of cytoplasmic organelles [301-304] and the segregation and retention of specific proteins and lipids in distinct ApM and BaM domains due to the presence of apical tight junctions [305, 306]. Functionally, the BaM facing the extracellular compartment maintains differentiation and survival, whereas the ApM facing the luminal (external) compartment mediates physiological states (e.g., quiescence) and exchange functions (e.g. absorption and secretion) [301]. Tight junctions are formed by transmembrane proteins connected to cytoplasmic proteins at the most apical side of cell-cell junctions [307, 308]. The redistribution of tight junction proteins away from apical sites is an indicator of the disruption of apical polarity [309-311]. Importantly, proteins normally located at the apical junctional complex have been implicated in the control of tumor development [295, 312]. Moreover, loss of apical polarity is necessary for cell cycle entry, and is one of the earliest changes observed in tissue architecture in breast neoplasia [293, 295, 313]. Interestingly, smoking, the key factor in the development of lung cancer, has been shown to alter apical polarity in the lung epithelium [314]. Therefore the status of tissue polarity constitutes a critical readout to assess epithelial integrity and homeostasis.

Currently, immunofluorescence imaging of fixed cell culture for apical polarity markers is needed to determine the status of apical polarity. This method prevents dynamic screening of factors that could control epithelial homeostasis. Also the percentage of apically polarized mammary acini in 3D culture varies from 60% to 80%

[293, 313, 315]. Consequently loss of apical polarity in a small, yet significant fraction of the acini population might be easily blurred by variation between different cultures. Thus, a large number of acini have to be analyzed to achieve statistical significance, which implies ineffectiveness of the current immunostaining method.

In polarized epithelial cells, not only proteins but also lipids are differentially distributed on apical and BaM [303, 304]. The ApM is strongly enriched in sphingolipids, which, together with cholesterol, form continuous liquid-ordered assemblies with restricted mobility. In contrast, the BaM has less raft coverage and thus, is in a less ordered phase [303, 304]. Different degrees of lipid ordering have been shown to produce distinct Raman spectral profiles in live tissues [316-318], which opens the possibility for applying this method to 3D cultures of mammary acini.

As a non-invasive and label-free analytical method, Raman spectroscopy has been widely used in biomedical research [319]. In particular, the analysis of lipid composition by Raman spectroscopy is well established in the skin [318], eye lens [317], and nerve fibers [320]. Since the first measurement of living cells [321], Raman spectroscopy has been extensively applied to quantitative studies of biological systems [322-324]. However, the application of Raman scattering to high-speed biological imaging is hindered by the very weak spontaneous Raman signals. In order to enhance the signal level, CARS microscope has been developed [325]. By focusing the excitation energy on the single Raman band and coherent addition of the scattering field, single-frequency CARS microscopy has been employed to visualize lipid-rich structures, including cellular membranes, myelin sheath, and adipocytes, at the speed of a few microseconds per pixel, on a laser-scanning microscope platform [326-328]. To offer spectral information, multiplex CARS (M-CARS) microscopy using a narrowband and a broadband pulse has been developed [329, 330] and applied to the study of LDs in 3T3-L1 cells at a speed of 20 ms per pixel [331, 332]. Another important development is hyperspectral CARS enabled by automatic wavelength scanning of a picosecond laser [333].

To fully appreciate the potential of high-speed vibrational imaging by CARS and quantitative spectral analysis by spontaneous Raman, Cheng and coworkers developed a compound Raman microscope that couples fast CARS imaging of a live biological sample with confocal Raman spectral analysis at points of interest [334]. The compound Raman microscope has been applied to quantitative analysis of LDs in live cells, tissues, and model organisms [334, 335].

In this work, we present a new application of compound Raman microscopy to label-free analysis of live cell membrane in 3D culture. Specifically we investigate how lipid ordering of ApM and BaM could be used to characterize apical polarity in live mammary acini. We took advantage of a high-throughput cell culture technique that permits the formation of acini in the presence of diluted EHS on a glass surface [313], enabling direct microscopic evaluation of apical polarity. We note that cell morphology and organization in 3D culture are completely different from those in flat monolayer culture. The cells in the acini tightly adhere together to form ball-like ApM and BaM, with diameter of 5 and 30 µm, respectively. This feature allowed acquisition of confocal Raman spectra of ApM and BaM with lateral resolution around 0.4 µm and axial resolution around 4 µm**.** By fast CARS imaging followed by confocal Raman spectroscopy of membranes at the equatorial plane of live acini, we show that the relative degree of lipid ordering of ApM compared with BaM effectively distinguishes polarized

(*P*) and nonpolarized (Non-*P*) mammary epithelia with high sensitivity and specificity. This method offers new opportunities for the study of environmental factors that influence epithelial homeostasis.

3.2 Experimental Section

3.2.1 3D Culture of Human Mammary Acini

Non-neoplastic human mammary epithelial HMT-3522 S1 cells were cultured at 37ºC in 5% CO_2, in chemically defined H14 medium. H14 medium consists of DMEM/F12 (Gibco/BRL, St Louis, MO) with 250 ng/ml insulin (Boehringer Mannheim, Indianapolis, IN), 10 µg/ml transferrin (Sigma, St Louis, MO), 2.6 ng/ml sodium selenite (BD Biosciences, Bedford, MA), 10^{-10} M estradiol (Sigma), 1.4 µM hydrocortisone (BD Biosciences), 5 µg/ml luteotropic hormone (Sigma), and 10 ng/ml EGF (EGF; BD Biosciences). H14 medium was routinely changed every 2-3 days. The high-throughput 3D culture was previously described (*Ref.* 32). Briefly cells were plated at a density of 41,520 cells / cm^2 in half the volume of medium for each 35 mm glass bottom dish. The other half of the medium containing 10% EHS material from Matrigel™ (BD Bioscience) was dripped on top of cells 5 min after cell seeding. The culture medium was changed every two to three days with EGF omitted after day 7. Acinar morphogenesis is routinely observed by day 8 to 10.

Treatment with disruptors of apical polarity was applied upon acini formation. Incubation with 1.5 mM EGTA began from day 10 and lasted for 24 hours, a time frame shown to effectively disrupt apical polarity in the majority of mammary acini [293]. Treatment with 60 µM AA (Cayman Chemical) was performed from day 8 to day 12 of

3D culture. The same H14 medium was used throughout the treatments with different modulators of apical polarity. As shown in Figure 3.2, we were able to track the same mammary acini, in gridded glass-bottom culture dishes, undergoing treatment by transmission and CARS imaging.

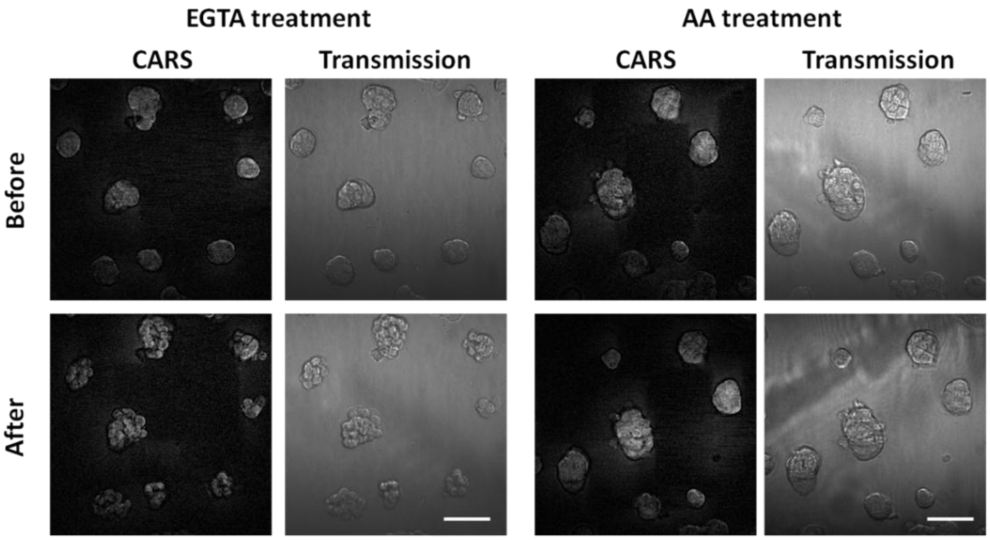

Figure 3.2 Longitudinal tracking of acini undergoing treatments to disrupt apical polarity. Acini were grown on gridded glass bottom culture dishes for 10 days using the high throughput method. They were located by CARS and transmission microscopy imaging before and after treatment with either EGTA or AA. Scale bars, 50 µm.

3.2.2 Immunostaining

Immunofluorescence staining of cells in 3D culture was performed as previously described [315]. Cells were permeabilized with 0.5% Triton X-100 (Sigma) for 15 min in cytoskeleton buffer [100 mM NaCl, 300 mM Sucrose, 10 mM Pipes pH 6.8, 5 mM $MgCl_2$, 1 mM pefabloc, 10 µg/ml aprotinin, 250µM NaF], then fixed in 10% formalin (Sigma) for 20 minutes at room temperature. Antibodies against ZO-1 (Invitrogen catalog # 339100; 5 µg/ml final concentration), ZO-2 (Invitrogen # 37-4700, 10 µg/ml final concentration), and hScrib (Santa Cruz catalog # SC-55543, 5 µg/ml final concentration) were used. Alexa Fluor 488 phalloidin (Molecular Probes, 5 units/ml final concentration) was used to image polymerized actin. Nuclei were stained with 4', 6-diamino-2-phenylindole (DAPI; 0.5µg/ml) and samples were mounted in ProLong antifade solution (Molecular Probes) and stored at -20ºC until use.

3.2.3 Compound Raman Microscopy and Spectrum Analysis

A compound Raman microscope, which integrates CARS and confocal Raman microspectroscopy on the same platform, was used for label-free analysis of apical polarity. In our apparatus, two synchronized 5-ps, 80 MHz laser oscilators (Tsunami, Spectra-Physics Lasers) are temporally synchronized and collinearly combined into a laser-scanning inverted microscope (FV300+IX71, Olympus). Pump and Stokes lasers were tuned to 707 nm (14140 cm^{-1}) and 885 nm (11300 cm^{-1}), respectively, to be in resonance with the CH_2 symmetric stretch vibration at 2840 cm^{-1}. Combined beams were focused into the specimen through a 60x water immersion objective with a 1.2 numerical aperture (UPlanApo/IR, Olympus). The forward CARS signal was collected by an air condenser with a 0.55 numerical aperture, transmitted through a 600/65 nm bandpass filter, and detected by a PMT (H7422-40, Hamamatsu). Average acquisition time for a 512 x 512 pixels CARS image was 1.12 second, and the combined Stokes and pump laser power at the specimen was kept constant at 40 mW. Following CARS imaging, the Stokes beam was blocked and the pump laser induced Raman scattering signal was directed toward the spectrometer (Shamrock SR-303i-A, Andor Technology), which was mounted to the side port of the microscope, to permit spectral analysis from 900 cm^{-1} to

3100 cm^{-1}. The spectrometer pinhole was 50-μm in diameter, which provides an axial resolution of about 4 μm. The lateral resolution was about 0.4 μm. Each Raman spectrum was acquired in 10 seconds, and pump laser power at the specimen was maintained at 15 mW. No tissue damage was observed.

To determine the location of the ApM and BaM, we first adjusted the focus to the equatorial plane of an acinus based on the CARS image (see Figure 3.3A). We then zoomed into the apical site of the acinus by CARS (see Figure 3.3B) and positioned the laser focus for Raman measurement on the most apical pole of certain epithelial cells in the acinus (e.g. the location indicated by the magenta circle in Figure 3.3B). We then moved the focus to the basal site of the acinus (see Figure 3.3C) and positioned the focus for Raman measurement on any location on the BaM of certain epithelial cells of the acinus (e.g. the location indicated by the blue circle in Figure 3.3C).

For Raman analysis, two spectra were taken, one from the cell (membrane, cytoplasm, or nucleus) and the other from the glass. The glass contribution was removed by first scaling the glass profile to make its intensity of the peak-free region (2000-2600 cm^{-1}) the same as that of the cell profile, and then subtracting this modified glass profile from the cell profile. The fluorescence background in the resultant Raman spectrum was fitted by a 4th order polynomial function and further removed. The 4th order polynomial fit was achieved by choosing six points in the spectrum lacking any spectral features. For a better comparison of spectral patterns, each Raman spectrum was then normalized by dividing by the peak intensity of the band around 2935 cm^{-1} over the spectral range 2770 - 3070 cm^{-1}. Then, the normalized Raman spectra were least-squares fitted as a sum of seven Lorentzian bands [330].

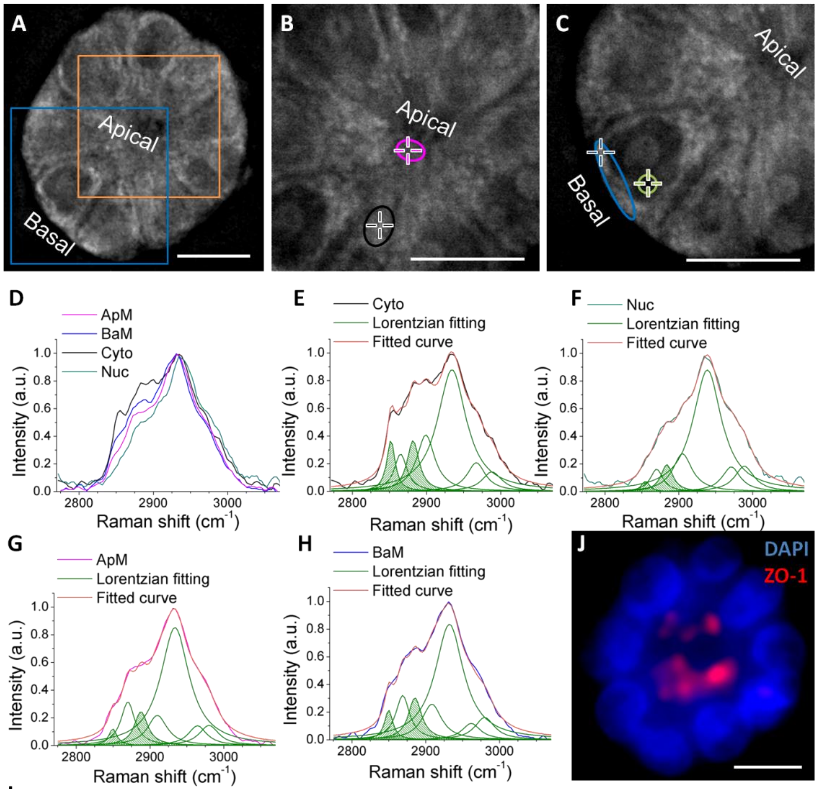

I

	ApM		BaM
R = A_{2885}/A_{2850}	3.32	>	2.31

Figure 3.3 Label-free analysis of lipids in polarized mammary acini. (A) CARS image of a mammary acinus with apical and basal poles. (B) CARS image of the orange square in A shown at higher magnification. Crosses within purple and black circles, which indicate ApM and cytoplasmic regions of the cell respectively, are the positions for confocal Raman spectral measurement. (C) CARS image of the blue square in A shown at higher magnification. Crosses within blue and green circles, which indicate BaM and nucleus regions of the cell respectively, are the positions for confocal Raman spectral measurement. (D) Normalized Raman spectra of regions within ApM (purple line), BaM (blue line), cytoplasm (Cyto, black line), and nucleus (Nuc, green line). (E-H) Lorentzian curve fitting for Raman spectra of ApM, BaM, Cyto, and Nuc. Original spectra are shown in the same color as in D. The Lorentzian fitting curves are shown in green. The areas under Raman bands around 2850 cm^{-1} and 2885 cm^{-1} are highlighted with green stripes. The cumulative fitted curves are shown in orange. (I) Ratio A_{2885}/A_{2850} (R) for ApM and BaM (R for Cyto equals 1.56, and R for Nuc equals 4.11). (J) Fluorescence image of the mammary acinus in A labeled for apical polarity marker ZO-1(red) and DNA (DAPI, blue; nine nuclei are seen in this focal plane). Scale bars, 10 µm.

$$I_{Raman}(w) = \sum_{j=1}^{7} \frac{2A_j}{\pi} \frac{\Gamma_j}{4(w - \Omega_j)^2 + \Gamma_j^{\,2}}$$

where w is the wavenumber, A_j is the area under the j^{th} band, Γ_j is the width and Ω_j is the center wavenumber of the j^{th} band. Peak wavenumbers and widths for curve fitting are listed in Table 3.1. The corresponding assignments of Raman peaks are listed in Table 3.2 [320, 336].

Table 3.1 Curve fitting parameters. The parameters of the seven Lorentzian bands used to fit the 2770 – 3070 cm^{-1} regions of all Raman spectra.

Peak center (Ω_j, cm^{-1})	Peak width (Γ_j, cm^{-1})
2845-2855	13.5
2856.5-2870	23.0
2875-2888	22.0
2885-2910	32.0
2930-2945	47.0
2958-2972	30.0
2980-3000	32.0

For Raman analysis of membrane lipid ordering, CARS microscopy was first used to visualize cell membranes of live mammary acini. Details about how to determine the location of the ApM and BaM can be found in the Supplemental Materials and Methods. The intense bands around 2850 cm^{-1} and 2885 cm^{-1} have been assigned to symmetric and asymmetric CH_2 stretching, respectively. The band around 2885 cm^{-1} is markedly enhanced by Fermi resonance in ordered lipid packing, whereas the band around 2850 cm^{-1} is not affected by structural changes of the lipid hydrocarbon chains [317, 318, 336]. Thus, the degree of lipid ordering can be represented by the ratio between the areas under Raman bands at 2885 cm^{-1} (A_{2885}) and 2850 cm^{-1} (A_{2850}), A_{2885}/A_{2850} (R) [317, 318, 336].

ApM_R (or BaM_R) was the degree of lipid ordering of ApM (or of BaM). A ratio ApM_R/BaM_R was defined to represent the relative degree of lipid ordering of ApM compared with that of BaM. To illustrate the ability of the ratio ApM_R/BaM_R to

Table 3.2 Assignments of Raman peaks.

Raman shift (cm^{-1})	Assignments	
	Protein	Lipid
2850		symmetric CH_2 stretching vibration
2860		Fermi resonance between the asymmetric CH_2 stretching mode
2882		asymmetric CH_2 stretching vibration
2902	symmetric CH_2 stretching vibrations	Fermi resonance between the asymmetric CH_2 stretching mode
2936	asymmetric CH_3 stretching vibration	symmetric CH_3 stretching vibration
2967		asymmetric CH_3 stretching vibration
2986	asymmetric CH_3 stretching vibrations	asymmetric CH_3 stretching vibration

differentiate between *P* and Non-*P* mammary acini, a ROC curve was generated by plotting sensitivity *vs*. (1-specificity) and the AUC was calculated. Based on the ROC curve, the best cutoff of ApM_R/BaM_R was determined.

3.2.4 Statistical Analysis

Student’s *t* test was used to (1) compare the degree of lipid ordering (R) of ApM and that of BaM for *P* and Non-*P* mammary acini, respectively, (2) compare the ratio ApM_R/BaM_R of *P* mammary acini and that of Non-*P* mammary acini, and (3) compare the ApM_R (or BaM_R) of *P* mammary acini and that of Non-*P* mammary acini.

$p < 0.05$ was considered statistically significant. The exact p values are shown in the corresponding figure captions.

3.3 Results and Discussion

As CARS permits selective imaging of lipid-rich structures, it was used to visualize the ApM and BaM in the equatorial plane of live mammary acini. Substantial CARS signals arose from the lipid-rich ApM and BaM of the mammary acinus, whereas weak CARS signals came from the lipid-poor cell nucleus (Figure 3.3A-C). This strong contrast easily distinguished, in a label-free manner, the different compartments of individual cells that form the single-layered epithelium. Considerable CARS signals also arose from the cytoplasmic space, possibly due to lipid-rich organelles such as endothelium reticulum, LDs and mitochondria. An important characteristic of the morphogenesis of acinar structures is the narrower width of the apical pole compared to the basal pole [313]. This characteristic was clearly outlined by CARS (Figure 3.3C). Confocal Raman microspectroscopy was further used to analyze lipid phases of ApM and BaM.

As shown in Figure 3.4, both ApM and BaM are present within the axial resolution of confocal Raman microspectroscopy (~4μm). Although the fingerprint regions on Raman spectra of ApM and BaM (Figure 3.5) did not show clear difference due to the low signal to noise ratio, the C-H stretching regions were very distinct (Figure 3.3D), indicating unique compositions of these cellular compartments. Moreover, based on the Lorentzian curve fitting, the degrees of lipid ordering represented by the ratio

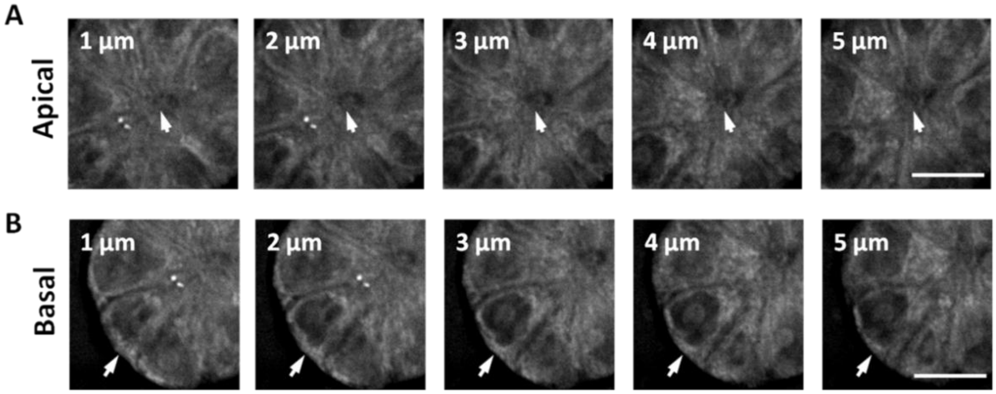

Figure 3.4 Depth-resolved CARS images of the apical and basal poles of a mammary acinus. Arrowheads indicate the ApM in A and BaM in B. Scale bars, 10 µm.

between the areas under Raman bands at 2885 cm^{-1} (A_{2885}) and at 2850 cm^{-1} (A_{2850}), A_{2885}/A_{2850} (R), were different among ApM, BaM, cytoplasm and nucleus (Figure 3.3E-H). In particular, R was much higher in ApM relative to BaM in the majority of *P* acini (n = 40) (Figure 3.3I). The polarized status was confirmed by the apical location of ZO-1 (Figure 3.3J). These results indicate that in the 3D acini, we are able to obtain distinctive Raman spectra from ApM and BaM, which are visualized by CARS. Moreover, the degree of lipid ordering, quantified by the ratio A_{2885}/A_{2850} (R), is different between ApM and BaM.

In order to induce a significant loss of apical polarity in the acini population, 10-day 3D cultures were incubated with 1.5 mM EGTA as shown previously [293]. Note that EGTA does not affect membrane lipid ordering (R) in mammary epithelial cells (S1 cells in 3D culture on day 1) before apical polarity has been formed (Figure 3.6). Raman spectra were then recorded for the nonpolarized (Non-*P*) mammary acini (i.e., with nonapically concentrated ZO-1 staining) from EGTA-treated cultures (usually more than

90% of acini are not apically polarized after EGTA treatment) and from control cultures (usually ~25% of acini are not apically polarized in routine 3D culture) (Figure 3.7). Breast epithelial cells treated with EGTA became round due to the loosening of cell-cell

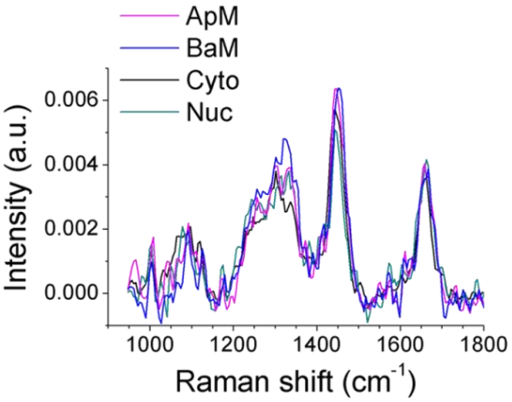

Figure 3.5 Raman spectra (900 – 1800 cm^{-1}) of ApM, BaM, cytoplasm, and nucleus of the acinus shown in Figure 3.3A.

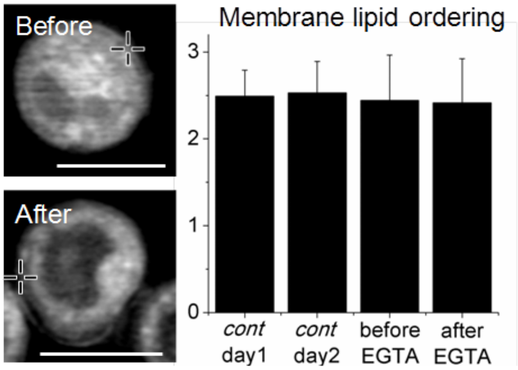

Figure 3.6 CARS images and membrane lipid ordering (R) of S1 cells in 3D culture before apical polarity has formed. EGTA was added on day 1 of 3D culture. Analysis was performed before and after 24h EGTA treatment. Control dishes were analyzed at the same time points. n = 5 cells. No statistical difference was found among the four compared groups (one-way ANOVA). Crosses indicate the locations for Raman spectral analysis. Scale bars, 10 µm.

contacts, which leads to acini with bumpy outer contour (Figure 3.7B). This morphology was in contrast with the control population in which acini usually had a smooth circumference regardless of their polarity status (compare Figure 3.3A to Figure 3.7A). Yet, lipid ordering (R) was consistently lower in ApM compared to BaM in Non-*P* mammary acini regardless of the change in cell shape, indicating that disruption of apical polarity per see is sufficient to show the reorganization of lipids (Figure 3.7).

To confirm that lipid ordering (R) was statistically different between ApM and BaM in both *P* and Non-*P* mammary acini, it was analyzed in 40 *P* and 40 Non-*P* mammary acini. Indeed lipid ordering was significantly higher in ApM compared to BaM for *P* mammary acini; whereas it was significantly lower in ApM compared to BaM for Non-*P* mammary acini (Figure 3.8A). The result for *P* mammary acini is consistent with chromatography analysis of the lipid composition of polarized intestinal cells that shows more ordered lipids within ApM than within BaM [303, 304, 337]. In addition, lipid ordering (R) was significantly higher for the ApM of *P* mammary acini compared to that of Non-*P* mammary acini, and significantly lower for the BaM of *P* mammary acini compared to that of Non-*P* mammary acini. The alterations in membrane lipid ordering in Non-*P* mammary acini compared to *P* mammary acini might be due to the disruption of tight junction, which leads to improper sorting of membrane lipids including cholesterol and sphingolipids. Although the specific lipid compositions of ApM and BaM remain to be investigated, the lipid ordering shows potential to distinguish *P* and Non-*P* mammary acini (Figure 3.8A). In order to differentiate *P* and Non-*P* mammary acini with both high sensitivity and specificity, the lipid ordering ratio, ApM_R/BaM_R, was analyzed. This

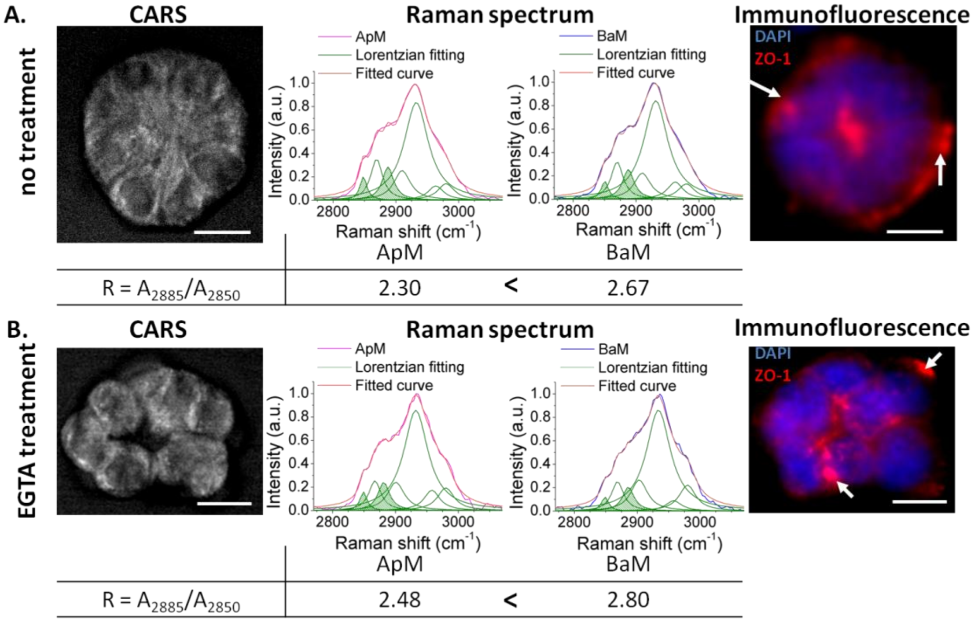

Figure 3.7 Label-free analysis of lipids in nonpolarized mammary acini. Shown are the CARS image, the Raman spectra of ApM and BaM with Lorentzian fitting, the ratio A2885/A2850 (R) for ApM and BaM, and immunofluorescence labeling for ZO-1(red; arrows indicate the presence of ZO-1 at the basal side of the acinus) for a nonpolarized (Non-*P*) mammary acinus in the control group (A) and a Non-*P* mammary acinus in the EGTA-treated group (B). Nuclei are counterstained with DAPI (blue). Scale bars,10 µm.

ratio represents the relative degree of lipid ordering of ApM (ApM_R) compared with that of BaM (BaM_R). Raman scans from different ApM and BaM locations inside an acinus (*P* or Non-*P* acinus) did not produce statistically different lipid ordering ratios (Figure 3.9**)**. Importantly, the lipid ordering ratio was significantly higher for *P* mammary acini compared to Non-*P* mammary acini with much smaller *p* value than that obtained from the comparison of these same populations based solely on ApM_R or on BaM_R (Figure 3.8B). This result suggests that *P* and Non-*P* mammary acini can be distinguished with higher statistical significance when using the lipid ordering ratio compared to the ratio R for the ApM or for the BaM.

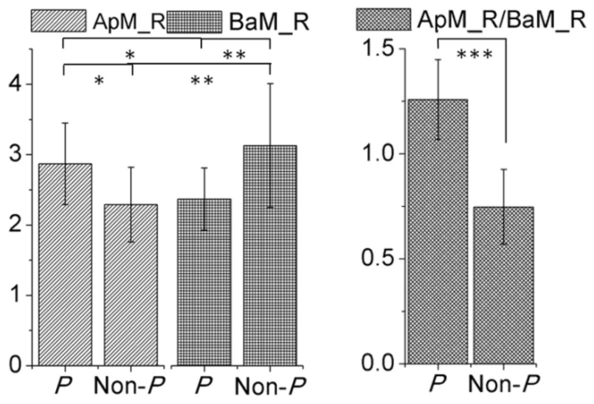

Figure 3.8 Distinction between ApM and BaM in polarized and nonpolarized acini. (A) Comparison of the ratio A2885/A2850 (R) in ApM and BaM regions for both polarized (P) mammary acini and nonpolarized (Non-P) mammary acini. (B) Comparison of the relative lipid ordering ratio ApM_R/BaM_R in *P* mammary acini and Non-*P* mammary acini. (Student's t-test, * $p < 5.0E-5$, ** $p < 1.0E-5$, *** $p = 4.0E-20$, n=40 acini).

The ratio of the symmetric C-H stretching mode intensities (peak height), I_{2885}/I_{2850} (R'), is a well accepted representation of the packing order of acyl chains [317, 318, 320, 338]. However, multiple peaks overlap within the C-H stretching region, which may cause inaccuracy when using peak height to calculate lipid ordering. Therefore in the results presented above we have used Lorentian fitting to obtain peak areas for each Raman bands and we have represented lipid ordering by the ratio of the areas R. The fitting results including parameters, statistics, and residuals can be found in Table 3.3 and Figure 3.10. In order to compare our results with previous work that used R' [318, 338], we also calculated R' for the same 40 *P* and 40 Non-*P* acini used for R calculation in Figure 3.8. R' fell mainly between 1.5 and 2 (for liquid R' equals 0.7, and for crystal it equals 2.2 [318, 338]) and showed the same trends as with R (compare Figure 3.8 to Figure 3.11**)**. However, the *p* values obtained from R' calculations were bigger than those obtained from R calculations, suggesting that R would perform better in distinguishing *P* and Non-*P* acini.

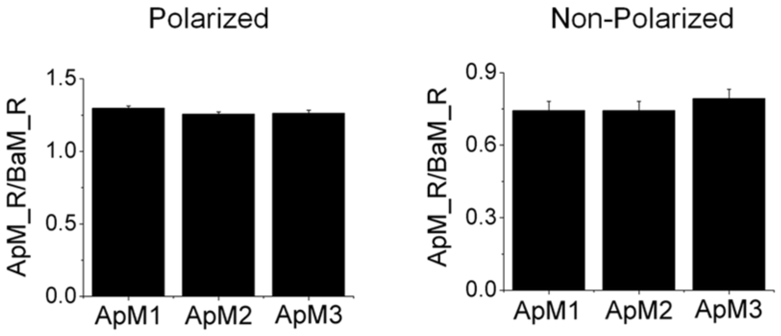

Figure 3.9 Reproducibility of ApM_R/BaM_R measurement. For both P and Non- P acini, ApM_R/BaM_R ratios were obtained based on three Raman scans performed at 3 different locations (labeled as ApM1, ApM2, ApM3) of ApM. No statistical significance was found using ANOVA test.

Table 3.3 An example of fitted curve parameters (peak center, peak width, and area under peak) and statistics (reduced Chi-square and adj. R-square). The statistics reflect the goodness of fit. The numbers in parentheses are the corresponding SDs.

Peak center (Ω_j, cm^{-1})	Peak width (Γ_j, cm^{-1})	Area under peak (a.u.)	Statistics	
2855.0 (1.4)	13.5	3.3 (1.0)	Reduced Chi-Square: 8.6E-4	Adj. R-Square: 0.992
2866.9 (3.0)	23.0	6.5 (1.2)		
2884.4 (1.7)	22.0	10.0 (1.7)		
2900.1 (2.1)	32.0	16.3 (1.9)		
2935.4 (0.9)	47.0	62.0 (1.8)		
2960.0 (2.2)	30.0	9.7 (1.6)		
2986.5 (1.3)	32.0	11.6 (0.9)		

To determine the ability of the lipid ordering ratio, ApM_R/BaM_R, to distinguish *P* from Non-*P* mammary acini, the histogram of the number of acini was plotted as a function of this ratio (Figure 3.12). The plots for *P* and Non-*P* mammary acini were assigned a red and blue color, respectively, and were fitted with normal distribution curves. An overlap between plots indicated that proper cutoff was required in order to distinguish *P* from Non-*P* mammary acini with both high sensitivity and

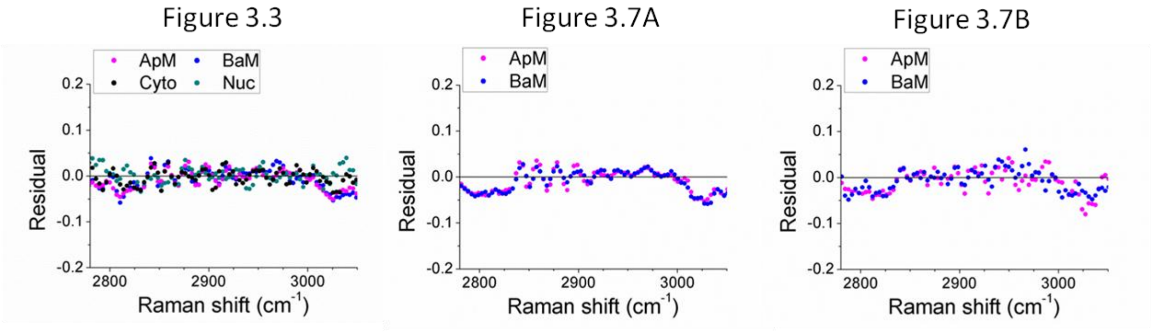

Figure 3.10 Residuals of the Lorentzian fittings for Figure 3.3 and Figure 3.7A-B.

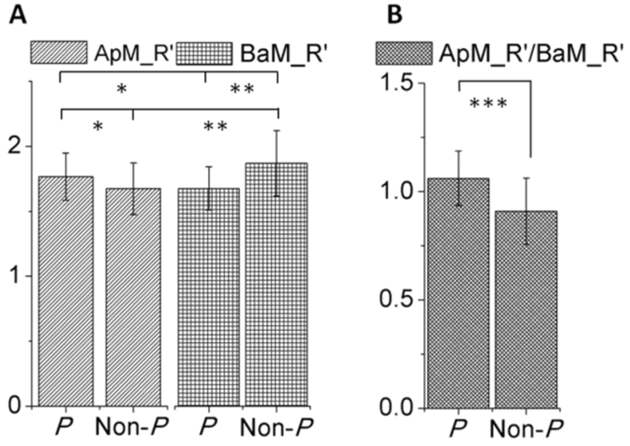

Figure 3.11 Distinction between ApM and BaM in polarized (P) and nonpolarized (Non-P) acini, using the ratios I2885/I2850 (R’) and ApM_R’/BaM_R’. (A) Comparison of the ratio I2885/I2850 (R’) in ApM and BaM for both P mammary acini and Non-*P* mammary acini. (B) Comparison of the ratio ApM_R’/BaM_R’ in *P* mammary acini and Non-*P* mammary acini. (Student's t-test, * $p < 0.05$, ** $p < 5.0E-4$, *** $p = 6.1E-6$, n=40 acini).

specificity**.** A ROC curve was built to illustrate the tradeoff between sensitivity and specificity by plotting the true-positive rate against the false-positive rate for the different possible cutoffs of the lipid ordering ratio. The closer the curve comes to the 45-degree diagonal (shown as a thin black line in Figure 3.12B) the less accurate the diagnostic test. The big AUC (=0.98) clearly demonstrated the ability of the lipid ordering ratio to accurately differentiate *P* from Non-*P* mammary acini (Figure 3.12B**)**. More importantly, the ROC curve provided a way to obtain the desired degree of sensitivity at the cost of specificity. Here, both high sensitivity (=0.925) and specificity (=0.925) were gained with a cutoff of 1.0 (lipid ordering ratio = 1.0). Therefore, it is possible to quantitatively and accurately distinguish *P* from Non-*P* mammary acini by the lipid ordering ratio with both high sensitivity and high specificity.

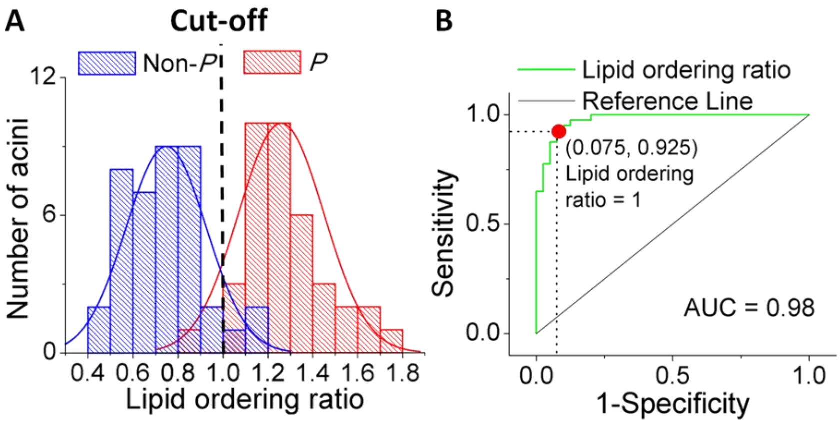

Figure 3.12 Sensitivity and specificity of the relative lipid ordering ratio in identifying polarized and nonpolarized acini. (A) Histogram plot of the number of acini as a function of the lipid ordering ratio (Blue: nonpolarized (Non-P) mammary acini, Red: polarized (*P*) mammary acini). (B) ROC curve illustrating the ability of lipid ordering ratio to distinguish *P* and Non-*P* mammary acini (green line). The ROC curve of two indistinguishable populations, represented by the black line, is included for comparison.

As an application of the label-free approach developed above to measure polarity status, disruption of apical polarity was tracked over time in mammary acini undergoing AA treatment. Dietary fatty acids have been associated with breast cancer development

[42, 339-343]. Particularly, high dietary intake of ω6 PUFAs has been associated with increased breast cancer risk [344]. Moreover, certain dietary interventions with fatty acids were shown to lead to rapid and potentially beneficial changes in ω3/ω6 PUFA ratio in the serum and breast adipose tissue [345, 346]. So far it is unknown whether ω6 PUFA could participate in the initiation stage of breast neoplasia by disrupting apical polarity. The impact of AA on apical polarity was assessed in series of eight live acini before and after treatment with 60 μM AA. CARS images of the same mammary acini were taken before and after a 4-day AA treatment and the status of apical polarity was evaluated based on lipid ordering ratio (Figure 3.13A, 3.14**)**. After excluding the acini that were nonpolarized already before AA treatment, a statistically significant loss of apical polarity (~30% of the population studied) was measured in AA-treated acini (Figure 3.13B). In contrast, examination of the apical location of tight junction protein ZO-1 by immunostaining in the same sets of samples and in 100 acini randomly chosen in each experiment, failed to reveal a statistically significant loss of apical polarity in AA-treated acini population (Figure 3.13C, 3.15).

The results shown in Figure 3.13 demonstrate that although immunostaining of tight junction proteins has been commonly used to determine the status of apical polarity [293, 313, 315], it is not very effective to detect significant loss of apical polarity induced by dietary factors in a small portion of the acini population. This ineffectiveness of immunostaining method is largely due to the variation between different cultures, given that the percentage of *P* mammary acini in control cultures varies from 60% to 80% [293, 313, 315].

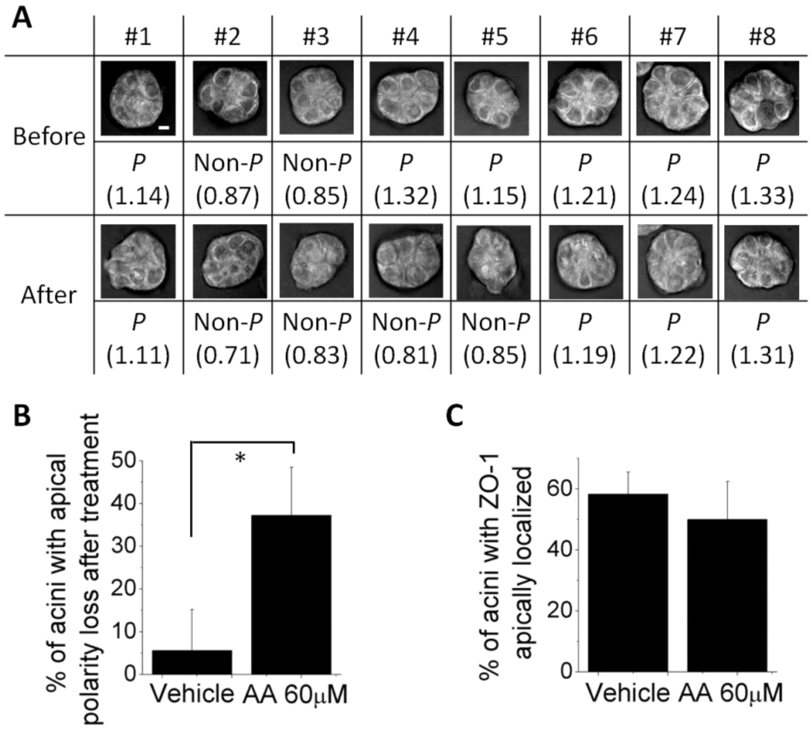

Figure 3.13 Measurements of the polarity status in acini before and after treatment with ω6 fatty acid. Acini were incubated with either ethanol vehicle or 60 µM AA from day 8 to 12 of 3D culture. (A) Status of apical polarity (polarized, *P* or nonpolarized, Non-*P*) based on the lipid ordering ratio (ApM_R/BaM_R, number indicated in parenthesis; R = A_{2885}/A_{2850}) for the same group of acini before and after AA treatment as measured by the Raman scattering-based method. (B) Percentage of acini that have lost apical polarity in the control and AA-treated groups at day 12 (after treatment with vehicle or with AA) compared to day 8 (before treatment) detected by the Raman scattering-based method (**p* value=0.0066, n=3 sets of 8 acini). (C) Percentage of acini with ZO-1 apically localized in vehicle control and AA-treated groups at day 12 of 3D culture (using the sample sets analyzed in B). Scale bar, 5 µm.

By tracking the status of apical polarity for the same live acini before and after treatment with the Raman method, we are able to take into account only the acini that are apically polarized before treatment and then readily measure how many of them lose apical polarity. Thus, our label-free Raman analysis measures a true effect of the treatment on apical polarity by discarding false positives, that is, the acini that would not have been apically polarized from the start.

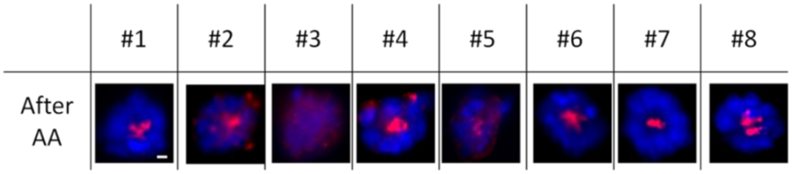

Figure 3.14 Immunofluorescence images of AA-treated mammary acini. Immunostaining for ZO-1 (red) and labeling for DNA (DAPI, blue) in acini following treatment with AA shown in Fig. 5A. Scale bar, 5 µm.

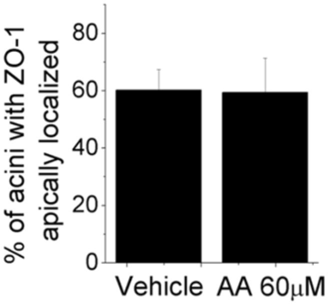

Figure 3.15 Blind scoring of ZO-1 localization in control and AA-treated acini populations. Acini in control and 60 µM AA-treated groups were fixed and immunolabeled for ZO-1 in three independent experiments (the same ones shown in Fig. 5). Here, at least 100 acini were randomly chosen and scored (ZO-1 staining apically localized or not apically localized) per experiment and results were analyzed by Student’s t-test.

To understand the origin of reduced lipid ordering in Non-*P* acini, we further studied how AA treatment might affect the tight junction complex. It is possible that the effect of AA might only encompass ZO-1, leaving the rest of the tight junction intact. To rule out this possibility, the effect of AA was studied not only on ZO-1 but also on ZO-2, another core tight junction protein that links transmembrane proteins to cytoplasmic

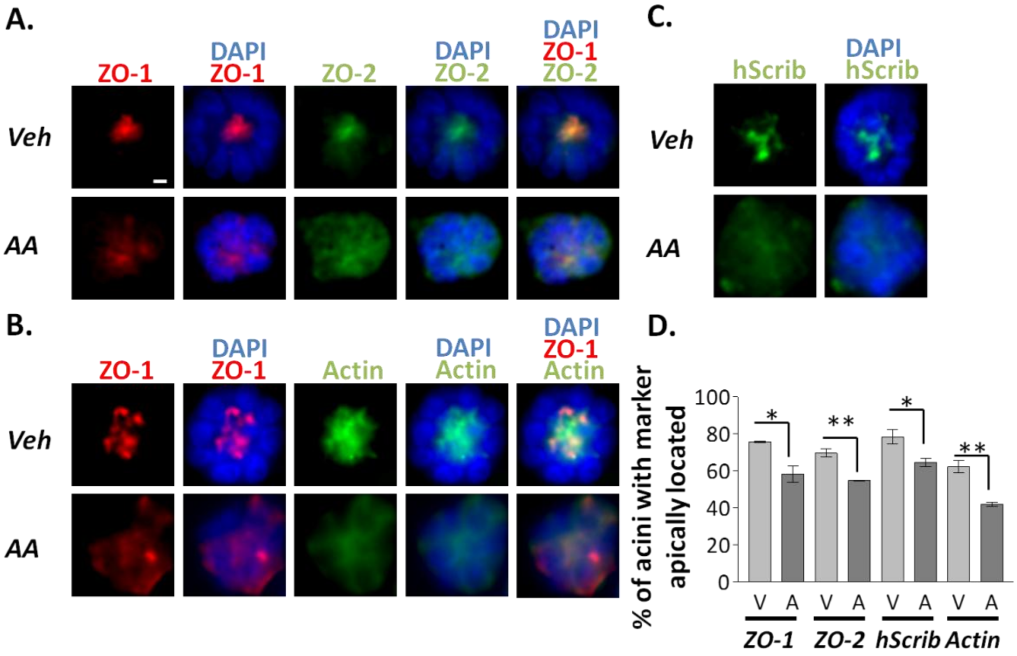

Figure 3.16 Distribution of apical polarity-related proteins in polarized (P) and nonpolarized (Non-P) acini. Dual staining for tight junction core proteins ZO-1 and ZO-2 (A), ZO-1 and cytoskeleton component actin (B), and immunolabeling for apical polarity organizer hScrib (C) in *P* mammary acini in the control group (vehicle, *Veh*) and Non-*P* mammary acini in ω6 *AA*-treated group. Cell nuclei were labeled with DAPI (blue color). (D) Histograms of the percentages of acini with apically located ZO-1 (p = 0.0167), ZO-2 (p = 0.0026), hScrib (p = 0.0347) and actin (p = 0.0043), (n=3, *V*: *Veh*, *A*: *AA*). * $p < 0.05$; ** $p < 0.01$. Scale bar, 5 µm.

components of the junctional complex and the cytoskeleton [347-349]. Immunostaining performed in a new set of experiments revealed that the two tight junction core proteins ZO-1 and ZO-2 colocalized in more than 90% of the cases when apically located and were significantly mislocalized upon AA treatment (Figure 3.16A**)** but did not overlap when away from the apical pole, suggesting that AA affects the tight junction complex globally. ZO-1 is the main protein that stabilizes the tight junction to the actin cytoskeleton in cells [347, 349, 350], therefore a severe disruption of the tight junction complex should be associated with the reorganization of the cytoskeleton. In cells that had apically polarized ZO-1, staining for polymerized actin was strongest at the apical side of the cells (Figure 3.16B). This is expected since the actin cytoskeleton serves as a framework to which tight junction complexes can bind and be secured in place [349]. However, in the cells that had mislocalized ZO-1, the actin cytoskeleton was diffuse (Figure 3.16B), in agreement with a disruption of the tight junction complex. Tumor suppressor hScrib [312] plays a critical role during the initial formation of the tight junction complex [351] and disruption of tight junctions might perturb its function. In control acini, hScrib was located at the apical side with some lateral positioning, as shown by immunostaining. However, in acini treated with ω6 AA, hScrib became mislocalized as revealed by a diffuse staining pattern (Figure 3.16C). Although the immunostaining method cannot always detect a significant difference between control and treated groups (Figure 3.13C, 3.14), there have been some instances in which the AA treatment induces statistically significant loss of apically located ZO-1, ZO-2, hScrib, and actin, as shown in Figure 3.16D. These observations suggest that AA profoundly affects apical polarity, including the integrity of hScrib tumor suppressor localization. Specifically, they indicate that AA causes acinar cells to lose apical organization via a disruption of the tight junction complex, because two of the tight junction core proteins redistribute away from the apical pole and tight junction anchorage to the actin filament network is destabilized. Considering the key role of actin filaments in maintaining the integrity of cell membranes, cytoskeleton disruption is consistent with the reduced lipid ordering in the ApM as detected by the Raman analysis. Therefore the lipid ordering ratio is a powerful way to measure modifications in tissue polarity, and thus, tissue homeostasis in live epithelia.

Our technique can be potentially used, in association with the breast cell model, as a screening method of risk factors for breast cancer as well as a screening method for chemopreventive agents in a similar way as what scientists are starting to do with cancer cells. In the latter case, cancer cells placed in 3D culture form tumor nodules that are then treated with potential anticancer drugs to test the cytotoxicity of these agents. In our study we are working with non-neoplastic cells based on increasing evidence from cell culture and patient studies that loss of apical polarity is a very early sign of a preneoplastic change [293]. There are currently no ways to test for dietary or chemical compounds that could act as agents to initiate and prevent the development of breast tumors. We are proposing that our apical polarity measurement method in 3D cell culture of non-neoplastic cells would permit accurate screening of deleterious factors for breast health (that would induce loss of apical polarity) and also preventive factors (based on the reestablishment of apical polarity by these factors or their effect to prevent apical polarity loss normally induced by other factors). The possibility of live cell detection with Raman technology will permit the study of sequential effects of factors of interest, e.g., to assess whether factor B restores apical polarity previously altered by factor A.

We have demonstrated that a Raman scattering based platform can be used to provide label-free determination of apical polarity of live mammary acini in 3D culture. In this method the lipid configurations within apical and BaM are measured by high-speed CARS imaging integrated with confocal Raman analysis. Notably, the derived ratio of the degree of lipid ordering appears superior to immunofluorescence-based analysis of fixed samples to determine the presence or disruption of apical polarity. This method has enabled us to quantify, with high sensitivity and specificity, the percentage of acini that lose apical polarity due to the effect of AA, a risk factor for breast cancer development. The proposed method provides an unprecedented label-free screening platform for rapid identification of risk factors that initiate the very early stage of epithelial neoplasia. Moreover, the use of the membrane lipid phase as readout to assess polarity should be applicable to other types of epithelia where over 90% of cancers originate. Indeed polarity is a common feature of the homeostasis of such tissues and all studies of early changes in epithelial neoplasms so far report polarity loss.

CHAPTER 4. LABEL-FREE IDENTIFICATION OF MAMMARY ADENOMA AND ADENOCARCINOMA BY COHERENT ANTI-STOKES RAMAN SCATTERING AND SUM FREQUENCY GENERATION IMAGING

A portion of the work presented in this chapter was published in *Laser & Photonics Reviews* [217]. Reprinted with permission from [217]. Copyright © 1999-2013 John Wiley & Sons, Inc.

Intact and unstained mammary tissues were examined by a multimodal NLO imaging system that allows CARS imaging of lipid-rich structures and SFG imaging of type I collagen fibrils. The CARS signals arising from cell membranes and cytoplasmic LDs allowed the identification of tumor cells, adipocytes, and endothelial cells. Simultaneous CARS and SFG imaging enabled direct 3D visualization of cell arrangement and ECM organization, but without the requirement for labeling. Epithelial cells that form a single row on the innermost part of the duct were visualized in normal mammary glands. In mammary adenomas, abundant wavy collagen fibrils formed a smooth outer contour to concentrically wrap the small cluster of tumor cells. In mammary adenocarcinomas, epithelial cells showed a ragged contour without an organized concentric wrap of collagen around them. These results were verified by histological analysis. Quantitative analysis of collagen density indicated that mammary adenocarcinomas had much less collagen density surrounding tumor mass than mammary adenomas. Taken together, these findings suggest that multimodal CARS/SFG imaging could potentially be an intraoperative image-guided tool for assessing tumor margins during breast cancer surgery

4.1 Introduction

Breast cancer is the most common form of cancer in women, except for non-melanoma skin cancer, and it is also the leading overall cause of cancer death in women between the ages of 20 and 59 [1, 352]. Fortunately, approximately 90% of initial breast cancer cases are diagnosed as a localized or locoregional disease, which can be attributed to the increased use of screening mammography [353]. Considering the negative impact of mastectomy on cosmesis and associated psychological issues of breast cancer patients [354], and the equivalent effectiveness of mastectomy and lumpectomy [355, 356], the National Institutes of Health has suggested lumpectomy as a primary treatment option in the majority of women with early-stage breast cancers [357]. Theoretically, non-hematological cancers can be cured if entirely removed by surgery, but this is not always possible because a single cancer cell, invisible to the naked eye, can re-grow into a new tumor. In order to define negative margins that are free of any cancer cells adjacent to the boundary of the tissue resection, pathologists need to examine the surgical specimen to determine if a margin of healthy tissue is present. As a result, about half of the patients undergoing lumpectomy have to suffer repeated surgical procedures called re-excisions [358]. Studies have shown that the risk of local recurrence and distant metastasis after lumpectomy is positively associated with the appearance of positive margins after the first surgery and the numbers of re-excision lumpectomies [359, 360]. Thus, accurately attaining negative margins at the first surgical procedure is the optimal outcome of lumpectomy. To assist in a complete resection of adenocarcinomas with negative margins in a single surgical procedure, we need an efficient intraoperative image-guided tool that can distinguish normal breast tissues from malignant tumor tissues [361-364].

Although histopathology has been the gold standard for cancer diagnosis, it cannot be used as an intraoperative image-guided diagnostic tool because histology requires time-consuming sample preparation, and it cannot provide 3D and real-time information about tissue architecture and organization in the natural state. Recently, medical imaging techniques, such as ultrasound [365], MRI [366] and radiofrequency spectroscopy [367], have been used as image-guide intervention methods in cancer surgery. However, all these imaging techniques only allow visualization of tissue anatomy with the resolution of ~1mm, which is not sufficient for accurate determination of tumor margins during the surgical phase. In addition to those clinical and diagnostic imaging techniques currently in use, optical imaging and spectroscopy are gradually becoming popular in the development of novel tumor diagnostic techniques. For example, OCT allows cross-sectional imaging of breast cancer in surgery with an endoscope [368, 369]. Raman spectroscopy has been employed to diagnose epithelial pre-malignant lesions and cancers based on chemical composition [370]. Confocal reflectance microscopy [371] and elastic scattering spectroscopy [372] have also been used for cancer diagnosis in clinical studies. However, their limited resolution or limited specificity hampers identification of the organization and composition of normal or disease states of mammary glands, which would be vital to the definition of negative boundaries. Therefore, the intraoperative image-guided tool needs to be an imaging technique that enables visualization of cellular and subcellular structures with high resolution.

During the past two decades, NLO imaging has opened a new window for cancer imaging [373]. In addition to submicron spatial resolution, NLO imaging allows 3D imaging of tissue architecture with large penetration depths, which cannot be attained using conventional histological techniques or confocal fluorescence microscopy. Collective studies have shown that differences in morphology and metabolic activity between malignant and non-malignant epithelial cells can be delineated by TPEF imaging of endogenous fluorophores, such as NAD(P)H and FAD [374, 375]. A distinct advantage of this method is that it avoids the need for any exogenous labeling agents, thus eliminating toxicity and safety concerns related to their use. However, based solely on the fluorescence signal from endogenous fluorophores, clear images of tumor cell structures are difficult to produce. In addition, TPEF is often combined with SHG imaging that visualizes type I collagen fibrils within tumor tissues, a major component of ECM [376].

To visualize biological molecules that cannot bear fluorescent labeling, CARS microscopy has been developed for high-speed vibrational imaging of lipid-rich structures, such as cellular membranes, myelin sheath, and cytoplasmic LDs [217]. More recently, multimodality imaging on a CARS microscope has been realized by implementation of SFG and TPEF using the same picoseconds laser sources [217]. The application of CARS microscopy to cancer imaging is emerging. Le *et al*. have demonstrated that CARS microscopy is able to visualize lipid-rich tumor cells *in vitro* and in mammary tissues [221, 377]. Evans *et al*. have applied CARS microscopy to vibrational imaging of brain tumor [378]. Nevertheless, the ability of CARS microscopy to differentiate adenomas from adenocarcinomas has not been demonstrated. Additionally, the advantages of integrating CARS and SFG for cancer detection have not been explored.

In this paper, we investigated whether multimodal CARS/SFG imaging could be used to characterize the features of unstained normal mammary gland, adenomas and adenocarcinomas in a methylnitrosourea (MNU)-treated female Sprague-Dawley rat model. Tumors induced in rats by administration of chemical carcinogens, such as MNU, have the potential to be examined during the multi-step process of carcinogenesis, including initiation, promotion, and progression [379, 380]. Here, we observed substantial CARS signals arising from the lipid-rich cell membranes and cytoplasmic LDs, but weak CARS signals from the lipid-poor cell nuclei. Thus, CARS imaging enabled us to identify various cell types, such as tumor cells, adipocytes, and endothelial cells, based on cell morphology and cytoplasm/nucleus ratio. Moreover, simultaneous CARS and SFG imaging enabled direct 3D visualization of cell arrangement and ECM organization without labeling. These results were verified by corresponding staining and standard histological analysis. Based on the morphology and 3D arrangement of epithelial cells and organization of collagen fibrils, we demonstrated that CARS/SFG imaging was able to accurately identify the normal mammary gland and distinguish between adenomas and adenocarcinomas. These findings suggest that CARS/SFG imaging could become an intraoperative image-guided tool for assessing tumor margins during breast cancer surgery.

4.2 Experimental Section

4.2.1 Animal Model and Tissue Specimens

Outbred female Sprague-Dawley rats were placed on a rat chow diet (Harlan Tech, Indianapolis, IN) containing 3.30 kcal/g of metabolizable energy. Rats received the carcinogen MNU or a control 0.9% saline injection. Tissue specimens for CARS/SFG imaging were flash frozen in liquid nitrogen and stored at -80 °C. Prior to imaging, tissue samples were briefly thawed at room temperature and fixed in 10% neutral-buffered formalin. All animal experiments were done with the approval of the Purdue Animal Care and Use Committee.

4.2.2 Histological Analysis

Mammary glands and tumor tissues were fixed in a solution of 10% neutral-buffered formalin. After fixation, tissues were processed and embedded in paraffin blocks. Tissue sections of 5 µm thickness were prepared and stained with hematoxylin-eosin. Mammary tumors from MNU-injected animals were classified as adenomas and adenocarcinomas based on gross morphology by a board certified pathologist. Normal mammary tissue from saline-injected animals was verified as free of any lesions. Histology images were acquired using a Nikon Eclipse E400 microscope (Nikon Corp., Tokyo, Japan) equipped with air objectives and a Spot Insight camera (Diagnostic Instrument, Inc., Sterling Heights, MI).

4.2.3 CARS/SFG Imaging System

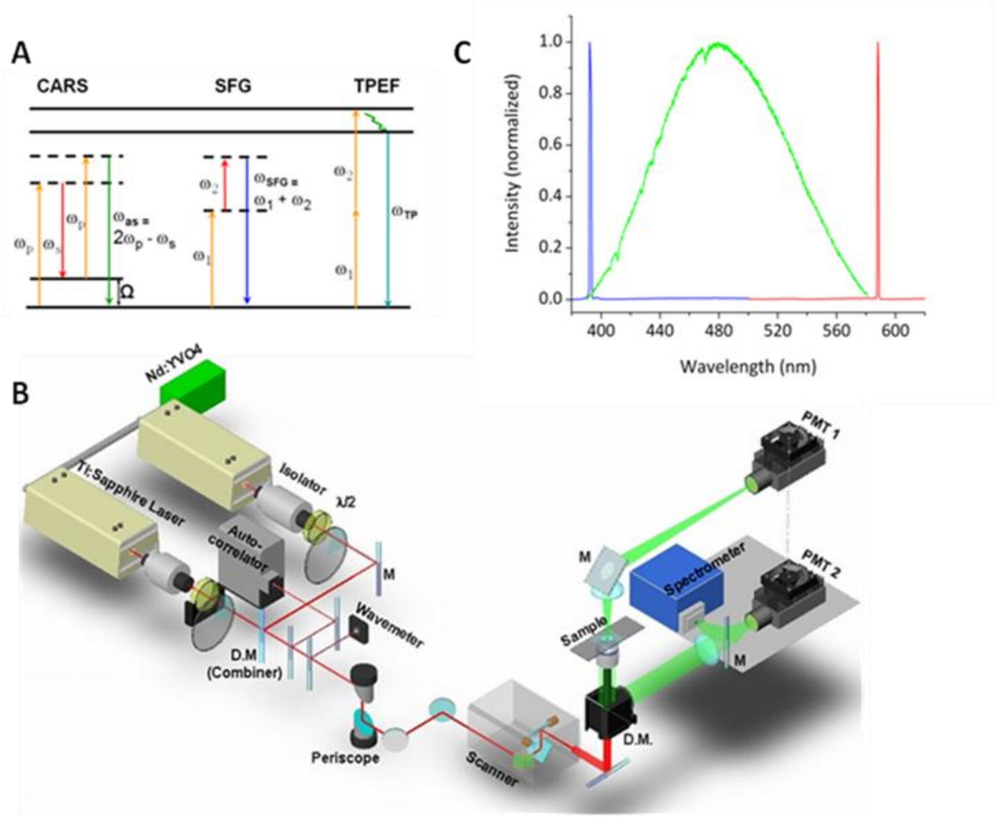

Figure 4.1 Multimodal NLO imaging methods and setup. (A) Energy diagram of NLO processes including CARS, SFG, and TPEF. (B) Schematic of a NLO microscope which combines CARS, SFG, and TPEF on the same platform. Inset window shows the simplified light path. DM: dichroic mirror, M: mirror. (C) Emission spectra of SFG signals from collagen fibrils (blue); TPEF signals from Hoechst 33342-labeled nuclei (green); and CARS signals from LDs (red).

A multimodal NLO microscope which allows CARS, SFG, and TPEF imaging on a single platform (Figure 4.1B) has been previously described [217]. The energy diagrams of CARS, SFG, and TPEF are shown in Figure 4.1A. The details has been described in previous chapters.

Microspectroscopy analysis of mammary tissue components was carried out by using a spectrometer (Sharmrock 303i, Andor Technology, Belfast, Ireland) equipped with an electron multiplying CCD (EM-CCD, Newton-970N-BV, Andor), installed at the back port of the microscope, and externally triggered by the confocal scanner. In this experiment, we first acquired an image, and then focused the light into a pixel of interest by the point-scan mode. The point-scan action triggered the spectrometer to record a spectrum of the NLO signals arising from the focal region (Figure 4.1C).

4.2.4 Imaging Conditions

No sample preparation was necessary before imaging the excised mammary tissues. A glass-bottom chamber containing tissues submerged in 1x PBS was placed on the microscope for imaging at room temperature. For CARS, SFG, and TPEF imaging of fixed tissues, the average powers of the pump and Stokes laser beams were attenuated by using neutral-density filter wheels to 40 mW and 20 mW at the sample when using the 20x objective, and 20 mW and 20 mW at the sample when using the 60x objective. For CARS and SFG imaging of histology slides, the average powers of the pump and Stokes laser beams were attenuated to 10 mW and 5 mW at the sample using the 20x objective. There was no noticeable photodamage to the samples throughout the imaging processes.

To visualize the tumor architectures with 3D cellular and subcellular resolution, we directly placed tissues of different thickness around 5 mm on a glass surface such that a relatively flat tissue surface faces the 60x water immersion objective on an inverted microscope. When the beating frequency was set to the specified 2840 cm^{-1}, substantial CARS signals arising from the lipid-rich structures were observed.

4.2.5 Quantitative Analysis of Collagen Density Surrounding Tumor Mass

An analysis volume was defined with the dimensions of 250 µm (x) × 250 µm (y) × 30 µm (z), with z = 0 being the tumor mass and collagen interface. For each analysis volume, 31 frames along the z-axis with a fixed step size of 1 µm were acquired. Six different volumes were evaluated, and the total SFG intensity from 186 frames (6 × 31 frames) was used to infer the mammary stromal collagen density surrounding tumor mass. The laser power at the sample and the high voltage of the PMT were kept constant for all measurements.

4.3 Results

4.3.1 Significant Components of Mammary Tissues Visualized with Label-free CARS/SFG Imaging

Since CARS is sensitive to lipids, which are a main component of the cytoplasmic LDs, cell membranes, and intracellular membranes, we used CARS to depict morphology of various cell types in mammary tissues. We observed substantial CARS signals arising from the cell membranes and cytoplasmic LDs, but only weak CARS signals from the lipid-poor cell nuclei (Figure 4.2A), a contrast indicating significantly enhanced visualization of cell morphology. Thus, CARS images enabled the identification of various cell types based on cell morphology and nucleus-cytoplasm ratio. For instance, mammary tumor cells were identified by a round shape and a large nucleus-cytoplasm ratio. The tumor cell nucleus and membrane were confirmed by Hoechst 33342 (Figure 4.3A-C) and DIOC18 (Figure 4.3D-E) staining, respectively. Adipocytes were identified by giant LDs within cells (Figure 4.2B), and blood vessels were recognized by tubular

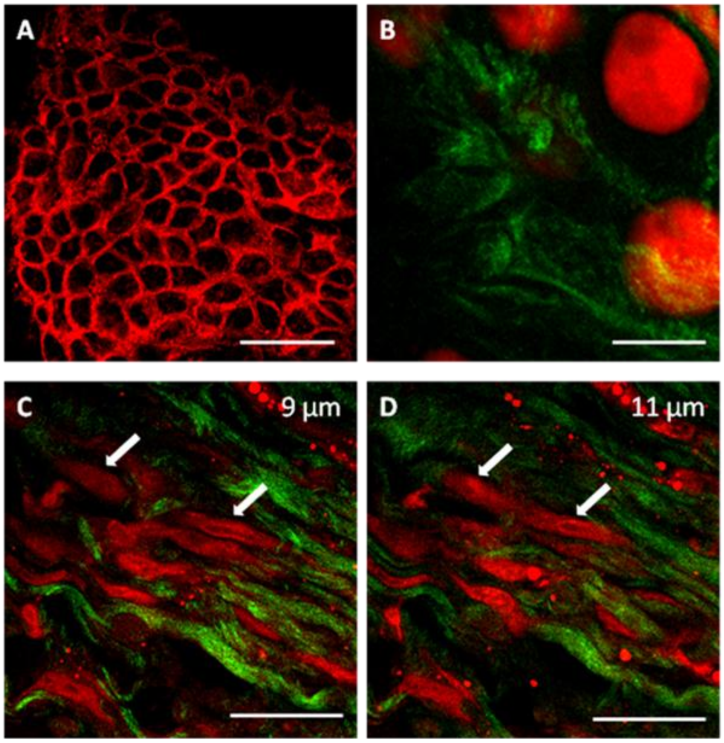

Figure 4.2 CARS and SFG imaging of significant components of the mammary tumor and stroma (Red: CARS; Green: SFG). (A) CARS image of tumor cells whose signal comes from lipid-rich cell membrane. (B) Adipocytes among dense collagen fibrils. (C-D) 3D images of blood vessels surrounded by parallel collagen fibrils. Scale bars: 25 µm.

structures shown in depth-resolved CARS images (Figure 4.2C-D), which were confirmed by FITC-IB4 labeling (Figure 4.4). In addition to various types of cells, we observed dense type I collagen fibrils surrounded by adipocytes (Figure 4.2B) and paralleled with blood vessels (Figure 4.2C-D). These findings demonstrate that CARS/SFG imaging allows label-free evaluation of mammary tissue architecture, including cell shape and arrangement, as well as collagen organization.

4.3.2 CARS/SFG Imaging of Normal Tissue, Adenoma, and Adenocarcinoma of Mammary Glands in Histology Samples

To determine whether CARS/SFG imaging could identify normal mammary gland, adenomas, and adenocarcinomas, we studied well-defined histology slides of mammary tissues. While considerable forward CARS signals arose from the unfilled areas on histology slides, including LDs within adipocytes, cell nuclei gave significant negative contrast because Haematoxylin, which was used for cell nuclei staining, absorbed most of the incident light. For the same reason, eosin-stained cytoplasm and ECM can be seen under CARS microscopy. Thus, CARS enabled us to depict the morphology of the histological specimen. SFG was used for selective imaging of type I collagen fibrils.

Compared with histological images of normal mammary gland, adenomas and adenocarcinomas (Figure 4.5A-C, respectively), the merged CARS and SFG images of corresponding histology slides (Figure 4.5D-F, respectively) specifically depicted morphological characteristics of normal mammary gland, mammary adenomas and adenocarcinomas. Density and organization of collagen fibrils surrounding epithelial cells provided the first identification marker. In the normal mammary glands and mammary adenomas, dense wavy collagen fibrils paralleling the ductal profile formed an integral scaffold to support the ductal cells. In contrast, the tumor mass in mammary adenocarcinomas was surrounded by thin and disorganized collagen fibrils. In addition, the extent of cell proliferation could be used as the second identification marker. The ductal epithelium formed a single layer in normal mammary gland, but proliferated as

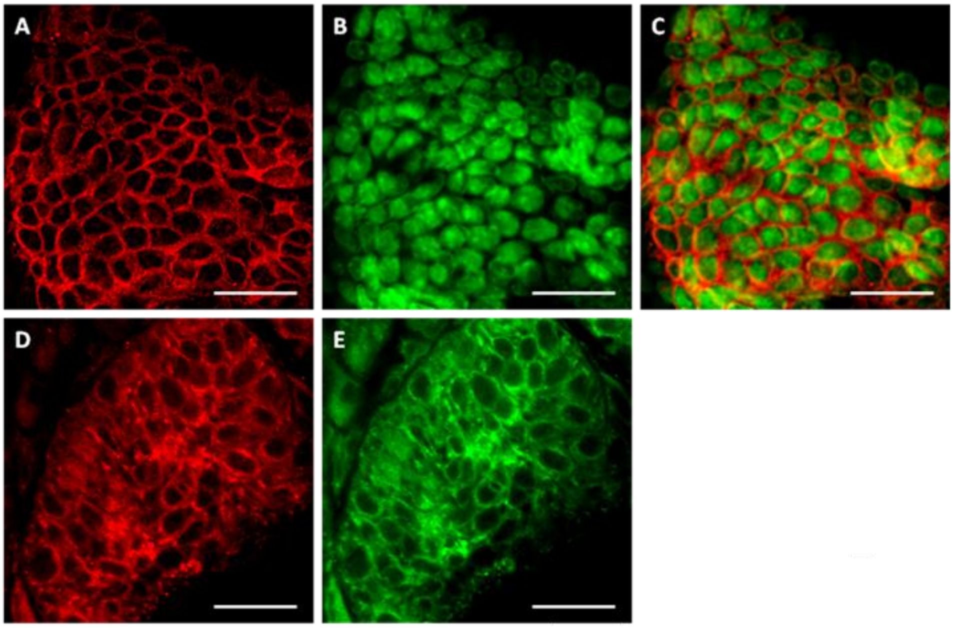

Figure 4.3 Confirm CARS observation of tumor cells by Hoechst33342 and DIOC18 labeling. (A, D) CARS image of tumor cells whose signal comes from lipid-rich cell membranes. (B) TPEF image of tumor cell nuclei labeled with Hoechst33342. (C) Merged image of A and B (red: CARS; green: TPEF). (E) TPEF image of tumor cell membrane labeled with DIOC18. Scalar bars: 25 µm.

multilayered epithelium in mammary tumors. Moreover, whereas the tumor mass was still localized in adenomas, tumor cells proliferated out of control and invaded the surrounding stroma in adenocarcinomas.

4.3.3 CARS/SFG Imaging of Intact Normal tissue, Adenoma, and Adenocarcinoma of Mammary Glands

The criteria established in the CARS/SFG images of histology slides were used to study unstained mammary tissues. The label-free CARS and SFG images of the intact normal mammary gland are shown in Figure 4.6A, which reflects the similar features

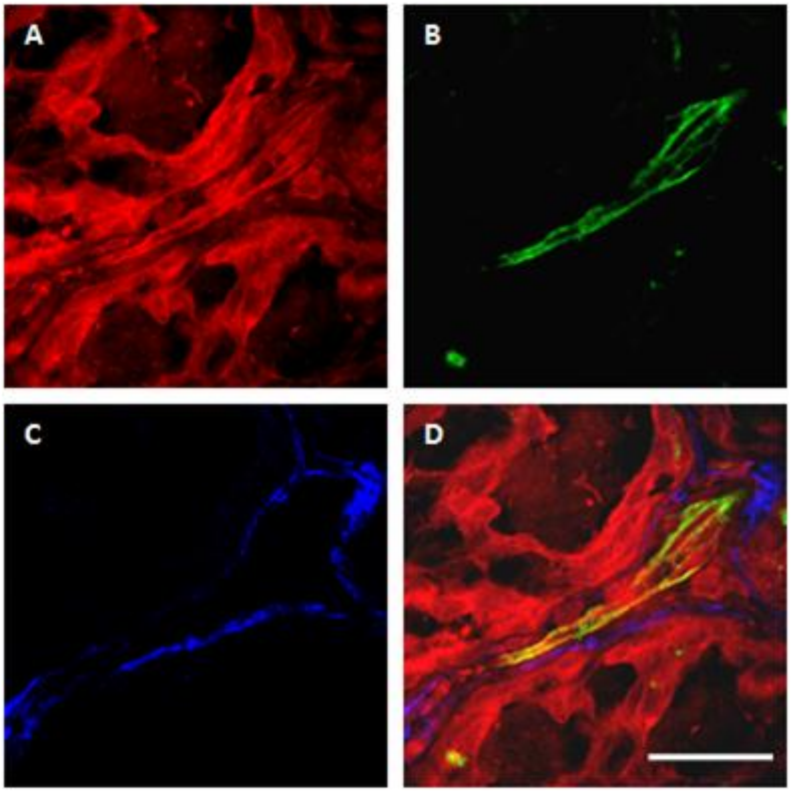

Figure 4.4 Confirm CARS observation of blood vessels by FITC-IB4 labeling. (A) CARS image of tumor cells and endothelial cells. (B) TPEF image of a blood vessel labeled with FITC-IB4. (C) SFG image of collagen fibrils. (D) CARS image (red) of the blood vessel is colocalized with TPEF (green) image. The blood vessel is protected by collagen fibrils (blue). Scalar bars: 25 μm.

observed from standard light microscopy of histological slides (Figure 4.6B). Based on these images, we were able to observe a single layer of epithelia on the innermost part of the duct. Bunches of mature collagen with a wavy fibrillar appearance tend to wrap concentrically around the duct and show a typical orientation of their long axis paralleling the duct. Outside the collagen are orderly arranged adipocytes with one giant LD per cell. In the zoom-in CARS image of the ductal cells, the single layer of columnar epithelium was seen with single-cell resolution (Figure 4.6C).

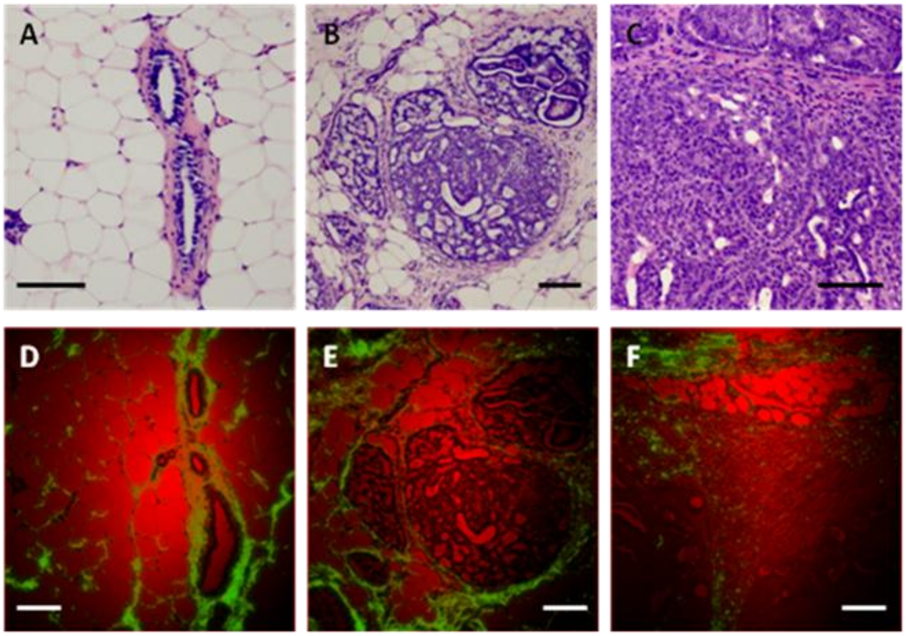

Figure 4.5 Validating CARS/SFG imaging as a tool to identify the normal mammary gland, mammary adenomas and adenocarcinomas. (A-C) H&E stained histology images of normal mammary gland, mammary adenoma and adenocarcinoma, respectively. Scale bars: 100 µm. (D-F) CARS and SFG images of histology slides from normal mammary gland, mammary adenoma and adenocarcinoma, respectively. Scale bars: 75 µm.

We further characterized mammary tumor tissues with the CARS/SFG imaging system. 3D images of adenomas showed that abundant wavy collagen fibrils formed a smooth outer contour that concentrically wrapped around the small cluster of tumor cells. These cells had a low cuboidal shape with enlarged nuclei and were in close proximity to each other (Figure 4.6D-F). The well-defined collagen boundary around the localized tumor mass was indicative of the tumor's benign nature. On the contrary, tumor cells in the adenocarcinoma showed a ragged contour without an organized concentric wrap of collagen (Figure 4.6G-I). These malignant tumor cells had a similar shape and size as tumor cells in the adenoma, but they had more invasive potential with the assistance of

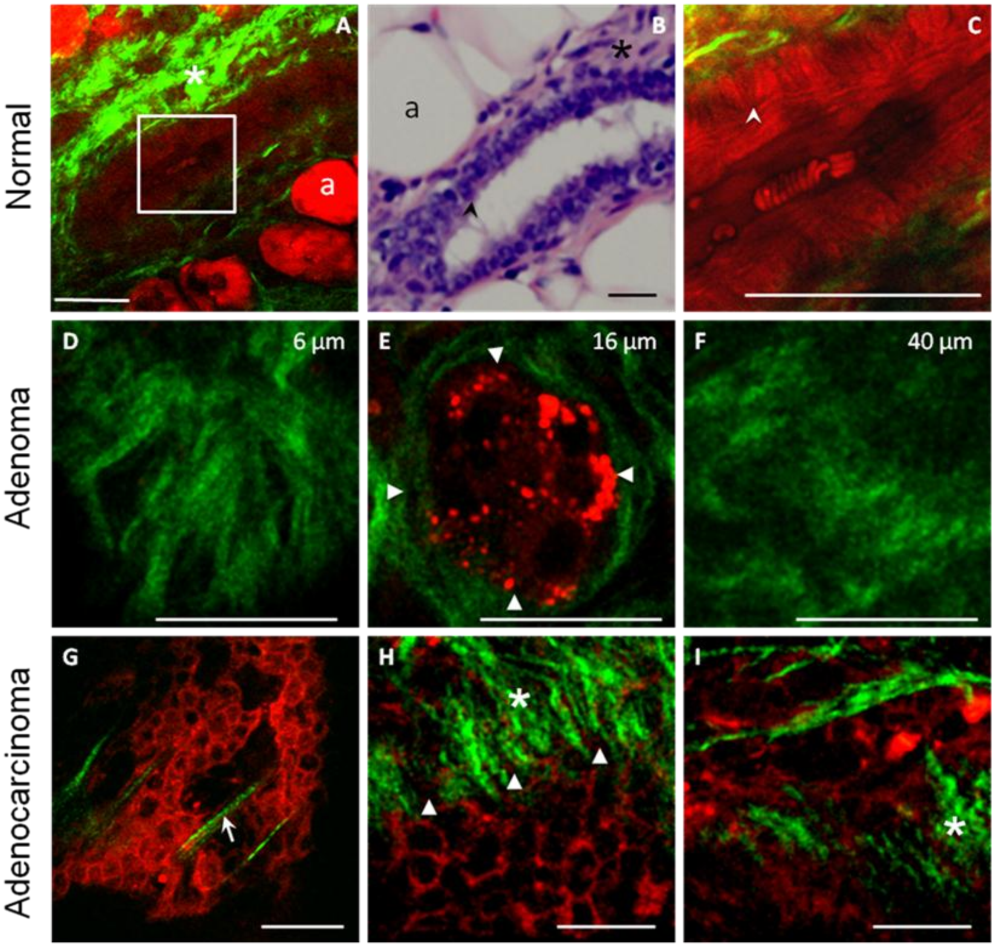

Figure 4.6 Label-free CARS and SFG imaging of normal mammary gland, mammary adenoma and adenocarcinoma in intact tissues (Red: CARS; Green: SFG). (A-C). Representative CARS and SFG images of unstained normal mammary gland *ex vivo*. Single-layer ductal cells are wrapped concentrically by bunches of wavy collagen fibrils (A, asterisk). Outside are orderly arranged adipocytes marked with "a" in A. The same features observed in intact tissue (A) are confirmed by the corresponding histological pattern (B). The box shown in A was magnified in C, which permits the single-cell resolution imaging of ductal cells (arrow head). Scale bars: 50 µm. (D-F) 3D images of adenoma show that abundant wavy collagen fibrils form a smooth organized outer contour (arrow heads) to concentrically wrap around the localized tumor mass. (G-I) Straight collagen fibrils usually observed either within (G, arrow) or perpendicularly against (H, I, asterisk) the tumor mass. The triangles in H delineate the ragged collagen boundary of tumor mass. Scale bars: 25 µm.

4.3.4 Quantitative Analysis of Collagen Density Surrounding Tumor Mass

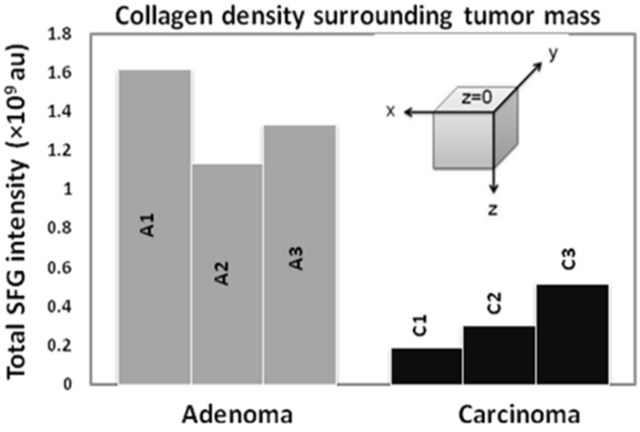

Figure 4.7 Quantitative analysis of collagen density surrounding tumor mass. Analysis of three pairs of adenoma and adenocarcinoma shows that adenoma has an average 4-fold higher collagen density surrounding tumor mass than adenocarcinoma. (Inset: simplified model that defines the dimensions of imaging; see details in Experimental Section.)

straight collagen fibrils usually observed either within (Figure 4.6G) or perpendicularly against (Figure 4.6H-I) the tumor mass. The straight collagen fibrils may act as “highways” enabling malignant tumor cells to migrate and invade towards the vasculature [381]. In addition to collagen organization, another factor that distinguished adenoma from adenocarcinoma was collagen density surrounding the tumor mass. A significant reduction of collagen density was observed in adenocarcinomas relative to adenomas. The mammary tumor status identified by the CARS/SFG imaging system was verified by the histological analysis of corresponding mammary tissues blindly.

To confirm that collagen density surrounding the tumor mass decreases in aggressive tumors, we quantitatively analyzed the collagen density surrounding adenomas and adenocarcinomas. Because SFG intensity is directly correlated with the concentration of type I collagen fibrils, we evaluated the relative collagen density of a tissue based on total SFG intensity. To systematically compare the collagen density between adenoma and adenocarcinoma, we defined a fixed analysis volume starting from the tumor mass-collagen interface and collected total SFG signals from six volumes in the mammary tumor tissues of each tumor (see Experimental Section; Figure 4.7). Consistent with our observation, quantitative analysis of SFG intensity indicated that mammary adenocarcinomas show a decrease in collagen density surrounding tumor mass by an average of 4-fold relative to mammary adenoma.

4.4 Discussion

We have distinguished normal mammary epithelial cells and mammary tumor cells based on the morphological information provided by CARS imaging. Whereas normal epithelial cells grew in a columnar shape with small nuclei and formed a single layer, tumor cells developed a round shape with large nuclei and proliferated into a multilayer cluster (Figure 4.6). Thus, our identification of tumor cells is based on the morphology and arrangement of epithelial cells. Because the CARS signals are generated from symmetric CH_2 stretch vibration, our method does not require any labeling and therefore avoids the common problem of photobleaching in fluorescence microscopy.

Although CARS was able to identify normal epithelial cells and tumor cells, it could not differentiate adenoma and adenocarcinoma by itself. Thus, we integrated CARS with SFG on the same platform, so that we were able to take advantages of both CARS and SFG to comprehensively characterize mammary tissues. SFG has been used to specifically image type I collagen fibrils [382, 383]. Here, SFG specifically recognized dense wavy collagen fibrils in normal mammary gland and mammary adenoma, as opposed to the thin straight collagen fibrils in mammary adenocarcinoma (Figure 4.6). These findings suggest that, in addition to morphological characteristics of epithelial cells, density and organization of type I collagen fibrils can also be evaluated as a crucial signature of tumor progression. Therefore, simultaneous CARS and SFG imaging of mammary tissues can indeed offer more comprehensive information compared to each individual technique. Our results have demonstrated that multimodal CARS/SFG imaging is able to accurately differentiate adenoma from adenocarcinoma in rat mammary tissues, based on morphology and arrangement of epithelial cells and 3D organization of type I collagen fibrils.

Several previous studies have shown that aberrations in type I collagen production and degradation have become one of the hallmarks of tumor stroma [384]. The observation of reduced collagen density in adenocarcinoma relative to adenoma is consistent with previous findings on proteases that degrade ECM in tumor environment [384]. More interestingly, Provenzano *et al.* defined tumor-associated collagen signatures to locate and characterize mammary tumors [385, 386]. In particular, Provenzano *et al.* claimed that collagen reorganization at the tumor-stromal interface facilitates local invasion [385]. So far, however, few studies have discussed straight collagen fibrils present in mammary adenocarcinoma. It is possible that collagenases and proteases play important roles in the formation of straight collagen fibrils to further facilitate tumor cell migration and invasion. The mechanisms underlying straight collagen formation need to be addressed in the future.

In this work, multimodal CARS/SFG imaging has shown the potential of intraoperative assessment of tumor margins. With a penetration depth of tens of microns and subcellular spatial resolution, CARS/SFG imaging provides a new contrast other than histology and enables us to identify tumor cells and their malignancy near the margin. Unlike histology, CARS/SFG imaging does not need any labeling agents, so that decisions can be made during the surgery. As a result, most normal tissues can be maintained with a negative margin. Furthermore, improvements in intraoperative margin assessment can significantly reduce local recurrence and distant metastasis induced by positive margins and re-excisions usually observed after lumpectomy. In order to achieve intraoperative margin assessment *in situ* by CARS/SFG imaging, the imaging system needs to be more compact by application of fiber lasers. The compact CARS/SFG imaging system could assist pathologists in making decisions and help surgeons remove entire malignant tumor tissues, while saving as much normal tissues as possible, within a single surgical procedure.

CHAPTER 5. OUTLOOK

5.1 Cholesterol Metabolism in Cancer

Our study has identified cholesterol esterification as a potential marker and therapeutic target of advanced PCa. Our next step, therefore, is to first validate the presence of altered cholesterol metabolism in human PCa patient specimens and prove the accumulation of CEs correlates with the clinical outcomes of PCa patients. We will then elucidate the mechanism linking cholesterol metabolism with cancer aggressiveness, and evaluate the therapeutic benefit of CE depletion in preclinical animal models of PCa. At the completion of this project, it is our expectation that we will have provided strong evidence to support the concept that inhibition of cholesterol accumulation is a viable and potentially attractive therapeutic intervention strategy to treat advanced PCa. Notably, several small molecule inhibitors of cholesterol accumulation, e.g. avasimibe, have been approved by FDA to treat atherosclerosis but failed due to the lack of effectiveness. Our proposed study would demonstrate a novel use of existing drugs to treat advanced PCa, and it is anticipated that preclinical studies and/or clinical trials will follow shortly after the completion of this project. Ultimately, the adoption of such strategy will substantially improve the clinical outcome for metastatic PCa patients that are resistant to hormone therapy. Our deeper mechanistic study will contribute to the understanding of dysregulated cholesterol metabolism in advanced PCa, which in turn provides the biological foundation of targeting cholesterol accumulation for treatment of metastatic PCa.

The *long term goal* of our project on cholesterol metabolism in cancer is to develop strategies that enable early diagnosis of aggressive tumors using elevated cholesterol metabolites as molecular markers, as well as suppression of cancer aggressiveness by modulating cholesterol metabolism pathways. Because the PI3K pathway is hyperactivated not only in advanced PCa, but also in many other human cancers, including brain, breast, renal, lymphocyte, cervical, and lung [67], cholesterol accumulation might be a common characteristic of PI3K-driven cancers. Future analysis of various types of human cancer tissues will validate whether CE is indeed a hallmark of PI3K-driven cancers, and whether CE can be used as a prognostic marker to predict cancer aggressiveness. Future elucidation of the molecular mechanisms by which PI3K pathway differentially regulates cholesterol metabolism in cancer cells from multiple tissues of origin will determine whether CE is a compelling drug target across multiple cancer types.

5.2 Membrane Lipids in Cancer

Based on the results of our study, we expect that analysis of apical polarity in live human mammary acini using Raman spectromicroscopy provides an effective screening platform to identify risk or protective factors that initiate or prevent breast cancer. We will achieve this goal with the following two steps.

The first step is to identify breast cancer risk and protective factors using Raman based screening platform. Dietary fatty acids and adipokines have been associated with breast cancer development [42, 387] Fatty acids are delivered to mammary cells mainly by uptake of LDL [263]. Dietary interventions of fatty acids can lead to rapid and potentially beneficial changes in ω3/ω6 PUFA ratio of serum and breast adipose tissue [345, 346]. The adipokines are a number of adipocyte-secreted polypeptides that have been associated with obesity and insulin resistance [42, 387]. However, a consensus is lacking on the impact of certain dietary fatty acids or adipokines on primary prevention of breast cancer [42, 388-390]. Our study has shown the capability of Raman spectromicroscopy to monitor the dynamic changes of apical polarity of the same acini over time. We will continue to test if Raman based screening platform could accurately and effectively determine the effects of a panel of dietary fatty acids and adipokines on apical polarity of mammary acini. Combinations of identified risk and potential protective factors will be further assessed to evaluate the preventative potential of the protective factors.

The second step is to reveal the impact of the identified risk and protective factors on the expression of apical polarity-associated genes. Recent findings have revealed that the status of apical polarity influences two genes of particular interest: PDPK1 and CDS1 (unpublished data, Lelièvre lab). PDPK1 functions downstream of PI3K through PDPK1's interaction with membrane phospholipids.[391] Although PDPK1 is known to be overexpressed in breast cancer,[391, 392] it has just been found to be upregulated when apical polarity is disrupted by AGA reagent, an inhibitor of gap junctional intercellular communication. CDS1 is an important precursor for the synthesis of phosphatidylinositol, whose phosphorylation plays an important role in lipid signaling [393]. Down-regulation of CDS1 has just been linked to loss of apical polarity induced by AGA reagent. By simultaneously measuring membrane lipid phase and expression of PDPK1 or CDS1 of the same acini over time, we will evaluate the change of PDPK1 or CDS1 expression when apical polarity is altered by identified risk factors or when apical polarity is restored by combining protective factors with the risk factors. This endeavor will determine whether PDPK1 or CDS1 is involved in the apical polarity alteration induced by the risk factors. The involvement of apical polarity-associated genes builds up a molecular basis for the impact of risk and protective factors on apical polarity of mammary acini, which may assist future mechanistic studies.

Finally, our approach could be extended to a multi-well plate on a dual scanning Raman spectromicroscope for high-throughput screening of numerous compounds and drugs. Future systematic study along this direction will help the design of better primary prevention strategies to reduce breast cancer incidence.

LIST OF REFERENCES

LIST OF REFERENCES

[1] R. Siegel, D. Naishadham, and A. Jemal, "Cancer statistics, 2013," *CA Cancer J. Clin.,* vol. 63, pp. 11-30, 2013.

[2] D. v. Hansemann, "Über asymmetrische Zelltheilung in Epithelhresbsen und deren biologische bedeutung," *Virchows Arch A Pathol Anat Histopathol,* vol. 119, pp. 299-326, 1890.

[3] R. J. Huebner and G. J. Todaro, "Oncogenes of RNA tumor viruses as determinants of cancer," *Proc. Natl. Acad. Sci. U.S.A.,* vol. 64, pp. 1087-1094, 1969.

[4] A. G. Knudson, "Mutation and cancer: statistical study of retinoblastoma," *Proc. Natl. Acad. Sci. U.S.A.,* vol. 68, pp. 820-823, 1971.

[5] W.-H. Lee, R. Bookstein, F. Hong, L.-J. Young, J.-Y. Shew, and E. Lee, "Human retinoblastoma susceptibility gene: cloning, identification, and sequence," *Science,* vol. 235, pp. 1394-1399, 1987.

[6] E. R. Fearon and B. Vogelstein, "A genetic model for colorectal tumorigenesis," *Cell,* vol. 61, pp. 759-767, 1990.

[7] O. Wargurg, K. Posener, and E. Negelein, "On the metabolism of carcinoma cells," *Biochemische Zeitschrift,* vol. 152, pp. 309-344, 1924.

[8] A. Schulze and A. L. Harris, "How cancer metabolism is tuned for proliferation and vulnerable to disruption," *Nature,* vol. 491, pp. 364-373, 2012.

[9] R. J. DeBerardinis, J. J. Lum, G. Hatzivassiliou, and C. B. Thompson, "The biology of cancer: metabolic reprogramming fuels cell growth and proliferation," *Cell Metab,* vol. 7, pp. 11-20, 2008.

[10] R. A. Cairns, I. S. Harris, and T. W. Mak, "Regulation of cancer cell metabolism," *Nat Rev Cancer,* vol. 11, pp. 85-95, 2011.

[11] P. S. Ward and C. B. Thompson, "Metabolic reprogramming: a cancer hallmark even warburg did not anticipate," *Cancer Cell,* vol. 21, pp. 297-308, 2012.

[12] E. Pauwels, E. Sturm, E. Bombardieri, F. Cleton, and M. Stokkel, "Positron-emission tomography with [18F] fluorodeoxyglucose," *J Cancer Res Clin Oncol,* vol. 126, pp. 549-559, 2000.

[13] D. A. Tennant, R. Durán, and E. Gottlieb, "Targeting metabolic transformation for cancer therapy," *Nat Rev Cancer,* vol. 10, pp. 267-277, 2010.

[14] D. Hanahan and R. A. Weinberg, "The hallmarks of cancer," *Cell,* vol. 100, pp. 57-70, 2000.

[15] D. Hanahan and R. A. Weinberg, "Hallmarks of cancer: the next generation," *Cell,* vol. 144, pp. 646-674, 2011.

[16] M. G. Vander Heiden, L. C. Cantley, and C. B. Thompson, "Understanding the Warburg effect: the metabolic requirements of cell proliferation," *Science,* vol. 324, pp. 1029-1033, 2009.

[17] S. Matoba, J.-G. Kang, W. D. Patino, A. Wragg, M. Boehm, O. Gavrilova, P. J. Hurley, F. Bunz, and P. M. Hwang, "p53 regulates mitochondrial respiration," *Science,* vol. 312, pp. 1650-1653, 2006.

[18] J. Son, C. A. Lyssiotis, H. Ying, X. Wang, S. Hua, M. Ligorio, R. M. Perera, C. R. Ferrone, E. Mullarky, N. Shyh-Chang, Y. a. Kang, J. B. Fleming, N. Bardeesy, J. M. Asara, M. C. Haigis, R. A. DePinho, L. C. Cantley, and A. C. Kimmelman, "Glutamine supports pancreatic cancer growth through a KRAS-regulated metabolic pathway," *Nature,* vol. 496, pp. 101-105, 2013.

[19] D. R. Wise and C. B. Thompson, "Glutamine addiction: a new therapeutic target in cancer," *Trends Biochem Sci,* vol. 35, pp. 427-433, 2010.

[20] M. Jain, R. Nilsson, S. Sharma, N. Madhusudhan, T. Kitami, A. L. Souza, R. Kafri, M. W. Kirschner, C. B. Clish, and V. K. Mootha, "Metabolite profiling identifies a key role for glycine in rapid cancer cell proliferation," *Science,* vol. 336, pp. 1040-1044, 2012.

[21] C. R. Santos and A. Schulze, "Lipid metabolism in cancer," *FEBS J.,* vol. 279, pp. 2610-2623, 2012.

[22] T. C. Walther and R. V. Farese Jr, "Lipid droplets and cellular lipid metabolism," *Annu Rev Biochem,* vol. 81, pp. 687-714, 2012.

[23] M. P. Wymann and R. Schneiter, "Lipid signalling in disease," *Nat Rev Mol Cell Biol,* vol. 9, pp. 162-176, 2008.

[24] P. G. Kopelman, "Obesity as a medical problem," *Nature,* vol. 404, pp. 635-643, 2000.

[25] K. M. Flegal, B. I. Graubard, D. F. Williamson, and M. H. Gail, "Cause-specific excess deaths associated with underweight, overweight, and obesity," *JAMA-J Am Med Assoc,* vol. 298, pp. 2028-2037, 2007.

[26] J. B. Meigs, P. W. F. Wilson, C. S. Fox, R. S. Vasan, D. M. Nathan, L. M. Sullivan, and R. B. D'Agostino, "Body mass index, metabolic syndrome, and risk of type 2 diabetes or cardiovascular disease," *J Clin Endocrinol Metab,* vol. 91, pp. 2906–2912, 2006.

[27] E. W. Gregg, Y. J. Cheng, B. L. Cadwell, G. Imperatore, D. E. Williams, K. M. Flegal, K. M. V. Narayan, and D. F. Williamson, "Secular trends in cardiovascular disease risk factors according to body mass index in US adults," *JAMA-J Am Med Assoc,* vol. 293, pp. 1868-1874, 2005.

[28] E. E. Calle, C. Rodriguez, K. Walker-Thurmond, and M. J. Thun, "Overweight, obesity, and mortality from cancer in a prospectively studied cohort of U.S. adults," *N Engl J Med,* vol. 348, pp. 1625-1638, 2003.

[29] A. Kubo and D. A. Corley, "Body mass index and adenocarcinomas of the esophagus or gastric cardia: a systematic review and meta-analysis," *Cancer Epidemiol Biomarkers Prev,* vol. 15, pp. 872-878, 2006.

[30] E. Giovannucci, G. A. Colditz, M. Starnmpfer, and W. C.Willett, "Physical activity, obesity, and risk of colorectal adenoma in women (United States)," *Cancer Causes Control,* vol. 7, pp. 253-263, 1996.

[31] A. Carmichael, "Obesity as a risk factor for development and poor prognosis of breast cancer," *BJOG-Int J Obstet Gy,* vol. 113, pp. 1160-1166, 2006.

[32] R. Ballard-Barbash and C. A. Swanson, "Body weight: estimation of risk for breast and endometrial cancers," *Am J Clin Nutr,* vol. 63, pp. 437S-441S, 1996.

[33] A. Bergström, C.-C. Hsieh, P. Lindblad, C.-M. Lu, N. Cook, and A. Wolk, "Obesity and renal cell cancer – a quantitative review," *Br J Cancer,* vol. 85, pp. 984–990, 2001.

[34] A. B. d. Gonzalez, S. Sweetland, and E. Spencer, "A meta-analysis of obesity and the risk of pancreatic cancer," *Br J Cancer,* vol. 89, pp. 519 – 523, 2003.

[35] S. Larsson and A. Wolk, "Overweight, obesity and risk of liver cancer: a meta-analysis of cohort studies," *Br J Cancer,* vol. 97, pp. 1005 – 1008, 2007.

[36] S. Larsson and A. Wolk, "Obesity and the risk of gallbladder cancer: a meta-analysis," *Br J Cancer,* vol. 96, pp. 1457-1461, 2007.

[37] G. H. Rauscher, S. T. Mayne, and D. T. Janerich, "Relation between body mass Index and lung cancer risk in men and women never and former smokers," *Am J Epidemiol,* vol. 152, pp. 506-513, 2000.

[38] J. V. Lacey, C. A. Swanson, L. A. Brinton, S. F. Altekruse, W. A. Barnes, P. E. Gravitt, M. D. Greenberg, O. C. Hadjimichael, L. McGowan, R. Mortel, P. E. Schwartz, R. J. Kurman, and A. Hildesheim, "Obesity as a potential risk factor for adenocarcinomas and squamous cell carcinomas of the uterine cervix," *Cancer,* vol. 98, pp. 814-821, 2003.

[39] L. J. Schouten, C. Rivera, D. J. Hunter, D. Spiegelman, H.-O. Adami, A. Arslan, W. L. Beeson, P. A. v. d. Brandt, J. E. Buring, A. R. Folsom, G. E. Fraser, J. L. Freudenheim, R. A. Goldbohm, S. E. Hankinson, J. V. Lacey, M. Leitzmann, A. Lukanova, J. R. Marshall, A. B. Miller, A. V. Patel, C. Rodriguez, T. E. Rohan, J. A. Ross, A. Wolk, S. M. Zhang, and S. A. Smith-Warner, "Height, body mass index, and ovarian cancer: a pooled analysis of 12 cohort studies," *Cancer Epidemiol Biomarkers Prev,* vol. 17, pp. 902-912, 2008.

[40] C. Rodriguez, S. J. Freedland, A. Deka, E. J. Jacobs, M. L. McCullough, A. V. Patel, M. J. Thun, and E. E. Calle, "Body mass index, weight change, and risk of prostate cancer in the cancer prevention study II nutrition cohort," *Cancer Epidemiol Biomarkers Prev,* vol. 16, pp. 63-69, 2007.

[41] J. A. Ross, E. Parker, C. K. Blair, J. R. Cerhan, and A. R. Folsom, "Body mass index and risk of leukemia in older women," *Cancer Epidemiol Biomarkers Prev,* vol. 13, pp. 1810-1813, 2004.

[42] E. E. Calle and R. Kaaks, "Overweight, obesity and cancer: epidemiological evidence and proposed mechanisms," *Nat Rev Cancer,* vol. 4, pp. 579-591, 2004.

[43] L. N. Kolonel, A. M. Nomura, and R. V. Cooney, "Dietary fat and prostate cancer: current status," *J. Natl. Cancer Inst.,* vol. 91, pp. 414-428, 1999.

[44] A. C. M. Thiébaut, A. Schatzkin, R. Ballard-Barbash, and V. Kipnis, "Dietary fat and breast cancer: contributions from a survival trial," *J Nat Cancer Inst,* vol. 98, pp. 1753-1755, 2006.

[45] L. Kushi and E. Giovannucci, "Dietary fat and cancer," *Am J Med,* vol. 113, pp. 63-70, 2002.

[46] W. C. Willett, "Dietary fat intake and cancer risk: a controversial and instructive story," *Semin Cancer Biol,* vol. 8, pp. 245-253, 1998.

[47] M. E. Martínez and E. Giovannucci, "Diet and the prevention of cancer," *Cancer Metastasis Rev,* vol. 16, pp. 357-376, 1997.

[48] D. Bagga, S. Capone, H. J. Wang, D. Heber, M. Lill, L. Chap, and J. A. Glaspy, "Dietary modulation of omega-3-omega-6 polyunsaturated fatty acid ratios in patients with breast cancer," *J Natl Cancer Inst,* vol. 89, pp. 1123-1131, 1997.

[49] N. Kobayashi, R. J. Barnard, S. M. Henning, D. Elashoff, S. T. Reddy, P. Cohen, P. Leung, J. Hong-Gonzalez, S. J. Freedland, J. Said, D. Gui, N. P. Seeram, L. M. Popoviciu, D. Bagga, D. Heber, J. A. Glaspy, and W. J. Aronson, "Effect of altering dietary w-6/w-3 fatty acid ratios on prostate cancer membrane composition, cyclooxygenase-2, and prostaglandin E2," *Clin Cancer Res,* vol. 12, pp. 4662-4670, 2006.

[50] C. H. MacLean, S. J. Newberry, W. A. Mojica, P. Khanna, A. M. Issa, M. J. Suttorp, Y.-W. Lim, S. B. Traina, L. Hilton, R. Garland, and S. C. Morton, "Effects of omega-3 fatty acids on cancer risk," *JAMA-J Am Med Assoc,* vol. 295, pp. 403-415, 2006.

[51] N. Potischman, C. E. McCulloch, T. Byers, L. Houghton, T. Nemoto, S. Graham, and T. C. Campbell, "Associations between breast cancer, plasma triglycerides, and cholesterol," *Nutr Cancer,* vol. 15, pp. 205-215, 1991.

[52] G. McKeown-Eyssen, "Epidemiology of colorectal cancer revisited: are serum triglycerides and/or plasma glucose associated with risk?," *Cancer Epidemiol. Biomarkers Prev,* vol. 3, pp. 687-695, December 1, 1994 1994.

[53] K. Yamada, S. Araki, M. Tamura, I. Sakai, Y. Takahashi, H. Kashihara, and S. Kono, "Relation of serum total cholesterol, serum triglycerides and fasting plasma glucose to colorectal carcinoma in situ," *Int J Epidemiol,* vol. 27, pp. 794-798, 1998.

[54] H. Ulmer, W. Borena, K. Rapp, J. Klenk, A. Strasak, G. Diem, H. Concin, and G. Nagel, "Serum triglyceride concentrations and cancer risk in a large cohort study in Austria," *Br J Cancer,* vol. 101, pp. 1202-1206, 2009.

[55] W. Borena, T. Stocks, H. Jonsson, S. Strohmaier, G. Nagel, T. Bjørge, J. Manjer, G. Hallmans, R. Selmer, M. Almquist, C. Häggström, A. Engeland, S. Tretli, H. Concin, A. Strasak, P. Stattin, and H. Ulmer, "Serum triglycerides and cancer risk in the metabolic syndrome and cancer (Me-Can) collaborative study," *Cancer Causes Control,* vol. 22, pp. 291-299, 2011.

[56] L. J. Vatten and O. P. Foss, "Total serum cholesterol and triglycerides and risk of breast cancer: a prospective study of 24,329 Norwegian women," *Cancer Res,* vol. 50, pp. 2341-2346, April 15, 1990 1990.

[57] M. D. Holmes, D. J. Hunter, G. A. Colditz, M. J. Stampfer, S. E. Hankinson, F. E. Speizer, B. Rosner, and W. C. Willett, "Association of dietary intake of fat and fatty acids with risk of breast cancer," *JAMA-J Am Med Assoc,* vol. 281, pp. 914-920, 1999.

[58] K. Siemianowicz, J. Gminski, M. Stajszczyk, W. Wojakowski, M. Goss, M. Machalski, A. Telega, K. Brulinski, and H. Magiera-Molendowska, "Serum total cholesterol and triglycerides levels in patients with lung cancer," *Int J Mol Med,* vol. 5, p. 201, 2000.

[59] P. E. Fielding and C. J. Fielding, "Dynamics of lipoprotein transport in the circulatory system," in *Biochemistry of Lipids, Lipoproteins, and Membranes*. vol. 20, J. E. Vance and D. E. Vance, Eds. New York: Elsevier Science Publishing Co. Inc., 1991, pp. 427-59.

[60] C. Ehnholm, *Cellular lipid metabolism*: Springer, 2009.

[61] F. P. Kuhajda, K. Jenner, F. D. Wood, R. A. Hennigar, L. B. Jacobs, J. D. Dick, and G. R. Pasternack, "Fatty acid synthesis: a potential selective target for antineoplastic therapy," *Proc. Natl. Acad. Sci. U.S.A.,* vol. 91, pp. 6379-6383, 1994.

[62] J. A. Menendez and R. Lupu, "Fatty acid synthase and the lipogenic phenotype in cancer pathogenesis," *Nat Rev Cancer,* vol. 7, pp. 763-777, 2007.

[63] G. Hatzivassiliou, F. Zhao, D. E. Bauer, C. Andreadis, A. N. Shaw, D. Dhanak, S. R. Hingorani, D. A. Tuveson, and C. B. Thompson, "ATP citrate lyase inhibition can suppress tumor cell growth," *Cancer Cell,* vol. 8, pp. 311-321, 2005.

[64] T. Migita, T. Narita, K. Nomura, E. Miyagi, F. Inazuka, M. Matsuura, M. Ushijima, T. Mashima, H. Seimiya, and Y. Satoh, "ATP citrate lyase: activation and therapeutic implications in non-small cell lung cancer," *Cancer Res,* vol. 68, pp. 8547-8554, 2008.

[65] V. Chajès, M. Cambot, K. Moreau, G. M. Lenoir, and V. Joulin, "Acetyl-CoA carboxylase α is essential to breast cancer cell survival," *Cancer Res,* vol. 66, pp. 5287-5294, 2006.

[66] A. Beckers, S. Organe, L. Timmermans, K. Scheys, A. Peeters, K. Brusselmans, G. Verhoeven, and J. V. Swinnen, "Chemical inhibition of acetyl-CoA carboxylase induces growth arrest and cytotoxicity selectively in cancer cells," *Cancer Res,* vol. 67, pp. 8180-8187, 2007.

[67] J. Luo, B. D. Manning, and L. C. Cantley, "Targeting the PI3K-Akt pathway in human cancer: Rationale and promise," *Cancer Cell,* vol. 4, pp. 257-262, 2003.

[68] B. B. Friday and A. A. Adjei, "Advances in targeting the Ras/Raf/MEK/Erk mitogen-activated protein kinase cascade with MEK inhibitors for cancer therapy," *Clin Cancer Res,* vol. 14, pp. 342-346, 2008.

[69] T. Porstmann, C. R. Santos, B. Griffiths, M. Cully, M. Wu, S. Leevers, J. R. Griffiths, Y. L. Chung, and A. Schulze, "SREBP activity is regulated by mTORC1 and contributes to Akt-dependent cell growth," *Cell Metab.,* vol. 8, pp. 224-236, 2008.

[70] M. S. Brown and J. L. Goldstein, "The SREBP pathway: regulation of cholesterol metabolism by proteolysis of a membrane-bound transcription factor," *Cell,* vol. 89, pp. 331-340, 1997.

[71] D. Eberle, B. Hegarty, P. Bossard, P. Ferré, and F. Foufelle, "SREBP transcription factors: master regulators of lipid homeostasis," *Biochimie,* vol. 86, pp. 839-848, 2004.

[72] F. Zhang and G. Du, "Dysregulated lipid metabolism in cancer," *World J Biol Chem,* vol. 3, p. 167, 2012.

[73] D. K. Nomura, J. Z. Long, S. Niessen, H. S. Hoover, S.-W. Ng, and B. F. Cravatt, "Monoacylglycerol lipase regulates a fatty acid network that promotes cancer pathogenesis," *Cell,* vol. 140, pp. 49-61, 2010.

[74] D. K. Nomura, D. P. Lombardi, J. W. Chang, S. Niessen, A. M. Ward, J. Z. Long, H. H. Hoover, and B. F. Cravatt, "Monoacylglycerol Lipase Exerts Dual Control over Endocannabinoid and Fatty Acid Pathways to Support Prostate Cancer," *Chemistry & Biology,* vol. 18, pp. 846-856, 2011.

[75] Y. Liu, "Fatty acid oxidation is a dominant bioenergetic pathway in prostate cancer," *Prostate Cancer Prostatic Dis,* vol. 9, pp. 230-234, 2006.

[76] R. T. Dorsam and J. S. Gutkind, "G-protein-coupled receptors and cancer," *Nat Rev Cancer,* vol. 7, pp. 79-94, 2007.

[77] D. Z. Wang and R. N. Dubois, "Eicosanoids and cancer," *Nat Rev Cancer,* vol. 10, pp. 181-193, 2010.

[78] T. Fujimoto, Y. Ohsaki, J. Cheng, M. Suzuki, and Y. Shinohara, "Lipid droplets: a classic organelle with new outfits," *Histochem. Cell Biol.,* vol. 130, pp. 263-279, Aug 2008.

[79] D. J. Murphy, "The biogenesis and functions of lipid bodies in animals, plants and microorganisms," *Prog. Lipid Res.,* vol. 40, pp. 325-438, 2001.

[80] M. Beller, K. Thiel, P. J. Thul, and H. Jackle, "Lipid droplets: A dynamic organelle moves into focus," *FEBS Lett.,* vol. 584, pp. 2176-2182, 2010.

[81] R. V. Farese and T. C. Walther, "Lipid droplets finally get a little R-E-S-P-E-C-T," *Cell,* vol. 139, pp. 855-860, 2009.

[82] C. V. Ramos and H. B. Taylor, "Lipid-rich carcinoma of breast - a clinicopathologic analysis of 13 examples," *Cancer,* vol. 33, pp. 812-819, 1974.

[83] J. M. Hakumäki and R. A. Kauppinen, "1H NMR visible lipids in the life and death of cells," *Trends Biochem. Sci.,* vol. 25, pp. 357-362, 2000.

[84] M. T. Accioly, P. Pacheco, C. M. Maya-Monteiro, N. Carrossini, B. K. Robbs, S. S. Oliveira, C. Kaufmann, J. A. Morgado-Diaz, P. T. Bozza, and J. P. B. Viola, "Lipid bodies are reservoirs of cyclooxygenase-2 and sites of prostaglandin-E2 synthesis in colon cancer cells," *Cancer Res.,* vol. 68, pp. 1732-1740, 2008.

[85] P. P. Rosen, *Rosen's breast pathology,* 3rd ed. New York: Lippincott Williams & Wilkins, 2008.

[86] R. A. Karmali, "Prostaglandins and cancer," *CA Cancer J. Clin.,* vol. 33, pp. 322-332, 1983.

[87] J. V. Swinnen, P. P. VanVeldhoven, M. Esquenet, W. Heyns, and G. Verhoeven, "Androgens markedly stimulate the accumulation of neutral lipids in the human prostatic adenocarcinoma cell line LNCaP," *Endocrinology,* vol. 137, pp. 4468-4474, 1996.

[88] J. V. Swinnen, M. Esquenet, K. Goossens, W. Heyns, and G. Verhoeven, "Androgens stimulate fatty acid synthase in the human prostate cancer cell line LNCaP," *Cancer Res.,* vol. 57, pp. 1086-1090, 1997.

[89] D. L. Herber, W. Cao, Y. Nefedova, S. V. Novitskiy, S. Nagaraj, V. A. Tyurin, A. Corzo, H. I. Cho, E. Celis, B. Lennox, S. C. Knight, T. Padhya, T. V. McCaffrey, J. C. McCaffrey, S. Antonia, M. Fishman, R. L. Ferris, V. E. Kagan, and D. I. Gabrilovich, "Lipid accumulation and dendritic cell dysfunction in cancer," *Nat Med,* vol. 16, pp. 880-U57, Aug 2010.

[90] P. T. Bozza and J. P. B. Viola, "Lipid droplets in inflammation and cancer," *Prostag. Leukotr. Ess.,* vol. 82, pp. 243-250, 2010.

[91] K. Simons and E. Ikonen, "How cells handle cholesterol," *Science,* vol. 290, pp. 1721-1726, 2000.

[92] D. Lloyd-Jones, R. Adams, M. Carnethon, G. De Simone, T. B. Ferguson, K. Flegal, E. Ford, K. Furie, A. Go, K. Greenlund, N. Haase, S. Hailpern, M. Ho, V. Howard, B. Kissela, S. Kittner, D. Lackland, L. Lisabeth, A. Marelli, M. McDermott, J. Meigs, D. Mozaffarian, G. Nichol, C. O'Donnell, V. Roger, W. Rosamond, R. Sacco, P. Sorlie, R. Stafford, J. Steinberger, T. Thom, S. Wasserthiel-Smoller, N. Wong, J. Wylie-Rosett, and Y. Hong, "Heart Disease and Stroke Statistics-2009 Update: A Report From the American Heart Association Statistics Committee and Stroke Statistics Subcommittee," *Circulation,* vol. 119, pp. 480-486, 2009.

[93] E. Ikonen, "Cellular cholesterol trafficking and compartmentalization," *Nat Rev Mol Cell Biol,* vol. 9, pp. 125-138, 2008.

[94] "American Cancer Society. *Cancer Prevention & Early Detection Facts & Figures 2013*. Atlanta: American Cancer Society; 2013."

[95] J. Hu, C. La Vecchia, M. de Groh, E. Negri, H. Morrison, and L. Mery, "Dietary cholesterol intake and cancer," *Ann. Oncol.,* vol. 23, pp. 491-500, 2012.

[96] Y. S. Lin, A. Tamakoshi, T. Hayakawa, S. Naruse, M. Kitagawa, and Y. Ohno, "Nutritional factors and risk of pancreatic cancer: a population-based case-control study based on direct interview in Japan," *J Gastroenterol,* vol. 40, pp. 297-301, 2005.

[97] D. S. Michaud, E. Giovannucci, W. C. Willett, G. A. Colditz, and C. S. Fuchs, "Dietary meat, dairy products, fat, and cholesterol and pancreatic cancer risk in a prospective study," *Am J Epidemiol,* vol. 157, pp. 1115-1125, Jun 2003.

[98] K. Liu, D. Moss, V. Persky, J. Stamler, D. Garside, and I. Soltero, "Dietary-cholesterol, fat, and fiber, and colon-cancer mortality - analysis of international data," *Lancet,* vol. 2, pp. 782-785, 1979.

[99] R. Jarvinen, P. Knekt, T. Hakulinen, H. Rissanen, and M. Heliovaara, "Dietary fat, cholesterol and colorectal cancer in a prospective study," *Br J Cancer,* vol. 85, pp. 357-361, 2001.

[100] E. DeStefani, M. Mendilaharsu, H. DeneoPellegrini, and A. Ronco, "Influence of dietary levels of fat, cholesterol, and calcium on colorectal cancer," *Nutr. Cancer,* vol. 29, pp. 83-89, 1997.

[101] J. P. Cruse, M. R. Lewin, and C. G. Clark, "An investigation into the mechanism of co-carcinogenesis of dietary-cholesterol during the induction of colon cancer in rats by 1,2 dimethylhydrazine," *Clin Oncol,* vol. 10, pp. 213-220, 1984.

[102] J. P. Cruse, M. R. Lewin, G. P. Ferulano, and C. G. Clark, "Co-carcinogenic effects of dietary cholesterol in experimental colon cancer," *Nature,* vol. 276, pp. 822-825, 1978.

[103] J. P. Cruse, M. R. Lewin, and C. G. Clark, "Dietary-cholesterol deprivation improves survival and reduces incidence of metastatic colon cancer in dimethylhydrazine-pretreated rats," *Gut,* vol. 23, pp. 594-599, 1982.

[104] M. T. Goodman, L. N. Kolonel, C. N. Yoshizawa, and J. H. Hankin, "The effect of dietary cholesterol and fat on the risk of lung cancer in hawaii," *Am J Epidemiol,* vol. 128, pp. 1241-1255, 1988.

[105] M. W. Hinds, L. N. Kolonel, J. H. Hankin, and J. Lee, "Dietary-cholesterol and lung-cancer risk in a multiethnic population in Hawaii," *Int J Cancer,* vol. 32, pp. 727-732, 1983.

[106] M. W. Hinds, L. N. Kolonel, J. Lee, and J. H. Hankin, "Dietary-cholesterol and lung-cancer risk among men in Hawaii," *Am J Clin Nutr,* vol. 37, pp. 192-193, 1983.

[107] L. K. Heilbrun, A. M. Nomura, and G. N. Stemmermann, "Dietary cholesterol and lung cancer risk among Japanese men in Hawaii," *Am J Clin Nutr,* vol. 39, pp. 375-9, 1984.

[108] P. Knekt, R. Seppänen, R. Järvinen, J. Virtamo, L. Hyvönen, E. Pukkala, and L. Teppo, "Dietary cholesterol, fatty acids, and the risk of lung cancer among men," *Nutr Cancer,* vol. 16, pp. 267-275, 1991.

[109] J. M. Genkinger, D. J. Hunter, D. Spiegelman, K. E. Anderson, W. L. Beeson, J. E. Buring, G. A. Colditz, G. E. Fraser, J. L. Freudenheim, R. A. Goldbohm, S. E. Hankinson, K. L. Koenig, S. C. Larsson, M. Leitzmann, M. L. McCullough, A. B. Miller, C. Rodriguez, T. E. Rohan, J. A. Ross, A. Schatzkin, L. J. Schouten, E. Smit, W. C. Willett, A. Wolk, A. Zeleniuch-Jacquotte, S. M. M. Zhang, and S. Smith-Warner, "A pooled analysis of 12 cohort studies of dietary fat, cholesterol and egg intake and ovarian cancer," *Cancer Causes Control,* vol. 17, pp. 273-285, 2006.

[110] L. A. Cohen and P. C. Chan, "Dietary cholesterol and experimental mammary cancer development," *Nutr Cancer,* vol. 4, pp. 99-106, 1982 1982.

[111] C. M. Kitahara, A. Berrington de González, N. D. Freedman, R. Huxley, Y. Mok, S. H. Jee, and J. M. Samet, "Total cholesterol and cancer risk in a large prospective study in Korea," *J Clin Oncol,* vol. 29, pp. 1592-1598, 2011.

[112] M. Eichholzer, H. B. Stähelin, F. Gutzwiller, E. Lüdin, and F. Bernasconi, "Association of low plasma cholesterol with mortality for cancer at various sites in men: 17-y follow-up of the prospective Basel study," *Am J Clin Nutr,* vol. 71, pp. 569-574, 2000.

[113] S. B. Kritchevsky and D. Kritchevsky, "Serum cholesterol and cancer risk: an epidemiologic perspective," *Annu Rev Nutr,* vol. 12, pp. 391-416, 1992.

[114] R. W. Sherwin, D. N. Wentworth, J. A. Cutler, S. B. Hulley, L. H. Kuller, and J. Stamler, "Serum cholesterol levels and cancer mortality in 361662 men screened for the multiple risk factor intervention trial," *JAMA-J Am Med Assoc,* vol. 257, pp. 943-948, 1987.

[115] S. J. Sharp and S. J. Pocock, "Time trends in serum cholesterol before cancer death," *Epidemiology,* vol. 8, pp. 132-136, 1997.

[116] J. Ahn, U. Lim, S. J. Weinstein, A. Schatzkin, R. B. Hayes, J. Virtamo, and D. Albanes, "Prediagnostic total and high-density lipoprotein cholesterol and risk of cancer," *Cancer Epidemiol. Biomarkers Prev,* vol. 18, pp. 2814-2821, 2009.

[117] S. Dessi, B. Batetta, O. Spano, F. Sanna, M. Tonello, M. Giacchino, L. Tessitore, P. Costelli, F. M. Baccino, and E. Madon, "Clinical remission is associated with restoration of normal high-density lipoprotein cholesterol levels in children with malignancies," *Clin Sci,* vol. 89, pp. 505-510, 1995.

[118] E. A. Platz, C. Till, P. J. Goodman, H. L. Parnes, W. D. Figg, D. Albanes, M. L. Neuhouser, E. A. Klein, I. M. Thompson, and A. R. Kristal, "Men with low serum cholesterol have a lower risk of high-grade prostate cancer in the placebo arm of the prostate cancer prevention trial," *Cancer Epidemiol. Biomarkers Prev,* vol. 18, pp. 2807-2813, 2009.

[119] E. A. Platz, S. K. Clinton, and E. Giovannucci, "Association between plasma cholesterol and prostate cancer in the PSA era," *Int J Cancer,* vol. 123, pp. 1693-1698, 2008.

[120] K. Shafique, P. McLoone, K. Qureshi, H. Leung, C. Hart, and D. S. Morrison, "Cholesterol and the risk of grade-specific prostate cancer incidence: evidence from two large prospective cohort studies with up to 37 years' follow up," *BMC Cancer,* vol. 12, p. 25, 2012.

[121] A. M. Mondul, S. L. Clipp, K. J. Helzlsouer, and E. A. Platz, "Association between plasma total cholesterol concentration and incident prostate cancer in the CLUE II cohort," *Cancer Causes Control,* vol. 21, pp. 61-68, 2011.

[122] M. Van Hemelrijck, H. Garmo, L. Holmberg, G. Walldius, I. Jungner, N. Hammar, and M. Lambe, "Prostate cancer risk in the Swedish AMORIS study," *Cancer,* vol. 117, pp. 2086-2095, 2011.

[123] M. Van Hemelrijck, G. Walldius, I. Jungner, N. Hammar, H. Garmo, E. Binda, A. Hayday, M. Lambe, and L. Holmberg, "Low levels of apolipoprotein A-I and HDL are associated with risk of prostate cancer in the Swedish AMORIS study," *Cancer Causes Control,* vol. 22, pp. 1011-1019, 2011.

[124] A. M. Mondul, S. J. Weinstein, J. Virtamo, and D. Albanes, "Serum total and HDL cholesterol and risk of prostate cancer," *Cancer Causes Control,* vol. 22, pp. 1545-1552, 2011.

[125] L. Zhuang, J. Kim, R. M. Adam, K. R. Solomon, and M. R. Freeman, "Cholesterol targeting alters lipid raft composition and cell survival in prostate cancer cells and xenografts," *J Clin Invest,* vol. 115, pp. 959-968, 2005.

[126] E. A. Mostaghel, K. R. Solomon, K. Pelton, M. R. Freeman, and R. B. Montgomery, "Impact of circulating cholesterol levels on growth and intratumoral androgen concentration of prostate tumors," *PLoS ONE,* vol. 7, p. e30062, 2012.

[127] K. R. Solomon, K. Pelton, K. Boucher, J. Joo, C. Tully, D. Zurakowski, C. P. Schaffner, J. Kim, and M. R. Freeman, "Ezetimibe is an inhibitor of tumor angiogenesis," *Am J Pathol,* vol. 174, pp. 1017-1026, 2009.

[128] G. Llaverias, C. Danilo, Y. Wang, A. K. Witkiewicz, K. Daumer, M. P. Lisanti, and P. G. Frank, "A western-type diet accelerates tumor progression in an autochthonous mouse model of prostate cancer," *Am J Pathol,* vol. 177, pp. 3180-3191, 2010.

[129] A. Eliassen, G. A. Colditz, B. Rosner, W. C. Willett, and S. E. Hankinson, "Serum lipids, lipid-lowering drugs, and the risk of breast cancer," *Arch Intern Med,* vol. 165, pp. 2264-2271, 2005.

[130] M. Ha, J. Sung, and Y.-M. Song, "Serum total cholesterol and the risk of breast cancer in postmenopausal Korean women," *Cancer Causes Control,* vol. 20, pp. 1055-1060, 2009.

[131] J. Manjer, R. Kaaks, E. Riboli, and G. Berglund, "Risk of breast cancer in relation to anthropometry, blood pressure, blood lipids and glucose metabolism: a prospective study within the Malmö Preventive Project," *Eur J Cancer Prev,* vol. 10, pp. 33-42, 2001.

[132] M. Bahl, M. Ennis, I. Tannock, J. Hux, K. Pritchard, J. Koo, and P. Goodwin, "Serum lipids and outcome of early-stage breast cancer: results of a prospective cohort study," *Breast Cancer Res Treat,* vol. 94, pp. 135-144, 2005.

[133] L. J. Vatten, O. P. Foss, and S. Kvinnsland, "Overall survival of breast cancer patients in relation to preclinically determined total serum cholesterol, body mass index, height and cigarette smoking: a population-based study," *Eur J Cancer Clin Oncol,* vol. 27, pp. 641-646, 1991.

[134] I. Delimaris, E. Faviou, G. Antonakos, E. Stathopoulou, A. Zachari, and A. Dionyssiou-Asteriou, "Oxidized LDL, serum oxidizability and serum lipid levels in patients with breast or ovarian cancer," *Clin Biochem,* vol. 40, pp. 1129-1134, 2007.

[135] A. J. Li, R. G. Elmore, I. Y.-d. Chen, and B. Y. Karlan, "Serum low-density lipoprotein levels correlate with survival in advanced stage epithelial ovarian cancers," *Gynecol Oncol,* vol. 116, pp. 78-81, 2010.

[136] F. J. B. van Duijnhoven, H. B. Bueno-De-Mesquita, M. Calligaro, M. Jenab, T. Pischon, E. H. J. M. Jansen, J. Frohlich, A. Ayyobi, K. Overvad, A. P. Toft-Petersen, A. Tjønneland, L. Hansen, M.-C. Boutron-Ruault, F. Clavel-Chapelon, V. Cottet, D. Palli, G. Tagliabue, S. Panico, R. Tumino, P. Vineis, R. Kaaks, B. Teucher, H. Boeing, D. Drogan, A. Trichopoulou, P. Lagiou, V. Dilis, P. H. M. Peeters, P. D. Siersema, L. Rodríguez, C. A. González, E. Molina-Montes, M. Dorronsoro, M.-J. Tormo, A. Barricarte, R. Palmqvist, G. Hallmans, K.-T. Khaw, K. K. Tsilidis, F. L. Crowe, V. Chajes, V. Fedirko, S. Rinaldi, T. Norat, and E. Riboli, "Blood lipid and lipoprotein concentrations and colorectal cancer risk in the European Prospective Investigation into Cancer and Nutrition," *Gut,* vol. 60, pp. 1094-1102, 2011.

[137] K. Suzuki, Y. Ito, K. Wakai, M. Kawado, S. Hashimoto, H. Toyoshima, M. Kojima, S. Tokudome, N. Hayakawa, Y. Watanabe, K. Tamakoshi, S. Suzuki, K. Ozasa, and A. Tamakoshi, "Serum oxidized low-density lipoprotein levels and risk of colorectal cancer: a case-control study nested in the Japan collaborative cohort study," *Cancer Epidemiol. Biomarkers Prev,* vol. 13, pp. 1781-1787, 2004.

[138] M. Notarnicola, D. F. Altomare, M. Correale, E. Ruggieri, B. D'Attoma, A. Mastrosimini, V. Guerra, and M. G. Caruso, "Serum lipid profile in colorectal cancer patients with and without synchronous distant metastases," *Oncology,* vol. 68, pp. 371-4, 2005.

[139] M. F. Demierre, P. D. Higgins, S. B. Gruber, E. Hawk, and S. M. Lippman, "Statins and cancer prevention," *Nat Rev Cancer,* vol. 5, pp. 930-42, 2005.

[140] K. R. Solomon and M. R. Freeman, "Do the cholesterol-lowering properties of statins affect cancer risk?," *Trends Endocrinol Metab,* vol. 19, pp. 113-21, 2008.

[141] S. F. Nielsen, B. G. Nordestgaard, and S. E. Bojesen, "Statin use and reduced cancer-related mortality," *N Engl J Med,* vol. 367, pp. 1792-802, Nov 8 2012.

[142] T. J. Murtola, T. Visakorpi, J. Lahtela, H. Syvala, and T. Tammela, "Statins and prostate cancer prevention: where we are now, and future directions," *Nat Clin Pract Urol,* vol. 5, pp. 376-87, 2008.

[143] K. Pelton, M. R. Freeman, and K. R. Solomon, "Cholesterol and prostate cancer," *Curr Opin Pharmacol,* vol. 12, pp. 751-9, 2012.

[144] E. J. Jacobs, C. C. Newton, M. J. Thun, and S. M. Gapstur, "Long-term use of cholesterol-lowering drugs and cancer incidence in a large United States cohort," *Cancer Res,* vol. 71, pp. 1763-71, 2011.

[145] C. C. Chang, S. C. Ho, H. F. Chiu, and C. Y. Yang, "Statins increase the risk of prostate cancer: a population-based case-control study," *Prostate,* vol. 71, pp. 1818-24, 2011.

[146] C. R. Ritch, G. Hruby, K. K. Badani, M. C. Benson, and J. M. McKiernan, "Effect of statin use on biochemical outcome following radical prostatectomy," *BJU Int,* vol. 108, pp. E211-6, 2011.

[147] E. A. Platz, M. F. Leitzmann, K. Fisvanathan, E. B. Rimm, M. J. Stampfer, W. C. Willett, and E. Giovannucci, "Statin drugs and risk of advanced prostate cancer," *J. Natl. Cancer Inst.,* vol. 98, pp. 1819-1825, 2006.

[148] E. D. Flick, L. A. Habel, K. A. Chan, S. K. Van Den Eeden, V. P. Quinn, R. Haque, E. J. Orav, J. D. Seeger, M. C. Sadler, C. P. Quesenberry, Jr., B. Sternfeld, S. J. Jacobsen, R. A. Whitmer, and B. J. Caan, "Statin use and risk of prostate cancer in the California Men's Health Study cohort," *Cancer Epidemiol Biomarkers Prev,* vol. 16, pp. 2218-25, 2007.

[149] E. J. Jacobs, C. Rodriguez, E. B. Bain, Y. Wang, M. J. Thun, and E. E. Calle, "Cholesterol-lowering drugs and advanced prostate cancer incidence in a large U.S. cohort," *Cancer Epidemiol Biomarkers Prev,* vol. 16, pp. 2213-7, 2007.

[150] T. J. Murtola, T. L. Tammela, J. Lahtela, and A. Auvinen, "Cholesterol-lowering drugs and prostate cancer risk: a population-based case-control study," *Cancer Epidemiol Biomarkers Prev,* vol. 16, pp. 2226-32, 2007.

[151] R. H. Breau, R. J. Karnes, D. J. Jacobson, M. E. McGree, S. J. Jacobsen, A. Nehra, M. M. Lieber, and J. L. St Sauver, "The association between statin use and the diagnosis of prostate cancer in a population based cohort," *J Urol,* vol. 184, pp. 494-9, 2010.

[152] N. Tan, E. A. Klein, J. Li, A. S. Moussa, and J. S. Jones, "Statin use and risk of prostate cancer in a population of men who underwent biopsy," *J Urol,* vol. 186, pp. 86-90, 2011.

[153] W. R. Farwell, L. W. D'Avolio, R. E. Scranton, E. V. Lawler, and J. M. Gaziano, "Statins and prostate cancer diagnosis and grade in a veterans population," *J Natl Cancer Inst,* vol. 103, pp. 885-92, 2011.

[154] M. Alizadeh, M. P. Sylvestre, T. Zilli, T. Van Nguyen, J. P. Guay, J. P. Bahary, and D. Taussky, "Effect of statins and anticoagulants on prostate cancer aggressiveness," *Int J Radiat Oncol Biol Phys,* vol. 83, pp. 1149-53, 2012.

[155] J. H. Fowke, S. S. Motley, D. A. Barocas, M. S. Cookson, R. Concepcion, S. Byerly, and J. A. Smith, Jr., "The associations between statin use and prostate cancer screening, prostate size, high-grade prostatic intraepithelial neoplasia (PIN), and prostate cancer," *Cancer Causes Control,* vol. 22, pp. 417-26, 2011.

[156] M. A. Kollmeier, M. S. Katz, K. Mak, Y. Yamada, D. J. Feder, Z. Zhang, X. Jia, W. Shi, and M. J. Zelefsky, "Improved biochemical outcomes with statin use in patients with high-risk localized prostate cancer treated with radiotherapy," *Int J Radiat Oncol Biol Phys,* vol. 79, pp. 713-8, 2011.

[157] A. M. Mondul, M. Han, E. B. Humphreys, C. L. Meinhold, P. C. Walsh, and E. A. Platz, "Association of statin use with pathological tumor characteristics and prostate cancer recurrence after surgery," *J Urol,* vol. 185, pp. 1268-73, 2011.

[158] S. W. Marcella, A. David, P. A. Ohman-Strickland, J. Carson, and G. G. Rhoads, "Statin use and fatal prostate cancer: a matched case-control study," *Cancer,* vol. 118, pp. 4046-52, 2012.

[159] S. Bonovas, K. Filioussi, N. Tsavaris, and N. M. Sitaras, "Use of statins and breast cancer: a meta-analysis of seven randomized clinical trials and nine observational studies," *J Clin Oncol,* vol. 23, pp. 8606-12, 2005.

[160] T. P. Ahern, L. Pedersen, M. Tarp, D. P. Cronin-Fenton, J. P. Garne, R. A. Silliman, H. T. Sorensen, and T. L. Lash, "Statin prescriptions and breast cancer recurrence risk: a Danish nationwide prospective cohort study," *J Natl Cancer Inst,* vol. 103, pp. 1461-8, 2011.

[161] M. L. Kwan, L. A. Habel, E. D. Flick, C. P. Quesenberry, and B. Caan, "Post-diagnosis statin use and breast cancer recurrence in a prospective cohort study of early stage breast cancer survivors," *Breast Cancer Res Treat,* vol. 109, pp. 573-9, 2008.

[162] J. A. Cauley, A. McTiernan, R. J. Rodabough, A. LaCroix, D. C. Bauer, K. L. Margolis, E. D. Paskett, M. Z. Vitolins, C. D. Furberg, and R. T. Chlebowski, "Statin use and breast cancer: prospective results from the Women's Health Initiative," *J Natl Cancer Inst,* vol. 98, pp. 700-7, 2006.

[163] T. M. Prowell, V. Stearns, and B. Trock, "Lipophilic statins merit additional study for breast cancer chemoprevention," *J Clin Oncol,* vol. 24, pp. 2128-9, 2006.

[164] T. M. Brewer, H. Masuda, D. D. Liu, Y. Shen, P. Liu, T. Iwamoto, K. Kai, C. M. Barnett, W. A. Woodward, J. M. Reuben, P. Yang, G. N. Hortobagyi, and N. T. Ueno, "Statin use in primary inflammatory breast cancer: a cohort study," *Br J Cancer,* vol. 109, pp. 318-24, 2013.

[165] J. N. Poynter, S. B. Gruber, P. D. Higgins, R. Almog, J. D. Bonner, H. S. Rennert, M. Low, J. K. Greenson, and G. Rennert, "Statins and the risk of colorectal cancer," *N Engl J Med,* vol. 352, pp. 2184-92, 2005.

[166] R. J. Jacobs, P. W. Voorneveld, L. L. Kodach, and J. C. Hardwick, "Cholesterol metabolism and colorectal cancers," *Curr Opin Pharmacol,* vol. 12, pp. 690-5, 2012.

[167] V. Khurana, H. R. Bejjanki, G. Caldito, and M. W. Owens, "Statins reduce the risk of lung cancer in humans: a large case-control study of US veterans," *Chest,* vol. 131, pp. 1282-8, 2007.

[168] S. Suissa, S. Dell'aniello, S. Vahey, and C. Renoux, "Time-window bias in case-control studies: statins and lung cancer," *Epidemiology,* vol. 22, pp. 228-31, 2011.

[169] R. G. Elmore, Y. Ioffe, D. R. Scoles, B. Y. Karlan, and A. J. Li, "Impact of statin therapy on survival in epithelial ovarian cancer," *Gynecol Oncol,* vol. 111, pp. 102-105, 2008.

[170] T. Y. Chang, C. C. Y. Chang, N. Ohgami, and Y. Yamauchi, "Cholesterol sensing, trafficking, and esterification," *Annu. Rev. Cell. Dev. Biol.,* vol. 22, pp. 129-157, 2006.

[171] O. Larsson, "HMG-CoA reductase inhibitors: role in normal and malignant cells," *Crit Rev Oncol Hematol,* vol. 22, pp. 197-212, 1996.

[172] H. Y. Li, F. R. Appelbaum, C. L. Willman, R. A. Zager, and D. E. Banker, "Cholesterol-modulating agents kill acute myeloid leukemia cells and sensitize them to therapeutics by blocking adaptive cholesterol responses," *Blood,* vol. 101, pp. 3628-34, 2003.

[173] J. W. Clendening, A. Pandyra, P. C. Boutros, S. El Ghamrasni, F. Khosravi, G. A. Trentin, A. Martirosyan, A. Hakem, R. Hakem, I. Jurisica, and L. Z. Penn, "Dysregulation of the mevalonate pathway promotes transformation," *Proc Natl Acad Sci U S A,* vol. 107, pp. 15051-6, 2010.

[174] C. Ginestier, F. Monville, J. Wicinski, O. Cabaud, N. Cervera, E. Josselin, P. Finetti, A. Guille, G. Larderet, P. Viens, S. Sebti, F. Bertucci, D. Birnbaum, and E. Charafe-Jauffret, "Mevalonate metabolism regulates Basal breast cancer stem cells and is a potential therapeutic target," *Stem Cells,* vol. 30, pp. 1327-37, 2012.

[175] Y. Chen and M. Hughes-Fulford, "Human prostate cancer cells lack feedback regulation of low-density lipoprotein receptor and its regulator, SREBP2," *Int. J. Cancer,* vol. 91, pp. 41-45, 2001.

[176] E. Thysell, I. Surowiec, E. Hornberg, S. Crnalic, A. Widmark, A. I. Johansson, P. Stattin, A. Bergh, T. Moritz, H. Antti, and P. Wikstrom, "Metabolomic characterization of human prostate cancer bone metastases reveals increased levels of cholesterol," *PLoS One,* vol. 5, p. e14175, 2010.

[177] C. Antalis, T. Arnold, T. Rasool, B. Lee, K. Buhman, and R. Siddiqui, "High ACAT1 expression in estrogen receptor negative basal-like breast cancer cells is associated with LDL-induced proliferation," *Breast Cancer Res. Treat.,* vol. 122, pp. 661-670, 2010.

[178] A. Stranzl, H. Schmidt, R. Winkler, and G. M. Kostner, "Low-density lipoprotein receptor mRNA in human breast cancer cells: influence by PKC modulators," *Breast Cancer Res Treat,* vol. 42, pp. 195-205, 1997.

[179] D. Guo, F. Reinitz, M. Youssef, C. Hong, D. Nathanson, D. Akhavan, D. Kuga, A. N. Amzajerdi, H. Soto, S. Zhu, I. Babic, K. Tanaka, J. Dang, A. Iwanami, B. Gini, J. DeJesus, D. D. Lisiero, T. T. Huang, R. M. Prins, P. Y. Wen, H. I. Robins, M. D. Prados, L. M. DeAngelis, I. K. Mellinghoff, M. P. Mehta, C. D. James, A. Chakravarti, T. F. Cloughesy, P. Tontonoz, and P. S. Mischel, "An LXR agonist promotes glioblastoma cell death through inhibition of an EGFR/AKT/SREBP-1/LDLR-dependent pathway," *Cancer Discov.*, vol. 1, pp. 442-56, September 15, 2011 2011.

[180] B. H. Lee, M. G. Taylor, P. Robinet, J. D. Smith, J. Schweitzer, E. Sehayek, S. M. Falzarano, C. Magi-Galluzzi, E. A. Klein, and A. H. Ting, "Dysregulation of cholesterol homeostasis in human prostate cancer through loss of ABCA1," *Cancer Res*, vol. 73, pp. 1211-8, 2013.

[181] W. Shao and P. J. Espenshade, "Expanding roles for SREBP in metabolism," *Cell Metab.*, vol. 16, pp. 414-419, 2012.

[182] P. Tontonoz, "Transcriptional and posttranscriptional control of cholesterol homeostasis by liver X receptors," *Cold Spring Harb Symp Quant Biol*, vol. 76, pp. 129-37, 2011.

[183] S. L. Ettinger, R. Sobel, T. G. Whitmore, M. Akbari, D. R. Bradley, M. E. Gleave, and C. C. Nelson, "Dysregulation of sterol response element-binding proteins and downstream effectors in prostate cancer during progression to androgen independence," *Cancer Res.*, vol. 64, pp. 2212-2221, 2004.

[184] C. P. Chuu, R. A. Hiipakka, J. M. Kokontis, J. Fukuchi, R. Y. Chen, and S. Liao, "Inhibition of tumor growth and progression of LNCaP prostate cancer cells in athymic mice by androgen and liver X receptor agonist," *Cancer Res*, vol. 66, pp. 6482-6, 2006.

[185] J. D. Debes and D. J. Tindall, "Mechanisms of androgen-refractory prostate cancer," *N. Engl. J. Med.*, vol. 351, pp. 1488-1490, 2004.

[186] J. A. Locke, E. S. Guns, A. A. Lubik, H. H. Adomat, S. C. Hendy, C. A. Wood, S. L. Ettinger, M. E. Gleave, and C. C. Nelson, "Androgen levels increase by intratumoral de novo steroidogenesis during progression of castration-resistant prostate cancer," *Cancer Res*, vol. 68, pp. 6407-15, 2008.

[187] P. R. Dillard, M. F. Lin, and S. A. Khan, "Androgen-independent prostate cancer cells acquire the complete steroidogenic potential of synthesizing testosterone from cholesterol," *Mol Cell Endocrinol*, vol. 295, pp. 115-20, 2008.

[188] R. B. Montgomery, E. A. Mostaghel, R. Vessella, D. L. Hess, T. F. Kalhorn, C. S. Higano, L. D. True, and P. S. Nelson, "Maintenance of intratumoral androgens in metastatic prostate cancer: a mechanism for castration-resistant tumor growth," *Cancer Res*, vol. 68, pp. 4447-54, 2008.

[189] C. G. Leon, J. A. Locke, H. H. Adomat, S. L. Etinger, A. L. Twiddy, R. D. Neumann, C. C. Nelson, E. S. Guns, and K. M. Wasan, "Alterations in cholesterol regulation contribute to the production of intratumoral androgens during progression to castration-resistant prostate cancer in a mouse xenograft model," *Prostate*, vol. 70, pp. 390-400, 2010.

[190] A. L. Twiddy, C. G. Leon, and K. M. Wasan, "Cholesterol as a potential target for castration-resistant prostate cancer," *Pharm Res*, vol. 28, pp. 423-37, 2011.

[191] K. Simons and D. Toomre, "Lipid rafts and signal transduction," *Nat Rev Mol Cell Biol,* vol. 1, pp. 31-39, 2000.

[192] V. Michel and M. Bakovic, "Lipid rafts in health and disease," *Biol Cell,* vol. 99, pp. 129-140, 2007.

[193] M. H. Hager, K. R. Solomon, and M. R. Freeman, "The role of cholesterol in prostate cancer.," *Curr. Opin. Clin. Nutr. Metab. Care,* vol. 9, pp. 379-385, 2006.

[194] J. A. Karam, Y. Lotan, C. G. Roehrborn, R. Ashfaq, P. I. Karakiewicz, and S. F. Shariat, "Caveolin-1 overexpression is associated with aggressive prostate cancer recurrence," *The Prostate,* vol. 67, pp. 614-622, 2007.

[195] T. M. Williams and M. P. Lisanti, "Caveolin-1 in oncogenic transformation, cancer, and metastasis," *Am J Physiol-Cell Ph,* vol. 288, pp. C494-C506, 2005.

[196] E. K. Sloan, K. L. Stanley, and R. L. Anderson, "Caveolin-1 inhibits breast cancer growth and metastasis," *Oncogene,* vol. 23, pp. 7893-7897, 2004.

[197] M. F. Mulas, C. Abete, D. Pulisci, A. Pani, B. Massidda, S. Dessì, and A. Mandas, "Cholesterol esters as growth regulators of lymphocytic leukaemia cells," *Cell Prolif.,* vol. 44, pp. 360-371, 2011.

[198] B. Batetta, A. Pani, M. Putzolu, F. Sanna, R. Bonatesta, S. Piras, O. Spano, M. F. Mulas, and S. Dessi, "Correlation between cholesterol esterification, MDR1 gene expression and rate of cell proliferation in CEM and MOLT4 cell lines," *Cell Prolif,* vol. 32, pp. 49-61, 1999.

[199] S. Dessi, B. Batetta, A. Pani, O. Spano, F. Sanna, M. Putzolu, R. Bonatesta, S. Piras, and P. Pani, "Role of cholesterol synthesis and esterification in the growth of CEM and MOLT4 lymphoblastic cells," *Biochem J,* vol. 321 (Pt 3), pp. 603-8, 1997.

[200] A. Pani and S. Dessì, "Cell Growth and Cholesterol Esters," Georgetown, TX; New York, NY: Landes Bioscience; Kluwer Academic/Plenum Publishers, 2003.

[201] M. R. Tosi and V. Tugnoli, "Cholesteryl esters in malignancy," *Clin Chim Acta,* vol. 359, pp. 27-45, 2005.

[202] C. Nygren, H. von Holst, J. E. Mansson, and P. Fredman, "Increased levels of cholesterol esters in glioma tissue and surrounding areas of human brain," *Br J Neurosurg,* vol. 11, pp. 216-20, 1997.

[203] A. Subramanian, B. Shankar Joshi, A. D. Roy, R. Roy, V. Gupta, and R. S. Dang, "NMR spectroscopic identification of cholesterol esters, plasmalogen and phenolic glycolipids as fingerprint markers of human intracranial tuberculomas," *NMR Biomed,* vol. 21, pp. 272-88, 2008.

[204] J. H. Pinthus, K. F. Whelan, D. Gallino, J. P. Lu, and N. Rothschild, "Metabolic features of clear-cell renal cell carcinoma: mechanisms and clinical implications," *Can Urol Assoc J,* vol. 5, pp. 274-82, 2011.

[205] H. A. Drabkin and R. M. Gemmill, "Cholesterol and the development of clear-cell renal carcinoma," *Curr Opin Pharmacol,* vol. 12, pp. 742-50, 2012.

[206] R. L. Gebhard, R. V. Clayman, W. F. Prigge, R. Figenshau, N. A. Staley, C. Reesey, and A. Bear, "Abnormal cholesterol metabolism in renal clear cell carcinoma," *J Lipid Res,* vol. 28, pp. 1177-84, 1987.

[207] P. M. Cruz, H. Mo, W. J. McConathy, N. Sabnis, and A. G. Lacko, "The role of cholesterol metabolism and cholesterol transport in carcinogenesis: a review of scientific findings, relevant to future cancer therapeutics," *Front Pharmacol,* vol. 4, p. 119, 2013.

[208] J. R. Krycer and A. J. Brown, "Cholesterol accumulation in prostate cancer: a classic observation from a modern perspective," *Biochim Biophys Acta,* vol. 1835, pp. 219-29, 2013.

[209] S. Silvente-Poirot and M. Poirot, "Cholesterol metabolism and cancer: the good, the bad and the ugly," *Curr Opin Pharmacol,* vol. 12, pp. 673-6, 2012.

[210] C. J. Antalis and K. K. Buhman, "Lipoproteins and Cancer," in *Lipoproteins - Role in Health and Diseases*, G. Kostner, Ed.: InTech, 2012.

[211] C. Danilo and P. G. Frank, "Cholesterol and breast cancer development," *Curr Opin Pharmacol,* vol. 12, pp. 677-82, 2012.

[212] J. M. Wiseman, D. R. Ifa, A. Venter, and R. G. Cooks, "Ambient molecular imaging by desorption electrospray ionization mass spectrometry," *Nat Protoc,* vol. 3, pp. 517-524, 2008.

[213] J. Griffiths, "Raman spectroscopy for medical diagnosis," *Anal Chem,* vol. 79, pp. 3975-3978, 2007.

[214] D. I. Ellis and R. Goodacre, "Metabolic fingerprinting in disease diagnosis: biomedical applications of infrared and Raman spectroscopy," *Analyst,* vol. 131, pp. 875-885, 2006.

[215] D. Naumann, "FT-infrared and FT-Raman spectroscopy in biomedical research," *App Spectrosc Rev,* vol. 36, pp. 239-298, 2001.

[216] M. J. Bissell and D. Radisky, "Putting tumours in context," *Nat Rev Cancer,* vol. 1, pp. 46-54, 2001.

[217] S. H. Yue, M. N. Slipchenko, and J.-X. Cheng, "Multimodal nonlinear optical microscopy," *Laser Photon. Rev.,* vol. 5, pp. 496-512, Jul 2011.

[218] J.-X. Cheng, Y. K. Jia, G. Zheng, and X. S. Xie, "Laser-scanning coherent anti-stokes raman scattering microscopy and applications to cell biology," *Biophys. J* . vol. 83, pp. 502–509, 2002.

[219] J.-X. Cheng and X. S. Xie, "Coherent anti-Stokes Raman scattering microscopy: instrumentation, theory, and applications," *J. Phys. Chem. B,* vol. 108, pp. 827-840, 2004.

[220] T. T. Le, H. M. Duren, M. N. Slipchenko, C.-D. Hu, and J.-X. Cheng, "Label-free quantitative analysis of lipid metabolism in living caenorhabditis elegans," *J. Lipid Res.,* p. jlr.D000638, September 23, 2009 2009.

[221] T. T. Le, C. W. Rehrer, T. B. Huff, M. B. Nichols, I. G. Camarillo, and J.-X. Cheng, "Nonlinear optical imaging to evaluate the impact of obesity on mammary gland and tumor stroma," *Molecular Imaging,* vol. 6, pp. 205–211, 2007.

[222] H. Wang, Y. Fu, P. Zickmund, R. Shi, and J.-X. Cheng, "Coherent anti-Stokes Raman scattering imaging of axonal myelin in live spinal tissues," *Biophys. J* . vol. 89, pp. 581-591, 2005.

[223] H. Wang, Y. Fu, and J. X. Cheng, "Experimental observation and theoretical analysis of Raman resonance-enhanced photodamage in coherent anti-Stokes Raman scattering microscopy," *J. Opt. Soc. Am. B,* vol. 24, pp. 544-552, 2007.

[224] Y. Ozeki, F. Dake, S. i. Kajiyama, K. Fukui, and K. Itoh, "Analysis and experimental assessment of the sensitivity of stimulated Raman scattering microscopy," *Opt. Express,* vol. 17, pp. 3651-3658, 2009.

[225] P. Nandakumar, A. Kovalev, and A. Volkmer, "Vibrational imaging based on stimulated Raman scattering microscopy," *New J. Phys.,* vol. 11, p. 033026, 2009.

[226] C. W. Freudiger, W. Min, B. G. Saar, S. Lu, G. R. Holtom, C. He, J. C. Tsai, J. X. Kang, and X. S. Xie, "Label-free biomedical imaging with high sensitivity by stimulated Raman scattering microscopy," *Science,* vol. 322, pp. 1857-61, 2008.

[227] P. Nandakumar, A. Kovalev, A. Muschielok, and A. Volkmer, "Vibrational imaging and microspectroscopies based on coherent anti-Stokes Raman scattering microscopy," *the 8th European/French Israeli Symposium on Nonlinear and Quantum Optics, Mo-B,* 2005.

[228] E. Ploetz, S. Laimgruber, S. Berner, W. Zinth, and P. Gilch, "Femtosecond stimulated Raman microscopy," *Appl. Phys. B,* vol. 87, pp. 389-393, 2007.

[229] B. G. Saar, C. W. Freudiger, J. Reichman, C. M. Stanley, G. R. Holtom, and X. S. Xie, "Video-rate molecular imaging in vivo with stimulated Raman scattering," *Science,* vol. 330, pp. 1368-1370, December 3, 2010 2010.

[230] M. N. Slipchenko, H. Chen, D. R. Ely, Y. Jung, M. T. Carvajal, and J. X. Cheng, "Vibrational imaging of tablets by epi-detected stimulated Raman scattering microscopy," *Analyst,* vol. 135, pp. 2613-2619, 2010.

[231] B. G. Saar, Y. N. Zeng, C. W. Freudiger, Y. S. Liu, M. E. Himmel, X. S. Xie, and S. Y. Ding, "Label-free, real-time monitoring of biomass processing with stimulated Raman scattering microscopy," *Angew. Chem. Int. Ed.,* vol. 49, pp. 5476-5479, 2010.

[232] M. N. Slipchenko, T. T. Le, H. T. Chen, and J. X. Cheng, "High-Speed Vibrational Imaging and Spectral Analysis of Lipid Bodies by Compound Raman Microscopy," *J Phys Chem B,* vol. 113, pp. 7681-7686, May 2009.

[233] M. N. Slipchenko, T. T. Le, H. T. Chen, and J. X. Cheng, "High-Speed Vibrational Imaging and Spectral Analysis of Lipid Bodies by Compound Raman Microscopy," *Journal of Physical Chemistry B,* vol. 113, pp. 7681-7686, May 2009.

[234] T. Migita, S. Ruiz, A. Fornari, M. Fiorentino, C. Priolo, G. Zadra, F. Inazuka, C. Grisanzio, E. Palescandolo, and e. a. E. Shin "Fatty acid synthase: a metabolic enzyme and candidate oncogene in prostate cancer," *J. Natl. Cancer Inst.,* vol. 101, pp. 519-532, 2009.

[235] J.-X. Cheng and X. S. Xie, *Coherent Raman Scattering Microscopy* vol. 1. Boca Raton, Florida: CRC Press, 2012.

[236] T. T. Le, S. Yue, and J.-X. Cheng, "Shedding new light on lipid biology with CARS microscopy," *J. Lipid Res.,* vol. 51, pp. 3091-102, 2010.

[237] X. Nan, E. O. Potma, and X. S. Xie, "Nonperturbative chemical imaging of organelle transport in living cells with coherent anti-Stokes Raman scattering microscopy," *Biophys. J.,* vol. 91, pp. 728-735, 2006.

[238] T. Hellerer, C. Axäng, C. Brackmann, P. Hillertz, M. Pilon, and A. Enejder, "Monitoring of lipid storage in Caenorhabditis elegans using coherent anti-Stokes Raman scattering (CARS) microscopy," *Proc. Natl. Acad. Sci. U.S.A.* , vol. 104, pp. 14658-14663, 2007.

[239] R. K. Lyn, D. C. Kennedy, A. Stolow, A. Ridsdale, and J. P. Pezacki, "Dynamics of lipid droplets induced by the hepatitis C virus core protein," *Biochem. Biophys. Res. Commun.*, vol. 399, pp. 518-524, 2010.

[240] M. Paar, C. Jüngst, N. A. Steiner, C. Magnes, F. Sinner, D. Kolb, A. Lass, R. Zimmermann, A. Zumbusch, S. D. Kohlwein, and H. Wolinski, "Remodeling of lipid droplets during lipolysis and growth in adipocytes," *J. Biol. Chem.*, vol. 287, pp. 11164-11173, 2012.

[241] W. Dou, D. Zhang, Y. Jung, J.-X. Cheng, and D. M. Umulis, "Label-free imaging of lipid-droplet intracellular motion in early Drosophila embryos using femtosecond-stimulated Raman loss microscopy," *Biophys. J.*, vol. 102, pp. 1666-1675, 2012.

[242] H. A. Rinia, K. N. J. Burger, M. Bonn, and M. Müller, "Quantitative label-free imaging of lipid composition and packing of individual cellular lipid droplets using multiplex CARS microscopy," *Biophys. J.*, vol. 95, pp. 4908-4914, 2008.

[243] M. N. Slipchenko, T. T. Le, H. T. Chen, and J.-X. Cheng, "High-speed vibrational imaging and spectral analysis of lipid bodies by compound Raman microscopy," *J. Phys. Chem. B*, vol. 113, pp. 7681-7686, 2009.

[244] T. Igawa, F. F. Lin, M. S. Lee, D. Karan, S. K. Batra, and M. F. Lin, "Establishment and characterization of androgen-independent human prostate cancer LNCaP cell model," *Prostate*, vol. 50, pp. 222-235, 2002.

[245] H. K. Lin, Y. C. Hu, L. Yang, S. Altuwaijri, Y. T. Chen, H. Y. Kang, and C. S. Chang, "Suppression versus induction of androgen receptor functions by the phosphatidylinositol 3-kinase/Akt pathway in prostate cancer LNCaP cells with different passage numbers," *J. Biol. Chem.*, vol. 278, pp. 50902-50907, 2003.

[246] E. Unni, S. H. Sun, B. C. Nan, M. J. McPhaul, B. Cheskis, M. A. Mancini, and M. Marcelli, "Changes in androgen receptor nongenotropic signaling correlate with transition of LNCaP cells to androgen independence," *Cancer Res.*, vol. 64, pp. 7156-7168, 2004.

[247] Y. H. Youm, S. Kim, Y. Y. Bahk, and T. K. Yoo, "Proteomic analysis of androgen-independent growth in low and high passage human LNCaP prostatic adenocarcinoma cells," *BMB Rep.*, vol. 41, pp. 722-727, 2008.

[248] D. Zhang, M. N. Slipchenko, and J.-X. Cheng, "Highly sensitive vibrational imaging by femtosecond pulse stimulated Raman loss," *J. Phys. Chem. Lett.*, vol. 2, pp. 1248-1253, 2011.

[249] P. C. de Smidt and T. J. C. van Berkel, "Prolonged serum half-life of antineoplastic drugs by incorporation into the low density lipoprotein," *Cancer Res.*, vol. 50, pp. 7476-7482, 1990.

[250] J. Folch, M. Lees, and G. H. S. Stanley, "A simple method for the isolation and purification of total lipids from animal tissues," *J. Biol. Chem.*, vol. 226, pp. 497-509, 1957.

[251] G. Liebisch, M. Binder, R. Schifferer, T. Langmann, B. Schulz, and G. Schmitz, "High throughput quantification of cholesterol and cholesteryl ester by electrospray ionization tandem mass spectrometry (ESI-MS/MS)," *Biochim Biophys Acta.*, vol. 1761, pp. 121-128, 2006.

[252] W.-C. Yang, J. Adamec, and F. E. Regnier, "Enhancement of the LC/MS analysis of fatty acids through derivatization and stable isotope coding," *Anal. Chem.*, vol. 79, pp. 5150-5157, 2007.

[253] G. Zhao, A. J. Souers, M. Voorbach, H. D. Falls, B. Droz, S. Brodjian, Y. Y. Lau, R. R. Iyengar, J. Gao, A. S. Judd, S. H. Wagaw, M. M. Ravn, K. M. Engstrom, J. K. Lynch, M. M. Mulhern, J. Freeman, B. D. Dayton, X. Wang, N. Grihalde, D. Fry, D. W. A. Beno, K. C. Marsh, Z. Su, G. J. Diaz, C. A. Collins, H. Sham, R. M. Reilly, M. E. Brune, and P. R. Kym, "Validation of diacyl glycerolacyltransferase I as a novel target for the treatment of obesity and dyslipidemia using a potent and selective small molecule inhibitor," *J. Med. Chem.*, vol. 51, pp. 380-383, 2013/10/08 2008.

[254] A. Rodriguez and D. C. Usher, "Anti-atherogenic effects of the acyl-CoA:cholesterol acyltransferase inhibitor, avasimibe (CI-1011), in cultured primary human macrophages," *Atherosclerosis*, vol. 161, pp. 45-54, 2002.

[255] H. T. Lee, D. R. Sliskovic, J. A. Picard, B. D. Roth, W. Wierenga, J. L. Hicks, R. F. Bousley, K. L. Hamelehle, R. Homan, C. Speyer, R. L. Stanfield, and B. R. Krause, "Inhibitors of acyl-CoA:cholesterol O-acyl transferase (ACAT) as hypocholesterolemic agents. CI-1011: an acyl sulfamate with unique cholesterol-lowering activity in animals fed noncholesterol-supplemented diets," *J. Med. Chem.*, vol. 39, pp. 5031-5034, 2013/10/08 1996.

[256] G. Llaverías, J. C. Laguna, and M. Alegret, "Pharmacology of the ACAT inhibitor avasimibe (CI-1011)," *Cardiovasc. Drug Rev.*, vol. 21, pp. 33-50, 2003.

[257] R. J. Williams, A. D. McCarthy, and C. D. Sutherland, "Esterification and absorption of cholesterol: in vitro and in vivo observations in the rat," *Biochim. Biophys. Acta.*, vol. 1003, pp. 213-216, 1989.

[258] R. J. Ablin, P. Guinan, and I. M. Bush, "Lipofuscin granules in normal, benign and malignant human prostatic tissue," *Urol. Res.*, vol. 1, pp. 149-151, 1973.

[259] Z. Movasaghi, S. Rehman, and I. U. Rehman, "Raman spectroscopy of biological tissues," *Appl. Spectrosc. Rev.*, vol. 42, pp. 493-541, 2007.

[260] M. E. McMenamin, P. Soung, S. Perera, I. Kaplan, M. Loda, and W. R. Sellers, "Loss of PTEN expression in paraffin-embedded primary prostate cancer correlates with high Gleason score and advanced stage," *Cancer Res.*, vol. 59, pp. 4291-4296, 1999.

[261] I. Vivanco and C. L. Sawyers, "The phosphatidylinositol 3-Kinase-AKT pathway in human cancer," *Nat Rev Cancer*, vol. 2, pp. 489-501, 2002.

[262] D. Sarker, A. H. Reid, T. A. Yap, and J. S. de Bono, "Targeting the PI3K/AKT pathway for the treatment of prostate cancer," *Clin. Cancer Res.*, vol. 15, pp. 4799-805, 2009.

[263] A. J. R. Habenicht, P. Salbach, M. Goerig, W. Zeh, U. Janssen-Timmen, C. Blattner, W. C. King, and J. A. Glomset, "The LDL receptor pathway delivers arachidonic acid for eicosanoid formation in cells stimulated by platelet-derived growth factor," *Nature,* vol. 345, pp. 634-636, 1990.

[264] M. Hughes-Fulford, Y. F. Chen, and R. R. Tjandrawinata, "Fatty acid regulates gene expression and growth of human prostate cancer PC-3 cells," *Carcinogenesis,* vol. 22, pp. 701-707, 2001.

[265] J. Ghosh and C. E. Myers, "Arachidonic acid stimulates prostate cancer cell growth: critical role of 5-lipoxygenase," *Biochem. Biophys. Res. Commun.,* vol. 235, pp. 418-423, 1997.

[266] M. Hughes-Fulford, C.-F. Li, J. Boonyaratanakornkit, and S. Sayyah, "Arachidonic acid activates phosphatidylinositol 3-kinase signaling and induces gene expression in prostate cancer," *Cancer Res.,* vol. 66, pp. 1427-1433, 2006.

[267] D. J. Murphy, "The biogenesis and functions of lipid bodies in animals, plants and microorganisms," *Prog. Lipid Res.,* vol. 40, pp. 325–438, 2001.

[268] R. B. Shah, R. Mehra, A. M. Chinnaiyan, R. Shen, D. Ghosh, M. Zhou, G. R. MacVicar, S. Varambally, J. Harwood, T. A. Bismar, R. Kim, M. A. Rubin, and K. J. Pienta, "Androgen-independent prostate cancer is a heterogeneous group of diseases: Lessons from a rapid autopsy program," *Cancer Res.,* vol. 64, pp. 9209-9216, 2004.

[269] N. Chalhoub and S. J. Baker, "PTEN and the PI3-kinase pathway in cancer," *Annu. Rev.Pathol.,* vol. 4, pp. 127-50, 2009.

[270] D. J. Mulholland, L. M. Tran, Y. Li, H. Cai, A. Morim, S. Wang, S. Plaisier, I. P. Garraway, J. Huang, and T. G. Graeber, "Cell autonomous role of PTEN in regulating castration-resistant prostate cancer growth," *Cancer Cell,* vol. 19, pp. 792-804, 2011.

[271] X. S. Liu, B. Song, B. D. Elzey, T. L. Ratliff, S. F. Konieczny, L. Cheng, N. Ahmad, and X. Liu, "Polo-like kinase 1 facilitates loss of PTEN tumor suppressor-induced prostate cancer formation," *J. Biol. Chem.,* vol. 286, pp. 35795-35800, October 14, 2011 2011.

[272] G. Swyer, "The cholesterol content of normal and enlarged prostates," *Cancer Res.,* vol. 2, pp. 372-375, 1942.

[273] E. A. Platz, M. F. Leitzmann, K. Fisvanathan, E. B. Rimm, M. J. Stampfer, W. C. Willett, and E. Giovannucci, "Statin drugs and risk of advanced prostate cancer," *J Nat Cancer Inst,* vol. 98, pp. 1819-1825, 2006.

[274] T. J. Murtola, H. Syvälä, P. Pennanen, M. Bläuer, T. Solakivi, T. Ylikomi, and T. L. J. Tammela, "Comparative effects of high and low-dose simvastatin on prostate epithelial cells: the role of LDL," *Eur J Pharmacol,* vol. 673, pp. 96-100, 2011.

[275] R. Siegel, D. Naishadham, and A. Jemal, "Cancer statistics, 2012," *CA Cancer J. Clin.,* vol. 62, pp. 10-29, 2012.

[276] F. H. Schröder, J. Hugosson, M. J. Roobol, T. L. J. Tammela, S. Ciatto, V. Nelen, M. Kwiatkowski, M. Lujan, H. Lilja, M. Zappa, L. J. Denis, F. Recker, A. Berenguer, L. Määttänen, C. H. Bangma, G. Aus, A. Villers, X. Rebillard, T. van der Kwast, B. G. Blijenberg, S. M. Moss, H. J. de Koning, and A. Auvinen, "Screening and prostate-cancer mortality in a randomized European study," *N. Engl. J. Med.,* vol. 360, pp. 1320-1328, 2009.

[277] L. Cheng and D. G. Bostwick, "Neoplasms of the prostate," in *Essentials of Anatomic Pathology* Totowa, New Jersey: Humana Press, 2002.

[278] J. S. de Bono, C. J. Logothetis, A. Molina, K. Fizazi, S. North, L. Chu, K. N. Chi, R. J. Jones, O. B. Goodman, F. Saad, J. N. Staffurth, P. Mainwaring, S. Harland, T. W. Flaig, T. E. Hutson, T. Cheng, H. Patterson, J. D. Hainsworth, C. J. Ryan, C. N. Sternberg, S. L. Ellard, A. Fléchon, M. Saleh, M. Scholz, E. Efstathiou, A. Zivi, D. Bianchini, Y. Loriot, N. Chieffo, T. Kheoh, C. M. Haqq, and H. I. Scher, "Abiraterone and increased survival in metastatic prostate cancer," *N. Engl. J. Med.,* vol. 364, pp. 1995-2005, 2011.

[279] S. Bemlih, M.-D. Poirier, and A. E. Andaloussi, "Acyl-coenzyme A: Cholesterol acyltransferase inhibitor Avasimibe affect survival and proliferation of glioma tumor cell lines," *Cancer Biol. Ther.,* vol. 9, pp. 1025-1032, 2010.

[280] C. Antalis, T. Arnold, T. Rasool, B. Lee, K. Buhman, and R. Siddiqui, "High ACAT1 expression in estrogen receptor negative basal-like breast cancer cells is associated with LDL-induced proliferation," *Breast Cancer Res. Treat.,* vol. 122, pp. 661-670, 2009.

[281] S. Yue, J. M. Cárdenas-Mora, L. S. Chaboub, S. A. Lelièvre, and J.-X. Cheng, "Label-free analysis of breast tissue polarity by Raman imaging of lipid phase," *Biophys. J.,* vol. 102, pp. 1215-1223, 2012.

[282] L. E. O'Brien, M. M. P. Zegers, and K. E. Mostov, "Building epithelial architecture: insights from three-dimensional culture models," *Nat Rev Mol Cell Biol,* vol. 3, pp. 531-537, 2002.

[283] F. Pampaloni, E. G. Reynaud, and E. H. K. Stelzer, "The third dimension bridges the gap between cell culture and live tissue," *Nat Rev Mol Cell Biol,* vol. 8, pp. 839-845, 2007.

[284] K. M. Yamada and E. Cukierman, "Modeling tissue morphogenesis and cancer in 3D," *Cell,* vol. 130, pp. 601-610, 2007.

[285] V. M. Weaver, O. W. Petersen, F. Wang, C. A. Larabell, P. Briand, C. Damsky, and M. J. Bissell, "Reversion of the malignant phenotype of human breast cells in three-dimensional culture and in vivo by integrin blocking antibodies," *J Cell Biol.,* vol. 137, pp. 231-245, 1997.

[286] S. A. Lelievre, V. M. Weaver, J. A. Nickerson, C. A. Larabell, A. Bhaumik, O. W. Petersen, and M. J. Bissell, "Tissue phenotype depends on reciprocal interactions between the extracellular matrix and the structural organization of the nucleus," *P Natl Acad Sci USA,* vol. 95, pp. 14711-14716, 1998.

[287] M. J. Bissell, D. C. Radisky, A. Rizki, V. M. Weaver, and O. W. Petersen, "The organizing principle: microenvironmental influences in the normal and malignant breast," *Differentiation,* vol. 70, pp. 537–546, 2002.

[288] V. M. Weaver, S. Lelievre, J. N. Lakins, M. A. Chrenek, J. C. R. Jones, F. Giancotti, Z. Werb, and M. J. Bissell, "beta 4 integrin-dependent formation of polarized three-dimensional architecture confers resistance to apoptosis in normal and malignant mammary epithelium," *Cancer Cell*, vol. 2, pp. 205-216, 2002.

[289] M. J. Bissell, A. Rizki, and S. Mian, "Tissue architecture: the ultimate regulator of breast epithelial function," *Current Opinion in Cell Biology* vol. 15, pp. 753–762, 2003.

[290] C. M. Nelson and M. J. Bissell, "Modeling dynamic reciprocity: Engineering three-dimensional culture models of breast architecture, function, and neoplastic transformation," *Semin. Cancer Biol.*, vol. 15, pp. 342-352, 2005.

[291] J. Debnath and J. S. Brugge, "Modelling glandular epithelial cancers in three-dimensional cultures," *Nat Rev Cancer*, vol. 5, pp. 675-688, 2005.

[292] H. A. Adissu, E. K. Asem, and S. A. Lelièvre, "Three-dimensional cell culture to model epithelia in the female reproductive system," *Reprod. Sci.*, vol. 14, pp. 11-19, 2007.

[293] G. Chandramouly, P. C. Abad, D. W. Knowles, and S. A. Lelièvre, "The control of tissue architecture over nuclear organization is crucial for epithelial cell fate," *J Cell Sci*, vol. 120, pp. 1596-1606, 2007.

[294] P. C. Abad, J. Lewis, I. S. Mian, D. W. Knowles, J. Sturgis, S. Badve, J. Xie, and S. A. Lelievre, "NuMA influences higher order chromatin organization in human mammary epithelium," *Mol. Biol. Cell*, vol. 18, pp. 348-361, 2007.

[295] S. A. Lelievre, "Tissue Polarity-Dependent Control of Mammary Epithelial Homeostasis and Cancer Development: an Epigenetic Perspective," *J. Mammary Gland Biol. Neoplasia*, vol. 15, pp. 49-63, Mar 2010.

[296] G. Y. Lee, P. A. Kenny, E. H. Lee, and M. J. Bissell, "Three-dimensional culture models of normal and malignant breast epithelial cells," *Nat Methods*, vol. 4, pp. 359 - 365, 2007.

[297] L. Hilakivi-Clarke, E. Cho, M. Raygada, and N. Kenney, "Alterations in mammary gland development following neonatal exposure to estradiol, transforming growth factor alpha, and estrogen receptor antagonist ICI 182,780," *J Cell Physiol*, vol. 170, pp. 279-289, 1997.

[298] L. K. Olson, Y. Tan, Y. Zhao, M. D. Aupperlee, and S. Z. Haslam, "Pubertal exposure to high fat diet causes mouse strain-dependent alterations in mammary gland development and estrogen responsiveness," *Int J Obesity*, vol. 34, pp. 1415-1426, 2010.

[299] C. M. Vachon, C. C. Kuni, K. Anderson, V. E. Anderson, and T. A. Sellers, "Association of mammographically defined percent breast density with epidemiologic risk factors for breast cancer (United States)," *Cancer Causes Control*, vol. 11, pp. 653-662, 2000.

[300] E. M. Fish and B. A. Molitoris, "Alterations in Epithelial Polarity and the Pathogenesis of Disease States," *New England Journal of Medicine*, vol. 330, pp. 1580-1588, Jun 1994.

[301] E. Rodriguez-Boulan and W. J. Nelson, "Morphogenesis of the polarized epithelial cell phenotype," *Science*, vol. 245, pp. 718-725, 1989.

[302] I. Mellman and W. J. Nelson, "Coordinated protein sorting, targeting and distribution in polarized cells," *Nature Reviews Molecular Cell Biology,* vol. 9, pp. 833-845, Nov 2008.

[303] S. Schuck and K. Simons, "Polarized sorting in epithelial cells: raft clustering and the biogenesis of the apical membrane," *J Cell Sci,* vol. 117, pp. 5955-5964, 2004.

[304] K. Simons and G. Vanmeer, "Lipid Sorting in Epithelial Cells," *Biochemistry,* vol. 27, pp. 6197-6202, Aug 1988.

[305] S. Tsukita, M. Furuse, and M. Itoh, "Multifunctional strands in tight junctions," *Nature Reviews Molecular Cell Biology,* vol. 2, pp. 285-293, Apr 2001.

[306] D. M. Bryant and K. E. Mostov, "From cells to organs: building polarized tissue," *Nature Reviews Molecular Cell Biology,* vol. 9, pp. 887-901, Nov 2008.

[307] M. Furuse, "Molecular Basis of the Core Structure of Tight Junctions " *Cold Spring Harb Perspect Biol,* vol. 2, p. a002907, 2010.

[308] L. L. Mitic and J. M. Anderson, "Molecular Architecture of Tight Junctions," *Annu. Rev. Physiol.,* vol. 60, pp. 121-142, 1998.

[309] M. Cereijido, J. Valdes, L. Shoshani, and R. G. Contreras, "Role of tight junctions in establishing and maintaining cell polarity," *Annual Review of Physiology,* vol. 60, pp. 161-177, 1998.

[310] K. Matter, S. Aijaz, A. Tsapara, and M. S. Balda, "Mammalian tight junctions in the regulation of epithelial differentiation and proliferation," *Curr Opin Cell Biol,* vol. 17, pp. 453-458, 2005.

[311] K. Matter and M. S. Balda, "Epithelial tight junctions, gene expression and nucleo-junctional interplay," *Journal of Cell Science,* vol. 120, pp. 1505-1511, May 2007.

[312] L. Zhan, A. Rosenberg, K. C. Bergami, M. Yu, Z. Xuan, A. B. Jaffe, C. Allred, and S. K. Muthuswamy, "Deregulation of Scribble Promotes Mammary Tumorigenesis and Reveals a Role for Cell Polarity in Carcinoma," *Cell,* vol. 135, pp. 865-878, 2008.

[313] C. Plachot, L. Chaboub, H. Adissu, L. Wang, A. Urazaev, J. Sturgis, E. Asem, and S. Lelievre, "Factors necessary to produce basoapical polarity in human glandular epithelium formed in conventional and high-throughput three-dimensional culture: example of the breast epithelium," *BMC Biol.,* vol. 7, p. 77, 2009.

[314] R. Shaykhiev, F. Otaki, P. Bonsu, D. Dang, M. Teater, Y. Strulovici-Barel, J. Salit, B.-G. Harvey, and R. Crystal, "Cigarette smoking reprograms apical junctional complex molecular architecture in the human airway epithelium in vivo," *Cellular and Molecular Life Sciences,* vol. 68, pp. 877-892, 2010.

[315] C. Plachot and S. A. Lelievre, "DNA methylation control of tissue polarity and cellular differentiation in the mammary epithelium," *Exp Cell Res,* vol. 298, pp. 122-132, 2004.

[316] D. F. H. Wallach, S. P. Verma, and J. Fookson, "Application of Laser Raman and Infrared Spectroscopy to the Analysis of Membrane-Structure," *Biochimica Et Biophysica Acta,* vol. 559, pp. 153-208, 1979.

[317] J. J. Duindam, G. Vrensen, C. Otto, and J. Greve, "Cholesterol, phospholipid, and protein changes in focal opacities in the human eye lens," *Invest Ophthalmol Vis Sci,* vol. 39, pp. 94-103, Jan 1998.

[318] M. Gniadecka, O. F. Nielsen, D. H. Christensen, and H. C. Wulf, "Structure of Water, Proteins, and Lipids in Intact Human Skin, Hair, and Nail," *J Invest Dermatol,* vol. 110, pp. 393-398, 1998.

[319] H.-U. Gremlich and B. Yan, *Infrared and Raman spectroscopy of biological materials*. New York: Marcel Dekker, 2001.

[320] M. Pezolet and D. Georgescauld, "Raman spectroscopy of nerve fibers," *Biophys J,* vol. 47, pp. 367-372, 1985.

[321] G. J. Puppels, F. F. M. de Mul, C. Otto, J. Greve, M. Robert-Nicoud, D. J. Arndt-Jovin, and T. M. Jovin, "Studying single living cells and chromosomes by confocal Raman microspectroscopy," *Nature,* vol. 347, pp. 301-303, 1990.

[322] Y.-S. Huang, T. Karashima, M. Yamamoto, and H.-o. Hamaguchi, "Molecular-Level Investigation of the Structure, Transformation, and Bioactivity of Single Living Fission Yeast Cells by Time- and Space-Resolved Raman Spectroscopy," *Biochemistry,* vol. 44, pp. 10009-10019, 2011/12/21 2005.

[323] K. W. Short, S. Carpenter, J. P. Freyer, and J. R. Mourant, "Raman spectroscopy detects biochemical changes due to proliferation in mammalian cell cultures," *Biophys J,* vol. 88, pp. 4274-4288, Jun 2005.

[324] H.-J. van Manen, Y. M. Kraan, D. Roos, and C. Otto, "Single-cell Raman and fluorescence microscopy reveal the association of lipid bodies with phagosomes in leukocytes," *Proc Natl Acad Sci U S A,* vol. 102, pp. 10159-10164, July 19, 2005 2005.

[325] J.-X. Cheng and X. S. Xie, "Coherent anti-Stokes Raman scattering microscopy: instrumentation, theory, and applications," *J Phys Chem B,* vol. 108, pp. 827-840, 2004.

[326] J.-X. Cheng, Y. K. Jia, G. Zheng, and X. S. Xie, "Laser-scanning coherent anti-stokes Raman scattering microscopy and applications to cell biology," *Biophys. J.,* vol. 83, pp. 502–509, 2002.

[327] H. Wang, Y. Fu, P. Zickmund, R. Shi, and J.-X. Cheng, "Coherent anti-Stokes Raman scattering imaging of axonal myelin in live spinal tissues," *Biophys. J.,* vol. 89, pp. 581-591, 2005.

[328] T. T. Le and J.-X. Cheng, "Single-Cell Profiling Reveals the Origin of Phenotypic Variability in Adipogenesis," *PLoS One,* vol. 4, p. e5189, 2009.

[329] M. Müller and J. M. Schins, "Imaging the Thermodynamic State of Lipid Membranes with Multiplex CARS Microscopy," *J Phys Chem B,* vol. 106, pp. 3715-3723, 2011/12/21 2002.

[330] J.-X. Cheng, A. Volkmer, L. D. Book, and X. S. Xie, "Multiplex Coherent Anti-Stokes Raman Scattering Microspectroscopy and Study of Lipid Vesicles," *J Phys Chem B,* vol. 106, pp. 8493-8498, 2011/12/21 2002.

[331] H. A. Rinia, K. N. J. Burger, M. Bonn, and M. Müller, "Quantitative Label-Free Imaging of Lipid Composition and Packing of Individual Cellular Lipid Droplets Using Multiplex CARS Microscopy," *Biophys J,* vol. 95, pp. 4908-4914, 2008.

[332] J. P. R. Day, K. F. Domke, G. Rago, H. Kano, H.-o. Hamaguchi, E. M. Vartiainen, and M. Bonn, "Quantitative Coherent Anti-Stokes Raman Scattering (CARS) Microscopy," *J Phys Chem B,* vol. 115, pp. 7713-7725, 2011/12/21 2011.

[333] C.-Y. Lin, J. L. Suhalim, C. L. Nien, M. D. Miljkovic, M. Diem, J. V. Jester, and E. O. Potma, "Picosecond spectral coherent anti-Stokes Raman scattering imaging with principal component analysis of meibomian glands," *J Biomed Opt,* vol. 16, p. 021104, Feb 2011.

[334] M. N. Slipchenko, T. T. Le, H. T. Chen, and J. X. Cheng, "High-Speed Vibrational Imaging and Spectral Analysis of Lipid Bodies by Compound Raman Microscopy," *J. Phys. Chem. B,* vol. 113, pp. 7681-7686, May 2009.

[335] T. T. Le, H. M. Duren, M. N. Slipchenko, C.-D. Hu, and J.-X. Cheng, "Label-free quantitative analysis of lipid metabolism in living caenorhabditis elegans," *J Lipid Res,* vol. 51, pp. 672-7, September 23, 2009 2010.

[336] G. Ayala, P. Carmona, M. de Cózar, and J. Monreal, "Vibrational spectra and structure of myelin membranes," *Eur Biophys J,* vol. 14, p. 219, 1987.

[337] T. A. Brasitus and D. Schachter, "Lipid dynamics and lipid-protein interactions in rat enterocyte basolateral and microvillus membranes," *Biochemistry,* vol. 19, pp. 2763-2769, 1980.

[338] B. P. Gaber and W. L. Peticolas, "On the quantitative interpretation of biomembrane structure by Raman spectroscopy," *Biochim Biophys Acta - Biomembranes,* vol. 465, pp. 260-274, 1977.

[339] H. Chamras, A. Ardashian, D. Heber, and J. A. Glaspy, "Fatty acid modulation of MCF-7 human breast cancer cell proliferation, apoptosis and differentiation," *Journal of Nutritional Biochemistry,* vol. 13, pp. 711-716, Dec 2002.

[340] H. Chujo, M. Yamasaki, S. Nou, N. Koyanagi, H. Tachibana, and K. Yamada, "Effect of conjugated linoleic acid isomers on growth factor-induced proliferation of human breast cancer cells," *Cancer Letters,* vol. 202, pp. 81-87, Dec 2003.

[341] D. P. Rose and J. M. Connolly, "Effects of Fatty Acids and Inhibitors of Eicosanoid Synthesis on the Growth of a Human Breast Cancer Cell Line in Culture," *Cancer Res,* vol. 50, pp. 7139-7144, Nov 1990.

[342] S. Hardy, Y. Langelier, and M. Prentki, "Oleate activates phosphatidylinositol 3-kinase and promotes proliferation and reduces apoptosis of MDA-MB-231 breast cancer cells, whereas palmitate has opposite effects," *Cancer Res,* vol. 60, pp. 6353-6358, Nov 2000.

[343] A. M. Lorincz and S. Sukumar, "Molecular links between obesity and breast cancer," *Endocrine-Related Cancer,* vol. 13, pp. 279-292, Jun 2006.

[344] H. Bartsch, J. Nair, and R. W. Owen, "Dietary polyunsaturated fatty acids and cancers of the breast and colorectum: emerging evidence for their role as risk modifiers," *Carcinogenesis,* vol. 20, pp. 2209-2218, December 1, 1999 1999.

[345] D. Bagga, S. Capone, H. J. Wang, D. Heber, M. Lill, L. Chap, and J. A. Glaspy, "Dietary modulation of omega-3-omega-6 polyunsaturated fatty acid ratios in patients with breast cancer," *Journal of the National Cancer Institute,* vol. 89, pp. 1123-1131, Aug 1997.

[346] S. L. Capone, D. Bagga, and J. A. Glaspy, "Relationship between omega-3 and omega-6 fatty acid ratios and breast cancer," *Nutrition,* vol. 13, pp. 822-824, Sep 1997.

[347] M. Itoh, A. Nagafuchi, S. Moroi, and S. Tsukita, "Involvement of ZO-1 in Cadherin-based Cell Adhesion through Its Direct Binding to Î± Catenin and Actin Filaments," *J Cell Biol,* vol. 138, pp. 181-192, July 14, 1997 1997.

[348] L. González-Mariscal, A. Betanzos, P. Nava, and B. E. Jaramillo, "Tight junction proteins," *Prog. Biophys. Mol. Biol.,* vol. 81, pp. 1-44, 2003.

[349] A. S. Fanning, B. J. Jameson, L. A. Jesaitis, and J. M. Anderson, "The Tight Junction Protein ZO-1 Establishes a Link between the Transmembrane Protein Occludin and the Actin Cytoskeleton," *J Biol Chem,* vol. 273, pp. 29745-29753, November 6, 1998 1998.

[350] E. S. Wittchen, J. Haskins, and B. R. Stevenson, "Protein interactions at the tight junction - Actin has multiple binding partners, and ZO-1 forms independent complexes with ZO-2 and ZO-3," *J Biol Chem,* vol. 274, pp. 35179-35185, Dec 1999.

[351] Y. Qin, C. Capaldo, B. M. Gumbiner, and I. G. Macara, "The mammalian Scribble polarity protein regulates epithelial cell adhesion and migration through E-cadherin," *J. Cell Biol.,* vol. 171, pp. 1061-1071, December 19, 2005 2005.

[352] C. DeSantis, R. Siegel, P. Bandi, and A. Jemal, "Breast cancer statistics, 2011," *CA Cancer J Clin,* vol. 61, pp. 408-418, 2011.

[353] R. A. Smith, D. Saslow, K. A. Sawyer, W. Burke, M. E. Costanza, W. P. E. III, R. S. Foster, E. Hendrick, H. J. Eyre, and S. Sener, "American cancer society guidelines for breast cancer screening: update 2003," *CA Cancer J Clin,* vol. 54, p. 141, 2003.

[354] R. J. Nold, R. L. Beamer, S. D. Helmer, and M. F. McBoyle, "Factors influencing a woman's choice to undergo breast-conserving surgery versus modified radical mastectomy," *Am J Surg.,* vol. 180, pp. 413–418, 2000.

[355] B. Fisher, S. Anderson, J. Bryant, R. G. Margolese, M. Deutsch, E. R. Fisher, J.-H. Jeong, and N. Wolmark, "Twenty-year follow-up of a randomized trial comparing total mastectomy, lumpectomy, and lumpectomy plus irradiation for the treatment of invasive breast cancer," *N Engl J Med,* vol. 347, pp. 1233-1241, 2002.

[356] U. Veronesi, N. Cascinelli, L. Mariani, M. Greco, R. Saccozzi, A. Luini, M. Aguilar, and E. Marubini, "Twenty-year follow-up of a randomized study comparing breast-conserving surgery with radical mastectomy for early breast cancer," *N Engl J Med,* vol. 347, pp. 1227-1232, 2002.

[357] "Treatment of early-stage breast cancer," *JAMA-J Am Med Assoc,* vol. 265, pp. 391-5, 1991.

[358] T. J. Kearney and M. Morrow, "Effect of reexcision on the success of breast-conserving surgery," *Ann Surg Oncol,* vol. 2, pp. 303-307, 1995.

[359] P. I. Tartter, J. Kaplan, I. Bleiweiss, C. Gajdos, A. Kong, S. Ahmed, and D. Zapetti, "Lumpectomy margins, reexcision, and local recurrence of breast cancer," *Am J Surg.,* vol. 179, pp. 81–85, 2000.

[360] T. S.Menes, P. I. Tartter, I. Bleiweiss, J. H.Godbold, A. Estabrook, and S. R. Smith, "The consequence of multiple re-excisions to obtain clear lumpectomy margins in breast cancer patients," *Ann Surg Oncol*, vol. 12, pp. 881-885, 2005.

[361] F. D. Rahusen, A. J. A. Bremers, H. F. J. Fabry, T. v. Amerongen, R. P. A. Boom, and S. Meijer, "Ultrasound-Guided Lumpectomy of Nonpalpable Breast Cancer Versus Wire-Guided Resection: A Randomized Clinical Trial," *Ann Surg Oncol,* vol. 9, pp. 994–998, 2002.

[362] A. Chagpar, T. Yen, A. Sahin, K. K. Hunt, G. J. Whitman, F. C. Ames, M. I. Ross, F. Meric-Bernstam, G. V. Babiera, S. E. Singletary, and H. M. Kuerer, "Intraoperative margin assessment reduces reexcision rates in patients with ductal carcinoma in situ treated with breast-conserving surgery," *Am J Surg,* vol. 186, pp. 371-377, 2003.

[363] F. J. Fleming, A. D. K. Hill, E. W. M. Dermott, A. O'Doherty, N. J. O'Higgins, and C. M. Quinn, "Intraoperative margin assessment and re-excision rate in breast conserving surgery," *Eur J Surg Oncol,* vol. 30, pp. 233-237, 2004.

[364] E. R. Camp, P. F. McAuliffe, J. S. Gilroy, C. G. Morris, D. S. Lind, N. P. Mendenhall, and E. M. C. III, "Minimizing local recurrence after breast conserving therapy using intraoperative shaved margins to determine pathologic tumor clearance," *J Am Coll Surg,* vol. 201, pp. 855-861, 2005.

[365] M. M. Moore, L. A. Whitney, L. Cerilli, J. Z. Imbrie, M. Bunch, V. B. Simpson, and J. B. Hanks, "Intraoperative ultrasound is associated with clear lumpectomy margins for palpable infiltrating ductal breast cancer," *Ann Surg,* vol. 233, pp. 761-768, 2001.

[366] M. F. Kircher, U. Mahmood, R. S. King, R. Weissleder, and L. Josephson, "A multimodal nanoparticle for preoperative magnetic resonance imaging and intraoperative optical brain tumor delineation," *Cancer Res,* vol. 63, pp. 8122-8125, 2003.

[367] T. Karni, I. Pappo, J. Sandbank, O. Lavon, V. Kent, R. Spector, S. Morgenstern, and S. Lelcuk, "A device for real-time, intraoperative margin assessment in breast-conservation surgery," *Am J Surg,* vol. 194, pp. 467-473, 2007.

[368] G. J. Tearney, M. E. Brezinski, B. E. Bouma, S. A. Boppart, C. Pitris, J. F. Southern, and J. G. Fujimoto, "In vivo endoscopic optical biopsy with optical coherence tomography," *Science,* vol. 276, pp. 2037-2039, 1997.

[369] S. A. Boppart, W. Luo, D. L. Marks, and K. W. Singletary, "Optical coherence tomography: feasibility for basic research and image-guided surgery of breast cancer," *Breast Cancer Res Tr,* vol. 84, pp. 85–97, 2004.

[370] A. S. Haka, K. E. Shafer-Peltier, M. Fitzmaurice, J. Crowe, R. R. Dasari, and M. S. Feld, "Diagnosing breast cancer by using Raman spectroscopy," *P Natl Acad Sci USA,* vol. 102, pp. 12371–12376, 2005.

[371] G. Pellacani, P. Guitera, C. Longo, M. Avramidis, S. Seidenari, and S. Menzies, "The impact of in vivo reflectance confocal microscopy for the diagnostic accuracy of melanoma and equivocal melanocytic lesions," *J Invest Dermatol,* vol. 127, pp. 2759-2765, 2007.

[372] I. J. Bigio, S. G. Bown, G. Briggs, C. Kelley, S. Lakhani, D. Pickard, P. M. Ripley, I. G. Rose, and C. Saunders, "Diagnosis of breast cancer using elastic-scattering spectroscopy: preliminary clinical results," *J Biomed Opt*, vol. 5, pp. 221-228, 2000.

[373] W. R. Zipfel, R. M. Williams, and W. W. Webb, "Nonlinear magic: multiphoton microscopy in the biosciences," *Nat Biotechnol*, vol. 21, pp. 1369-1377, 2003.

[374] M. C. Skala, J. M. Squirrell, K. M. Vrotsos, J. C. Eickhoff, A. Gendron-Fitzpatrick, K. W. Eliceiri, and N. Ramanujam, "Multiphoton microscopy of endogenous fluorescence differentiates normal, precancerous, and cancerous squamous epithelial tissues," *Cancer Res*, vol. 65, pp. 1180-1186, 2005.

[375] N. D. Kirkpatrick, M. A. Brewer, and U. Utzinger, "Endogenous Optical Biomarkers of Ovarian Cancer Evaluated with Multiphoton Microscopy," *Cancer Epidemiol Biomarkers Prevent*, vol. 16, pp. 2048-2057, 2007.

[376] W. R. Zipfel, R. M. Williams, R. Christie, A. Y. Nikitin, B. T. Hyman, and W. W. Webb, "Live tissue intrinsic emission microscopy using multiphoton-excited native fluorescence and second harmonic generation," *P Natl Acad Sci USA*, vol. 100, pp. 7075-7080, 2003.

[377] T. T. Le, T. B. Huff, and J.-X. Cheng, "Coherent anti-Stokes Raman scattering imaging of lipids in cancer metastasis," *BMC Cancer*, vol. 9, 2009.

[378] C. L. Evans, X. Xu, S. Kesari, X. S. Xie, S. T. C. Wong, and G. S. Young, "Chemically-selective imaging of brain structures with CARS microscopy," *Opt. Express*, vol. 15, pp. 12076-12087, 2007.

[379] G. Thordarson, A. V.Lee, M. McCarty, K. V. Horn, O. Chu, Y.-C. Chou, J. Yang, R. C.Guzman, S. Nandi, and F. Talamantes, "Growth and characterization of N-methyl-N-nitrosourea-induced mammary tumors in intact and ovariectomized rats," *Carcinogenesis*, vol. 22, pp. 2039-2047, 2001.

[380] J. Liska, S. Galbavy, D. Macejova, J. Zlatos, and J. Brtko, "Histopathology of mammary tumours in female rats treated with 1-methyl-1-nitrosourea," *Endocr Regul*, vol. 34, pp. 91-96, 2000.

[381] M. H. Zaman, L. M. Trapani, A. L. Sieminski, D. MacKellar, H. Gong, R. D. Kamm, A. Wells, D. A. Lauffenburger, and P. Matsudaira, "Migration of tumor cells in 3D matrices is governed by matrix stiffness along with cell-matrix adhesion and proteolysis," *P Natl Acad Sci USA*, vol. 103, pp. 10889–10894, 2006.

[382] Y. Fu, H. Wang, R. Shi, and J.-X. Cheng, "Second harmonic and sum frequency generation imaging of fibrous astroglial filaments in ex vivo spinal tissues," *Biophys. J* . vol. 92, pp. 3251-3259, 2007.

[383] H.-W. Wang, T. T. Le, and J.-X. Cheng, "Label-free imaging of arterial cells and extracellular matrix using a multimodal CARS microscope," *Opt Commun*, vol. 281, pp. 1813–1822, 2008.

[384] E. Brown, T. McKee, E. Tomaso, A. Pluen, B. Seed, Y. Boucher, and R. K. Jain, "Dynamic imaging of collagen and its modulation in tumors in vivo using second-harmonic generation," *Nat Med*, vol. 9, pp. 796-800, 2003.

[385] P. P. Provenzano, K. W. Eliceiri, J. M. Campbell, D. R. Inman, J. G. White, and P. J. Keely, "Collagen reorganization at the tumor-stromal interface facilitates local invasion," *BMC Med,* vol. 4, 2006.

[386] P. P. Provenzano, D. R. Inman, K. W. Eliceiri, J. G. Knittel, L. Yan, C. T. Rueden, J. G. White, and P. J. Keely, "Collagen density promotes mammary tumor initiation and progression," *BMC Med,* vol. 6, 2008.

[387] A. M. Lorincz and S. Sukumar, "Molecular links between obesity and breast cancer," *Endocr Relat Cancer,* vol. 13, pp. 279-292, Jun 2006.

[388] C. H. MacLean, S. J. Newberry, W. A. Mojica, P. Khanna, A. M. Issa, M. J. Suttorp, Y. W. Lim, S. B. Traina, L. Hilton, R. Garland, and S. C. Morton, "Effects of omega-3 fatty acids on cancer risk - A systematic review," *Jama-Journal of the American Medical Association,* vol. 295, pp. 403-415, Jan 2006.

[389] M. Mezzetti, C. La Vecchia, A. Decarli, P. Boyle, R. Talanmini, and S. Franceschi, "Population attributable risk for breast cancer: Diet, nutrition, and physical exercise," *Journal of the National Cancer Institute,* vol. 90, pp. 389-394, Mar 1998.

[390] D. J. Hunter, D. Spiegelman, H. O. Adami, L. Beeson, P. A. vandenBrandt, A. R. Folsom, G. E. Fraser, R. A. Goldbohm, S. Graham, G. R. Howe, L. H. Kushi, J. R. Marshall, A. McDermott, A. B. Miller, F. E. Speizer, A. Wolk, S. S. Yaun, and W. Willett, "Cohort studies of fat intake and the risk of breast cancer - A pooled analysis," *New England Journal of Medicine,* vol. 334, pp. 356-361, Feb 1996.

[391] M. Maurer, T. Su, L. H. Saal, S. Koujak, B. D. Hopkins, C. R. Barkley, J. P. Wu, S. Nandula, B. Dutta, Y. L. Xie, Y. R. Chin, D. I. Kim, J. S. Ferris, S. K. Gruvberger-Saal, M. Laakso, X. M. Wang, L. Memeo, A. Rojtman, T. Matos, J. S. Yu, C. Cordon-Cardo, J. Isola, M. B. Terry, A. Toker, G. B. Mills, J. J. Zhao, V. Murty, H. Hibshoosh, and R. Parsons, "3-Phosphoinositide-Dependent Kinase 1 Potentiates Upstream Lesions on the Phosphatidylinositol 3-Kinase Pathway in Breast Carcinoma," *Cancer Research,* vol. 69, pp. 6299-6306, Aug 2009.

[392] H. J. Lin, F. C. Hsieh, H. Song, and J. Lin, "Elevated phosphorylation and activation of PDK-I/AKT pathway in human breast cancer," *British Journal of Cancer,* vol. 93, pp. 1372-1381, Dec 2005.

[393] A. Lykidis, P. D. Jackson, C. O. Rock, and S. Jackowski, "The role of CDP-diacylglycerol synthetase and phosphatidylinositol synthase activity levels in the regulation of cellular phosphatidylinositol content," *Journal of Biological Chemistry,* vol. 272, pp. 33402-33409, Dec 1997.

VITA

VITA

Shuhua Yue
Graduate School, Purdue University

Education
B.S., Engineering, 2007, Tsinghua University, Beijing, China
Ph.D., Engineering, 2013, Purdue University, West Lafayette, Indiana

Research Interests
Biomedical optics
Raman spectromicroscopy
Lipid metabolism in human cancers
Biomarker for cancer diagnosis
Novel target for cancer therapy

PUBLICATIONS

PUBLICATIONS

1. **Shuhua Yue**, Junjie Li, Seung-Young Lee, Bing Song, Tian Shao, Hyeon Jeong Lee, Liang Cheng, Timothy Masterson, Xiaoqi Liu, Timothy Ratliff, Ji-Xin Cheng, "Altered cholesterol metabolism: new avenue to diagnosis and treatment of human prostate cancer" (under revision to **Cell Metabolism**).
2. **Shuhua Yue**, Juan Manuel Cárdenas-Mora, Lesley S. Chaboub, Sophie A. Lelièvre, Ji-Xin Cheng, "Label-free analysis of breast tissue polarity by Raman imaging of lipid phase", **Biophysical Journal**, 2012, 102(5): 1215-1223.
3. **Shuhua Yue**, Mikhail N Slipchenko, Ji-Xin Cheng, "Multimodal nonlinear optical microscopy", **Laser & Photonics Review**, 2011, 5(4):496-512.
4. **Shuhua Yue**, Juan Manuel Cárdenas-Mora, Sophie A. Lelièvre, Ji-Xin Cheng, "Highlyeffective screening of breast cancer risk factors by compound Raman analysis of 3D culture of human mammary epithelium", **AACR Proceedings** 2010.
5. **Shuhua Yue**, Meihan Wang, Fei Guo, Zhaohui Meng, Jing Bai, "Present status of the wearable wireless ECG", **Biomedical Engineering and Clinical Medicine**, 2006, 10(4):262-6.
6. Thuc Le, **Shuhua Yue**, Ji-Xin Cheng, "Shedding new light on lipid biology by CARS microscopy", **Journal of Lipid Research**, 2010, 51:3091.

7. Jung Yeon Kwon, Sang Gwon Seo, **Shuhua Yue**, Ji-Xin Cheng, Ki Won Lee, Kee-Hong Kim, "An inhibitory effect of resveratrol in the mitotic clonal expansion and insulin signaling pathway in the early phase of adipogenesis", **Nutrition Research** 2012, 32(8): 607-16.

8. Delong Zhang, Mikhail N. Slipchenko, **Shuhua Yue**, Junjie Li and Ji-Xin Cheng, "A femtosecond stimulated Raman loss (fSRL) microscope for highly sensitive bond-selective imaging", **Proceedings of SPIE** 7903, 79032L (2011).

9. Junjie Yao, Gang Hu, **Shuhua Yue**, Jing Bai, "A 3D-surface Torso reconstruction method used in fluorescence molecular tomography of small animals", **Chinese Journal of Biomedical Engineering**, 2008, 27(3):360-5.

10. Jung Yeon Kwon, Sang Gwon Seo, Yong-Seok Heo, **Shuhua Yue**, Ji-Xin Cheng, Ki Won Lee, and Kee-Hong Kim, "Piceatannol, a natural polyphenolic stilbene, inhibits adipogenesis via modulation of mitotic clonal expansion and insulin receptor function in the early phase of differentiation", **Journal of Biological Chemistry** 2012, 287(14):11566-78.

11. Sang Gwon Seo, Hee Yang, Seung Ho Shin, Soyun Min, Yeong A. Kim, Jae Gak Yu, Dong Eun Lee, Min-Yu Chung, Yong-Seok Heo, Jung Yeon Kwon, **Shuhua Yue**, Kee Hong Kim, Ji-Xin Cheng, Ki Won Lee, Hyong Joo Lee, "A metabolite of daidzein, 6,7,4′-trihydroxyisoflavone, suppresses adipogenesis in 3T3-L1 preadipocytes via ATP-competitive inhibition of PI3K", **Molecular Nutrition & Food Research**, 2013, In press.